KAUNAS UNIVERSITY OF TECHNOLOGY

ARTURAS ALEKSANDROVAS

ARBITRARY POSITION AND WIDTH PULSE SEQUENCES FOR ULTRASONIC IMAGING AND MEASUREMENTS

Doctoral dissertation
Technological Sciences, Electrical and Electronic Engineering (01T)

2018, Kaunas

This doctoral dissertation was prepared at Kaunas University of Technology, Faculty of Electrical and Electronics, Department of Electronics Engineering during the period of 2013–2017.

Scientific Supervisor:

Prof. Dr. Linas SVILAINIS (Kaunas University of Technology, Technological Sciences, Electrical and Electronics Engineering – 01T)

Scientific Advisor:

Assoc. Prof. Dr. Alberto RODRIGUEZ MARTINEZ (Miguel Hernandez University of Elche, Technological Sciences, Electrical and Electronics Engineering – 01T)

Doctoral dissertation has been published in:
http://ktu.edu

English Language Editor:

Tony Bexon

ISBN 978-609-02-1500-5

The bibliographic information about the publication is available in the National Bibliographic Data Bank (NBDB) of the Martynas Mažvydas National Library of Lithuania.

KAUNO TECHNOLOGIJOS UNIVERSITETAS

ARTURAS ALEKSANDROVAS

LAISVAI PASIRENKAMOS TRUKMĖS IR POZICIJOS IMPULSŲ SEKOS ULTRAGARSINĖMS VIZUALIZACIJOS IR MATAVIMO SISTEMOMS

Daktaro disertacija
Technologijos mokslai, elektros ir elektronikos inžinerija (01T)

2018, Kaunas

Disertacija rengta 2013–2017 metais Kauno technologijos universiteto Elektros ir elektronikos fakulteto Elektronikos inžinerijos katedroje.

Mokslinis vadovas:

Prof. dr. Linas SVILAINIS (Kauno technologijos universitetas, technologijos mokslai, elektros ir elektronikos inžinerija – 01T)

Mokslinis konsultantas:

Doc. dr. Alberto RODRIGUEZ MARTINEZ (Elčės Migelio Hernandeso universitetas, technologijos mokslai, elektros ir elektronikos inžinerija – 01T)

Interneto svetainės, kurioje skelbiama disertacija, adresas:
http://ktu.edu

Redagavo:

Tony Bexon

ISBN 978-609-02-1500-5

Leidinio bibliografinė informacija pateikiama Lietuvos nacionalinės Martyno Mažvydo bibliotekos Nacionalinės bibliografijos duomenų banke (NBDB).

NOMENCLATURE AND ABBREVIATIONS

AC	Auto-correlation
ACF	Auto-correlation function
ADC	Analog to digital converter
AM	Amplitude modulation
AM-FM	Amplitude modulation – frequency modulation
AM-NLFM	Amplitude modulation – nonlinear frequency modulation
APWP	Arbitrary Position and Width Pulses
A-scan	Amplitude scan
B-scan	Brightness scan
CCF	Cross-correlation function
CRLB	Cramer-Rao lower error bound
CSIC	Spanish: Consejo Superior de Investigaciones Científicas
CW	Continuous wave
DAC	Digital to Analog converter
DC	Direct current
DFT	Discrete Fourier transform
EMI	Electromagnetic interference
FM	Frequency modulation
FM-CW	Frequency modulated continuous wave
GA	Genetic Algorithm
GFRP	Glass fiber reinforced plastic
HV	High voltage
IDFT	Inverse discrete Fourier transform
LFM	Linear frequency modulation (chirp)
MLW	Mainlobe level
NCCF	Normalized cross-correlation function
NDT	Nondestructive testing
NF	Noise figure
NLFM	Nonlinear frequency modulation (nonlinear chirp)
PCB	Printed circuit boards
PCB	Printed circuit board
PRF	Pulse repetition frequency
PSF	Point spread function
PSK	Phase shift keying
PWM	Pulse width modulation
RF	Radio frequency
RMS	Root mean square
ROC	Receiver operating curves
RT	Radiographic testing
SCR	Signal to clutter ratio
SLL	Sidelobes level
SMPS	Switched mode power supply
SNR	Signal to noise ratio
SS	Spread spectrum
SWC	Sine wave correlation
SWC	Sine wave correlation
ToF	Time-of-light
UT	Ultrasonic testing

TABLE OF CONTENTS

INTRODUCTION

Relevance of the research

The area of ultrasound applications is very wide. It is used in medical measurements [1,2], NDT (Nondestructive Testing) [3,4], materials properties study [5,6], liquid and gas flow measurement [7,8], food quality inspection [9] and many other areas [10,11,12]. The main advantages of ultrasound are that it does not use ionizing radiation, it directly interacts the with material mechanical properties, it can penetrate metals and opaque materials, and that the required equipment is of low cost, low energy, lightweight and relatively small in size [13,14].

There are two main ultrasonic NDT applications: measurements and imaging. Each of these applications requires different parameters to get reliable results. In measurement applications, the information about the objects under analysis is obtained from the signal propagation time, the reflection amplitude and/or the attenuation in the material [15]. As for imaging applications, the intensity of the reflections and their position in time provide the location and severity of defects or inhomogeneities [16,17].

Unfortunately, ultrasound has also some disadvantages: probing signals undergo not just attenuation, but also mode conversion, diffraction and have a limited bandwidth [18]. This bandwidth limiting is caused by the material (attenuation depends on frequency, therefore higher frequencies are attenuated more) and the transducer. Therefore, the quality of imaging and measurement applications depends on the probing signal [19]. Most ultrasonic systems use simple signals, such as pulse [20] or toneburst [6], because these signals are easy to generate and easy to interpret the results, but they either lack energy or bandwidth [21].

Spread spectrum (SS) signals, such as arbitrary waveform [26], chirp (LFM – Linear Frequency Modulation) [27,28], nonlinear chirp (NLFM – Nonlinear Frequency Modulation) and PSK – Phase Shift Keying) sequences [29], appear to be a solution for these shortcomings [22,23,24]. Application of spread spectrum signals offers significant advantages over simple signals, which can be summarized as:

- better SNR can be achieved by increasing excitation signal duration, yet not losing the signal bandwidth [16];
- spectrum can be programmed to any shape using SS, while pulse and a toneburst signal spectrum has a fixed shape (*sinc*) [37];
- bandwidth expansion beyond the transducer passband or smoothing can be achieved due to losses compensation [25].

Unfortunately, SS signals also has some disadvantages, mainly related to their length, dynamic range, spectral flatness and programmability. Regarding their length, SS signals have to be long in order to gain the energy, which could lead to reflections overlap; even for very sparsely spaced reflections [30]. On the other hand, the dynamic range in imaging is directly related with the dynamic range of the sidelobes, that is, the ration between main lobe and sidelobe amplitudes, and SS signals suffer from large correlation sidelobes [31]. For example, PSK are good in orthogonal probing, but have significant sidelobes and their spectrum is fixed and not flat [32,33].

Chirp, especially nonlinear, is good in spectral flatness, but it has also significant correlation sidelobes [28]. The cause is at the start and the end of the signal: all frequencies are present here so the spread spectrum property is distorted. This can be suppressed using windowing (Hamming, Tukey) but then efficiency will suffer [34]. Spectral programming of chirp is complex – no direct solution is available, although inverse solutions and approximations have been offered with some success [35,36,37].

Finally, there is another important issue. Probing signals can be classified by the way and how they are generated. For example, rectangular signals are generated by simple switch(-es) and arbitrary waveform generators use linear amplifier at the output. Rectangular excitation is more attractive and is widely used because: i) it is simpler and the cost of the equipment is lower [38,14], ii) it has a higher efficiency, resulting in less heat and longer battery life [39] and iii) the size and weight of the equipment is lower, and portability is demanded everywhere. Unfortunately, rectangular signals exhibit certain disadvantages: additional spectral ripples [6] and additional correlation sidelobes [25].

The aim of the research is to develop a new signals class in order to overcome the problems of conventional spread spectrum signals, and to investigate the performance of these signals in ultrasonic imaging and measurements.

Tasks of the research

The following tasks were formulated in order to achieve the objective:

1. Performance analysis of conventional excitation signals in imaging and measurement applications in order to rectify the shortcomings of these signals. Useful properties to be retained should be identified and possible applications for performance demonstration should be selected.
2. Development of a new type of the rectangular excitation signals capable of solving the shortcomings of the conventional signals. Design of the APWP (Arbitrary Position and Width Pulses) optimization technique; rectify performance parameters to be used as convergence criteria; propose a candidate set generation algorithm; propose a simple system transfer model for optimization.
3. Investigate the performance of APWP signals using the metrics rectified.
4. Demonstrate the APWP signals performance in imaging and measurement.

Scientific novelty

1. As a result of this work, a new type of rectangular excitation SS signals has been proposed: trains of arbitrary position and width pulses (APWP).
2. The usual approach to SS signals application does not assume signal optimization, therefore it is not adapted neither to the electronics, the transducers nor the materials under analysis. The novelty of the proposed APWP approach is the optimization of the APWP train accounting of the signal transmission through the system, which enhance the properties of the signals in terms of dynamic range, bandwidth and spectral flatness.

3. It was proposed to use a simple numerical model of the signal transmission through the ultrasonic system to speed up the optimization process: instead of doing the iterations on-line (in real environment), those are carried out virtually, using the system transmission model; such an approach not only speeds up the process but also ensures stable experiment conditions.
4. Three types of optimization procedures (Monte Carlo, genetic and combined) have been developed and tested. The best performance has been found when the initial conditions are defined by the rectangular waves derived from optimized nonlinear frequency modulation SS signals, and then optimization of pulse durations is carried out.

Practical value of the work

It is important to ensure the quality of results in ultrasonic measurements. Quality is determined by the received signal energy, bandwidth and correlation properties. Signals currently in use either do not provide the energy and bandwidth simultaneously but have good temporal properties (pulse, toneburst, step and spike). Conventional SS signals (phase manipulation by m-sequences, linear frequency modulation, chirp) do not offer the programmability of the spectral shape, or do not have the ability to control the correlation properties (chirp), or require complex equipment for excitation (arbitrary waveform signals).

To overcome the aforementioned shortcomings and limitations, a new type of spread spectrum signals (optimized APWP) was proposed in this work, which offers both wide bandwidth, high energy, has the ability to program the spectral shape and correlation properties and simultaneously do not require complex excitation electronics. The main advantages of the proposed APWP signals can be summarized as follows:

- simple excitation electronics is required, thanks to the elementary construction of pulse sets;
- spectral parameters can be programed, maintaining the excitation efficiency;
- combination of the advantages of square pulses and the SS signals;
- sidelobes' level can be minimized by adapting the excitation to the transducer and/or the system frequency response, therefore increasing the dynamic range.

With these enhancements, the proposed signals will be of great interest for the time delay estimation based applications, such as navigation, anemometry, flow measurement, ranging and material measurements. The signals allow to improve the measurement quality; due to the expanded effective bandwidth, better compression, lower correlation sidelobes and higher SNR.

It will also be of interest for imaging applications. Imaging resolution is improved by the expanded envelope bandwidth, and contrast is increased by the higher SNR and lower sidelobes.

Finally, these signals are extremely efficient in spectroscopy, where both the spectral coverage, flatness and SNR are important.

Results have been applied while carrying out these research projects:

- „Novel spread spectrum technologies in digital ultrasonic systems“, ULTRASPREAD from the Research Council of Lithuania.
- „Smart mechatronics technologies and solutions for processing effectiveness and environment care: from materials to tools“, In-smart EU structural support program.
- „Adaptive deconvolution algorithms for ultrasonic measurements“, ADECON, Kaunas University of Technology – funded interdisciplinary project.
- Industry contract for R&D with UAB SCiiL Baltic „ Electronics prototype for tank leakage detection using ultrasound“.
- R&D contract with the University Miguel Hernadez (Spain) „Prototype development of ultrasonic spread spectrum excitation data acquisition system“.

Approbation

The scientific results obtained during the period of the dissertation were presented in 22 publications: 6 articles were published in international journals referred in the Thomson Reuters Web of Science DB, 2 articles in journals referred in WoS DB but with no indexing, 14 publications appeared in conference proceedings of the conferences held in Bucharest (Romania), Metz (France), Warsaw (Poland), Prague (Czech Republic), Ghent (Belgium), Berlin (Germany), Athens (Greece), Sofia (Bulgaria), Dresden (Germany), Madrid (Spain) and Caparica (Portugal). The results were also presented in conferences held in Lithuania (Vilnius and Palanga). A grant for doctoral studies was received, provided by the Research Council of Lithuania and the Ministry of Education of the Republic of Lithuania for the period 2013-2017. A doctoral internship was carried out in University Miguel Hernandez in Elche, Spain, in 2016, funded by the ERSASMUS+ program.

Results presented in defense of the thesis

1. It has been demonstrated that conventional excitation signals have shortcomings and limitations:
   - pulse or toneburst signals do not provide energy and bandwidth simultaneously;
   - spectral shape and bandwidth of PSK signals is fixed; chirp signals have fixed spectral shape and large correlation sidelobes;
   - nonlinear chirp or arbitrary waveforms require complex excitation electronics.
2. APWP signals optimization technique has been proposed. Optimization accounts for the transfer function of the system. It is based on the following convergence criteria: the relative sidelobes level (both RF and envelope), the relative noise margin, the mainlobe width, the effective bandwidth and the spectral flatness.
3. Optimized APWP signals can give better performance metrics, in particular:

- APWP signals offer programmable correlation sidelobes, which can be made lower or comparable to other SS signals;
- APWP spatial resolution is comparable to chirp;
- APWP performance in the iterative deconvolution in the case of small reflections spacing is comparable to chirp, APWP performance is best in the case of large spacing;
- complex spectral shape can be designed, which can be used for either bandwidth improvement or spectral losses compensation;
- instead of using modulation (as PSK signals), spectra concentration within the passband can be achieved without sacrificing other parameters.

4. Performance of the APWP signals has been tested in imaging and measurement applications with successful results:
   - bias errors of flow measurement (zero flow temperature drift) can be improved;
   - relative noise margin can be improved, even with narrowband transducers;
   - spectral coverage (wider material properties and thickness range) and accuracy (better model fitting performance) of spectroscopy measurements can be improved;
   - deconvolution performance is improved.

Structure and coverage of the thesis

The dissertation consists of an introduction, five parts, conclusions, list of references and annexes. The volume of the work is 127 pages (132 pages with annexes). There are 11 tables, 73 equations and 144 figures. The list of references consists of 100 titles. The content of the thesis is organized as follows:

1. In the first chapter, an extensive analysis of the existing signals is presented, aiming to outline the shortcomings and advantages of the existing signals.
2. The second chapter analyzes applications of rectangular spread spectrum signals, aiming to indicate the advantages of these signals and also to rectify the problems occurring.
3. The third chapter is dedicated to develop the APWP optimization technique. Design of the convergence criteria, candidate set generation algorithm and system transfer model are presented.
4. The fourth chapter presents an exhaustive experimental performance analysis of the proposed APWP signals.
5. The fifth chapter is devoted to demonstrate the added value that APWP signals bring in imaging and measurement applications.

1. ANALYSIS OF THE CONVENTIONAL EXCITATION SIGNALS

This chapter is aimed at analyzing and discussing the essential shortcomings and advantages of the existing signals. Conventional excitation evaluation is based on the most common ultrasound applications: time of flight estimation, imaging and spectroscopy.

Rectangular pulse, step and spike excitation signals are regarded as standard. These signals are easy to generate, in addition the required equipment is simple, economical and portable. Results obtained with these signals are easy to interpret, there is no need for any correlation processing to get resolution. All historically settled techniques started from these signals. Unfortunately, due to their simplicity these signals have certain limitations. Conventional spread spectrum signals are included in the analysis in order to introduce their distinct properties and behavior.

1.1. Time of flight estimation

Estimation of the time-of-flight (ToF) of the ultrasonic pulse is used in material thickness measurement, ranging, acoustic properties measurement, material elastic properties, load, stress measurement, process monitoring, temperature measurement, and gas and liquid flow measurement [40].

The received signal *s(t)* is usually a delayed copy of the transmitted signal *r(t)* with reduced amplitude *A* and additive white noise [41]:

$$s(t) = A \cdot r(t-\tau) + n(t). \tag{1.1}$$

Phase, frequency or group delay [42,43,44] can be used in ToF estimation. Local properties (zero crossing, level thresholding, peak location [40]) or global (correlation peak, *L1*, *L2-norm* minimization [45]) signal properties match can be used to estimate the arrival time of the signal. The last three techniques are the most common in ToF estimation due to their accuracy and reliability and therefore will be discussed below.

Cross-correlation technique is using the maximum position of the cross-correlation as the ToF estimate [44]:

$$ToF_{CC} = \arg\left[\max\left(x(\tau)\right)\right], \tag{1.2}$$

where the cross-correlation *x* is defined as:

$$x(\tau) = \int_{-\infty}^{\infty} s(t) \cdot r(t-\tau)\, dt. \tag{1.3}$$

For the *L1*-norm, the location of the minimum of the *L*1-norm of the reference signal *r* subtraction from the received signal *s* can be used as the ToF estimate [45]:

$$ToF_{L1} = \arg\left\{\min\left[L1(\tau)\right]\right\}, \tag{1.4}$$

$$L1(\tau) = \int_{-\infty}^{\infty} \left|s(t) - r(t-\tau)\right| dt. \tag{1.5}$$

Finally, the location of $L2$-norm minimum of the remainder of the reference signal subtraction from the received signal can be used as the ToF estimate [45]:

$$ToF_{L2} = \arg\left\{\min\left[L2(\tau)\right]\right\}, \tag{1.6}$$

$$L2(\tau) = \int_{-\infty}^{\infty}\left[s(t) - r(t-\tau)\right]^2 dt\,. \tag{1.7}$$

Refer Fig. 1.1 for techniques' output comparison.

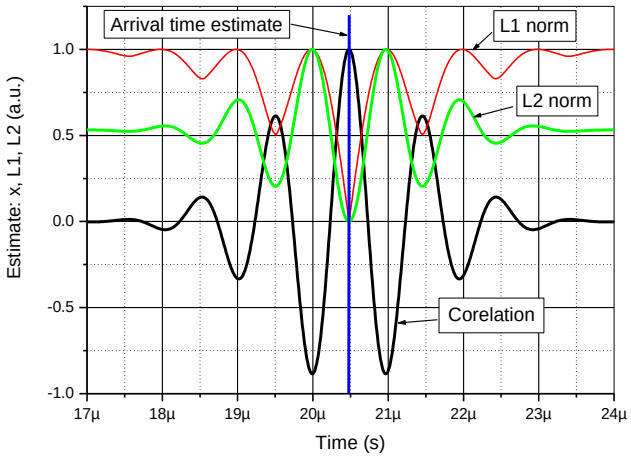

Fig. 1.1. ToF estimation using global properties match [40]

It can be seen that the correlation function has a maximum at ToF position while minimization techniques have a minimum. The aforementioned techniques have optimal filter properties [43,44], i.e., make full use of the signal energy. The ToF variance in such a case is defined by the Cramer-Rao lower error bound (CRLB) [46,47]. If the received signal is corrupted by additive white Gaussian noise and the correlation function peak is used for ToF estimation, the variance can be defined as:

$$\sigma_{ToF} \geq \frac{1}{2\pi F_e\sqrt{\dfrac{2E}{N_0}}}, \tag{1.8}$$

where F_e is the effective bandwidth, N_0 is power spectral density and E is the energy of the received signal, delivered to impedance Z, and that can be calculated as:

$$E = \frac{2}{Z}\int_0^{\infty} S(f)\cdot S^*(f)\,df \approx U^2\cdot\tau_i\,, \tag{1.9}$$

where $S(f)$ is the signal in frequency domain, $S^*(f)$ is the complex conjugate of $S(f)$, U is the signal amplitude and τ_i its duration (if rectangular pulse is used). On the other

hand, the effective bandwidth F_e is the square sum of the center frequency f_0 and envelope bandwidth β:

$$F_e^2 = f_0^2 + \beta^2 = \frac{\int_{-\infty}^{\infty} (f - f_0)^2 |S(f)|^2 df}{E} + \frac{\left[\int_{-\infty}^{\infty} f |S(f)|^2 df\right]^2}{E^2}. \quad (1.10)$$

Finally, the noise power density is obtained as [48]:

$$N_0 = \frac{e_{nT}^2 + e_{nV}^2 + (i_n \cdot Z)^2}{Z}, \quad (1.11)$$

where e_{nT} is the noise created by the real part of the transducer impedance Z_T, e_{nV} is the voltage and i_n is the current noise of the receiver [49]. It should be noted that the SNR is measured as the ratio of the signal energy to the noise power spectral density:

$$SNR = \frac{2E}{N_0}. \quad (1.12)$$

It can be concluded that the choice of the parameters to be used for ToF random errors reduction is limited. It should be noted that the noise power density is limited by the thermal noise and electronics used, and usually has little room for improvement. On the other hand, the bandwidth is mainly defined by the transducer used. Therefore, the only parameter available for a wider variation is the signal energy. The energy can be improved by increasing the excitation amplitude or the signal duration, but excitation amplitude is limited by the electronics and transducer design, therefore, the energy can be boosted only by increasing the signal duration.

If narrowband CW toneburst signals are used, anomalous ToF estimation errors can occur, because the neighboring correlation peaks can be taken as the absolute maximum (Fig. 1.2). Then, errors predicted by equation (1.8) are no longer valid – significant ToF estimation outliers start to prevail on the measurement [25].

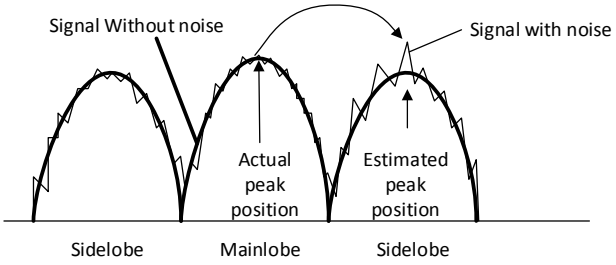

Fig. 1.2. Anomalous ToF estimation errors can occur if neighboring correlation peaks are high [25]

If can be concluded that both transducer and excitation signal spectrums have to be wide in order to avoid these abrupt errors. It can be concluded that SNR, center frequency and envelope bandwidth are important if high precision ToF measurement is needed.

1.2. Resolution

In case of reflection imagining, the media step response is evaluated: only places with a sudden change on acoustic impedance give reflections. The acoustic impedance is defined by the material velocity c and density ρ [99]:

$$Z = \rho c\,, \tag{1.13}$$

where c is defined as:

$$c = \sqrt{\frac{M}{\rho}}\,, \tag{1.14}$$

where M is the elastic modulus and ρ the density.

The reflection coefficient R_{12} between the material 1 and the material 2 is a function of their respective acoustic impedances Z_1 and Z_2:

$$R_{12} = \frac{Z_2 - Z_1}{Z_2 + Z_1}\,. \tag{1.15}$$

Signal received $s(t)$ from the test specimen is usually treated as the convolution of the specimen pulse response $h(t)$ [50] with the probing ultrasonic signal $s_p(t)$:

$$s(t) = \int_{-\infty}^{\infty} h(\tau)\cdot s_p(t-\tau)\,d\tau\,. \tag{1.16}$$

Reflections will overlap if spaced less than the duration of the probing signal. Resolution is the minimal spacing between two reflections; which can be resolved. Usually, it is considered that the duration of the pulse is equal to resolution [44]. Once the duration of the probing signal is defined by the system bandwidth, then it is the bandwidth that defines the resolution [51].

An experiment has been carried out to demonstrate the transducer bandwidth influence on resolution. The stepped sputtered composite sample was used. The thickness of the steps was 0.85 mm, 1.75 mm, 2.75 mm and 3.85 mm (Fig. 1.3).

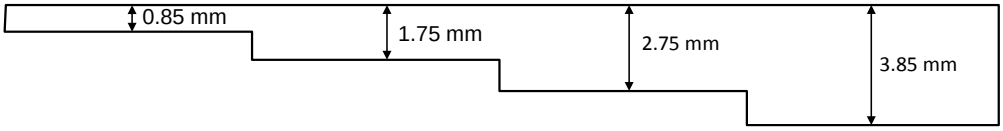

Fig. 1.3. Stepped composite sample drawing

Transducers with a center frequency 2 MHz and 5 MHz were used to collect ultrasonic data in reflection mode. Imaging was done in reflection mode, probing was done from the top of the sample. Collected A-scans were assembled into B-scan images with reflection amplitude converted into brightness.

Results are presented in Fig. 1.4.

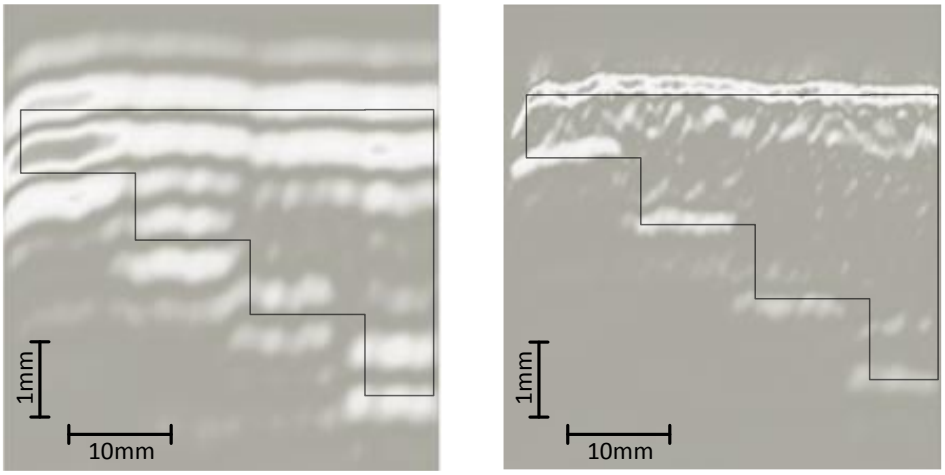

Fig. 1.4. Reflection mode image of the stepped composite sample using 2 MHz (right) and 5 MHz (left) transducers, with actual sample geometry overlaid [17]

It can be seen that the 5 MHz transducer allows to resolve 1 mm thickness. Resolution improvement was achieved because the resulting bandwidth of the transducer was wider: transducer bandwidth is a fraction of the center frequency. Refer Fig. 1.5 for bandwidth comparison of two simulated transducers with 50 % bandwidth.

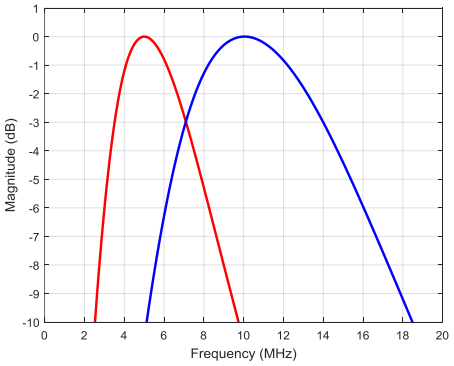

Fig. 1.5. Transducers bandwidth comparison

It can be concluded that the bandwidth of the system (mainly defined by the transducer) is defining the resolution limit. It can be assumed that the system bandwidth can be artificially improved by spectral equalization to improve the resolution. Compensation of spectral losses can be accomplished by dividing the signal *S(f)* by the probing signal $S_R(f)$ (addressed as reference) in the spectral domain:

$$S_{cmp}(f) = \frac{S(f)}{S_R(f)}. \tag{1.17}$$

Signal S_{cmp} then can be converted into a time domain by using Fourier transform. Such an operation is addressed as inverse filtering. This will correspond to the deconvolution of the signal received *s(t)* from the test specimen with the probing ultrasonic signal $s_R(t)$ so the specimen pulse response *h(t)* is obtained. Refer Fig. 1.6 for deconvolution example of the noise free signal (presented in publication [52]).

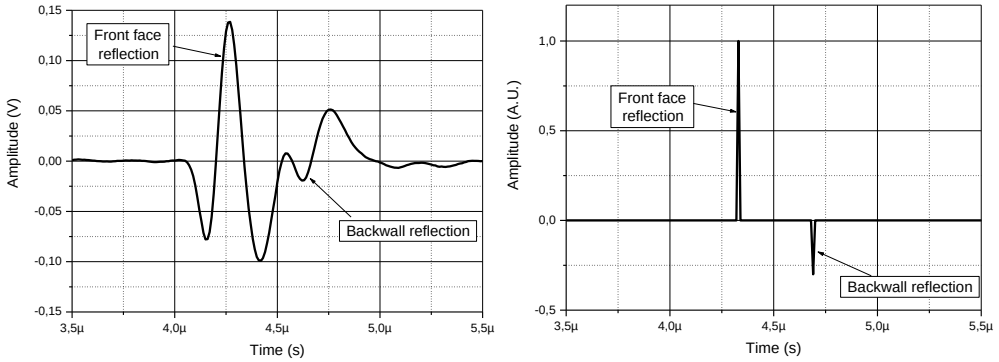

Fig. 1.6. Deconvolution result (right) of the noise free signal (left) [52]

Unfortunately, presence of noise complicates the deconvolution: the spectral areas where the signal to noise ratio (SNR) is low do not contain sufficient information. Refer Fig. 1.7 for same example as in Fig. 1.6 but with noise present.

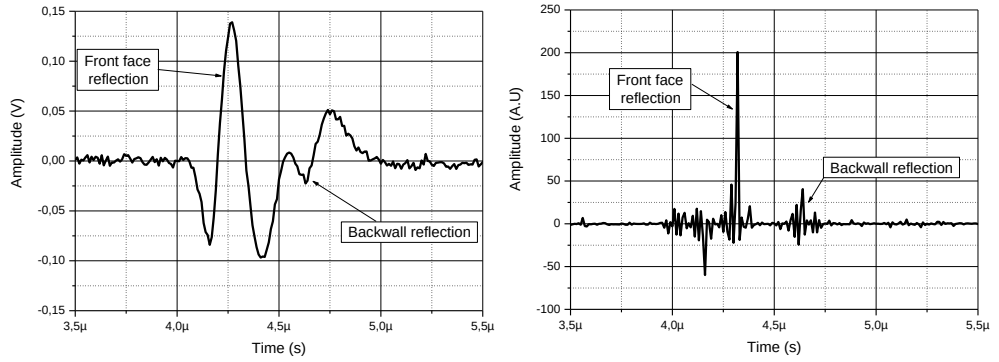

Fig. 1.7. Deconvolution of noisy signal (left): resulting signal have poor SNR (right) [52]

It can be seen that noise provides additional artifacts. The Wiener deconvolution has been proposed to avoid gain in areas with low SNR [53]. Despite SNR not influencing the resolution directly, it can be concluded that it is essential to have as much as possible a wide bandwidth and high SNR if artificial resolution improvement techniques are used.

1.3. Spectroscopy

Signals overlapping is a problem in imaging, but spectroscopy reduces this phenomenon [55]. Constructed and destructive interference occurs if the measured

layer thickness is so small that reflections overlap. The reflection coefficient R of the thin plate with impedance Z_2 immersed in liquid with impedance Z_1 is [17]:

$$R = \frac{Z_1^2 - Z_2^2}{Z_1^2 + Z_2^2 + 2iZ_1Z_2 \cot k_2 d}, \tag{1.18}$$

$$k_2 = \frac{2\pi}{c_2} + i\alpha, \tag{1.19}$$

$$Z_2 = Z_2^{'} + iZ_2^{''}, \tag{1.20}$$

where k_2 is the wave number of the plate, d is the thickness, α – attenuation coefficient and c_2 is the longitudinal velocity in the plate. From equations (1.18)-(1.20) it can be assumed that layers should produce some information in the spectral response. The reflection from a thin layer of a material with impedance Z followed by another material with impedance Z_{next} can be modelled using equations (1.15) and (1.21) [64]:

$$Z_{in} = \frac{Z(Z_{next}\cos(kd) + iZ\sin(kd))}{(Z\cos(kd) + iZ_{next}\sin(kd))}, \tag{1.21}$$

where k is the wave number for the layer and d is the layer thickness. More layers can be added by replacing Z_{next} with equation (1.21).

Refer to Fig. 1.8 left for the reflectivity simulation of the frequency response of single 150 μm Lucite layer (labeled as Material1, blue curve) and dual layer sample (150 μm Lucite on top of 200 μm polyvinyl chloride, labeled as Material2, red curve) using equations (1.18)-(1.21).

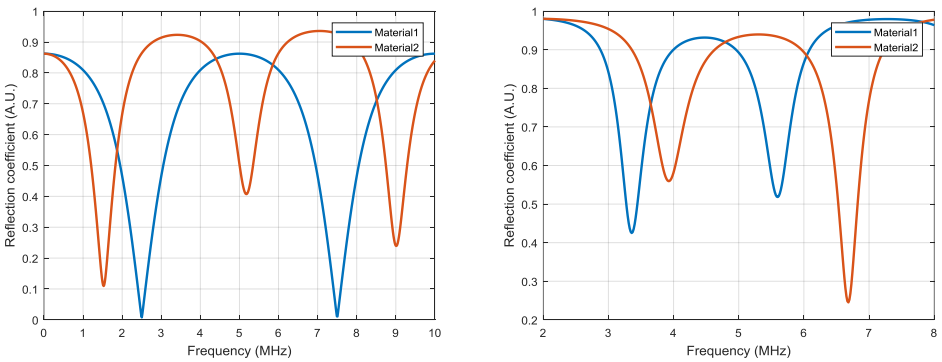

Fig. 1.8. Spectroscopy response from single layer and multilayer material (left); and multilayer material with different first layer thickness

It can be seen that a single layer has repeatable resonance, while response of multilayer material is more complex. Several resonances have to be measured in order to solve the inverse problem by fitting the model into measurement results [54]. Furthermore, even a slight change in the material thickness moves the resonances.

Refer to Fig. 1.8 right for the spectroscopy response comparison where the first material (Lucite) thickness was changed from 150 μm to 120 μm.

It can be concluded that, in order to have a wide range of possible thicknesses, wide bandwidth signals and transducers are needed to cover the bandwidth of interest. Furthermore, it is important to ensure good SNR at the resonances frequency.

Refer Fig. 1.9 for the noisy case of the same situation as above, when the same amplitude pulse and 3 μs long SS signal were used for probing.

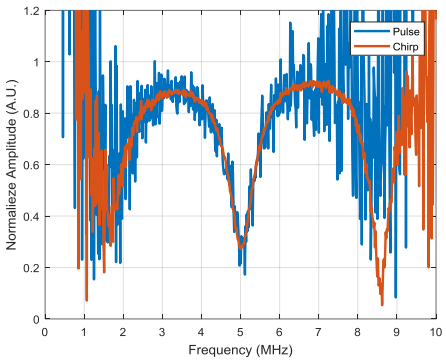

Fig. 1.9. SNR comparison when spectroscopy is carried out using pulse and SS signals

It can be seen that the resonant dips at 1.5 MHz and 8.5 MHz have very low SNR in the case of pulse excitation. It can be concluded that not only wide bandwidth but also high SNR has to be ensured for efficient spectroscopy application.

Spectroscopy can be used for thin laminates imaging. An experiment has been carried out to show the spectroscopy application in lamination quality inspection (presented in publication [17]). A plastic dual-layer laminate was applied on a Plexiglas slab (Fig. 1.10). The outer layer had a rough, decorative surface that created speckle, therefore inspection using the reflection amplitude was not possible.

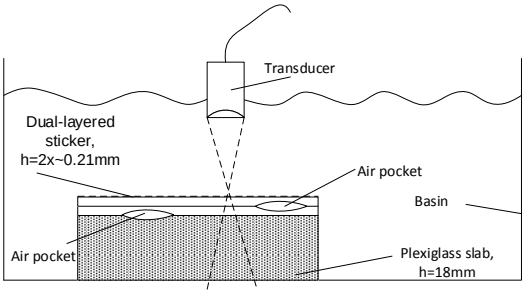

Fig. 1.10. Setup used for lamination quality inspection using spectroscopy [17]

The inspection has been carried out using a 5 MHz wideband focused transducer IRY405 (from NDT transducers LLC). The excitation used a wideband chirp covering (1-10) MHz of 3 μs duration. Refer Fig. 1.11 for 20x20 mm area image obtained using spectroscopy. A-scans, obtained at every x, y position, were transformed into frequency domain, using Discrete Fourier Transform (DFT). Magnitude at the selected frequency was used to create a C-scan image of the sample.

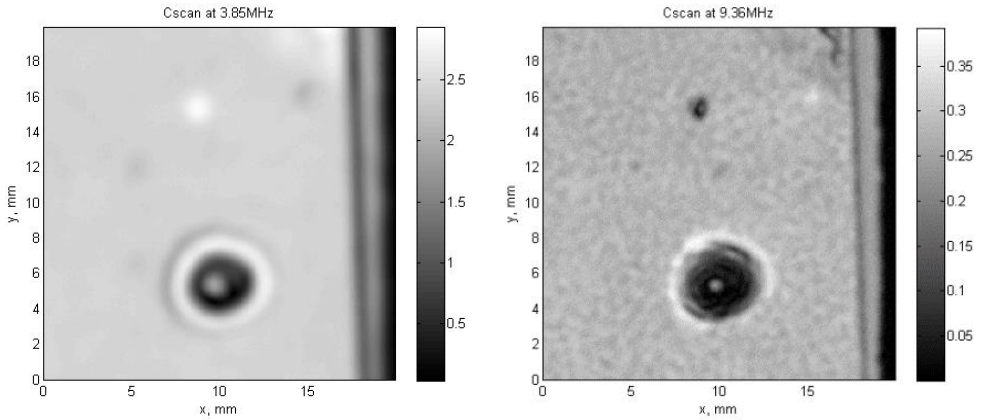

Fig. 1.11. Lamination quality inspection results using spectroscopy: spectral content magnitude (A.U.) at 3.85 MHz (left) and 9.36 MHz (right) [17]

The speckle caused by the rough outer surface was present at high frequencies (Fig. 1.11 left) but was absent at low frequencies (Fig. 1.11 right). The reflection from the air pocket caused by a sand particle trapped between the substrate and the laminate is visible in both images (lower center part). The air trapped between the laminate layers is also detectable (two small dots at the top). It should be noted that grain noise, usually created by electronics is low, due to the wideband and high SNR excitation.

1.4. Excitation using simple signals

The excitation signal's duration influences the spectral content. The disadvantage of pulse excitation is that the majority of the spectral content is outside of the transducer passband [95]. Refer Fig. 1.12 for spectral content comparison when the transducer was excited by 50 V rectangular pulse (left) and step (right).

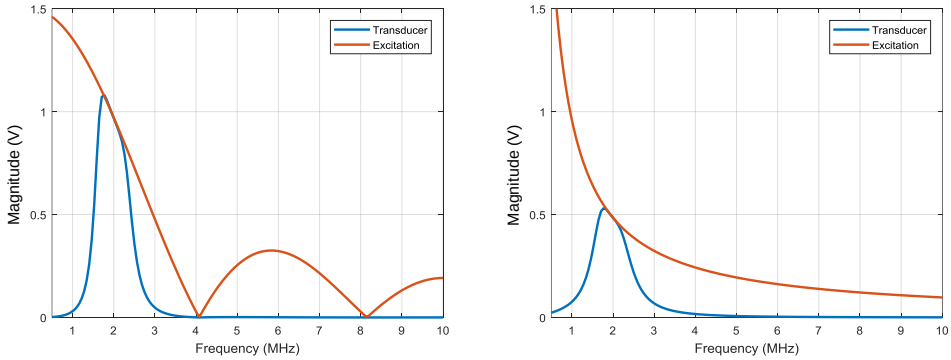

Fig. 1.12. Spectral content when transducer excited by 50 V rectangular pulse (left) and step (right)

It can be seen that the majority of the exciting signal energy is concentrated at low frequencies, while the transducer does not pass this frequency range. This

situation is even worse in the case of step excitation. Furthermore, the transducer excitation with a rectangular pulse requires a pulse duration matching in order to improve the efficiency [93]. Usually, the duration is chosen to be equal to half of the center frequency period. This means that the excitation signal energy is lesser for high frequency transducers.

Refer Fig. 1.13 for 40 % bandwidth transducer signals spectrum in the case of the transducer center frequency equal to 2 MHz, 5 MHz 10 MHz and 20 MHz.

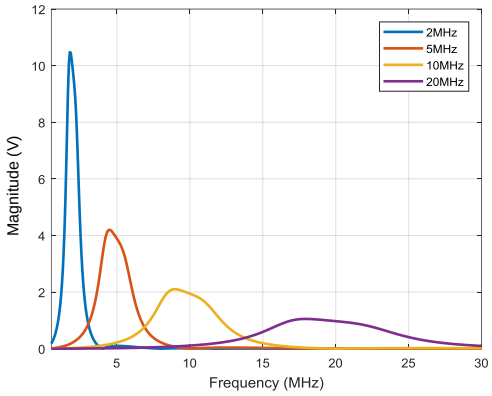

Fig. 1.13. Transducer output signal spectrums for 40 % bandwidth and center frequency 2 MHz, 5 MHz 10 MHz and 20 MHz

It can be seen that the spectral density decreases, despite the fact that the excitation pulse voltage was always 50 V. This decrease in the spectral density is also influenced by the fact that the pulser slew rate is fixed. The reason for a fixed slew rate is the MOSFET used for driving the transducer. The transducer input impedance is mainly capacitive, therefore, when the MOSFET is switching high voltage to capacitive load, the output rise time is defined by two processes: constant current charge (prevalent at the beginning of the charging cycle, defined by a peak current of the MOSFET I_{Dpeak}) and constant voltage charge through drain-source resistance R_{DS} (at the end of charging cycle). Rise time is mainly defined by a constant current charging mode, so rise time is approximately [56]:

$$t_{rise} = \frac{V_{tr} C_0}{I_{Dpeak}}, \tag{1.22}$$

where I_{Dpeak}/C_0 is equivalent to slew rate. Using 10 A I_{Dpeak} and a 500 pF transducer, the result shows a 20 V/ns slew rate. Refer Fig. 1.14 for pulser output signals comparison in the case of 50 V and 500 V output amplitude.

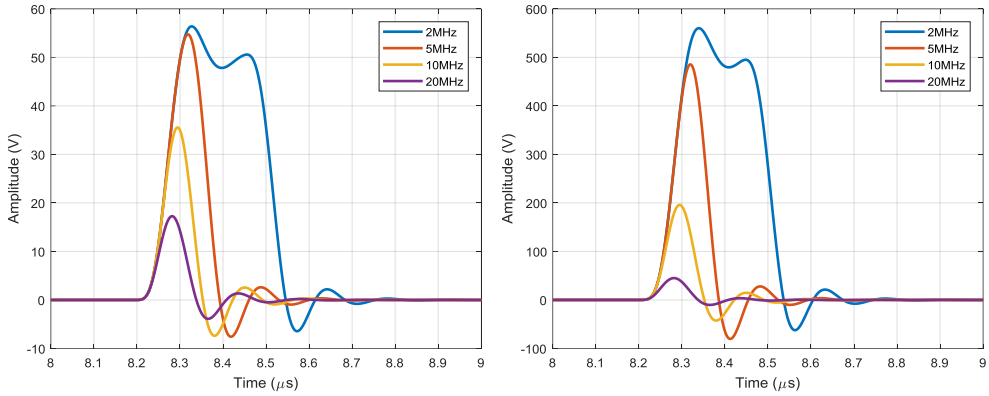

Fig. 1.14. Pulser output signals in case of 50 V (left) and 500 V (right) output amplitude

It can be seen that the signal amplitude is decreasing for higher output amplitudes. The reason is that the slew rate is insufficient for short pulse durations. Also, signal fronts should be taken into consideration. On the other hand, application of higher I_{Dpeak} MOSFET does not significantly improve the slew rate, because parasitically capacitance increases. For instance, IPD65R190C7 has 49 A $I_{Dpeak,}$ which may suggest that a 100 V/ns slew rate can be achieved, but it has 15nF C_{OSS} at 0 V V_{DS} that will significantly increase the switching time and reduce the pulser efficiency (compared to the usual 500 pF transducer capacitance). Refer Fig. 1.15 for transducer output spectral content comparison in case of 50 V (left) and 500 V (right) excitation amplitude [92,93].

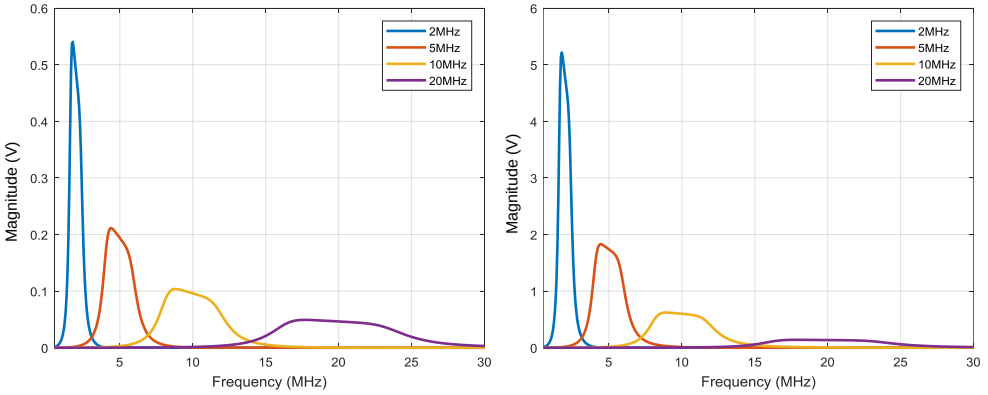

Fig. 1.15. Transducer output spectrum for 50 V (left) and 500 V (right) output amplitude

It can be concluded that excitation using single rectangular pulses leads to a spectral density decrease if high frequency transducers are used. This problem becomes critical for frequencies beyond 10 MHz, as the higher the transducer frequency the shorter the required pulse rise and fall time. Fixed slew rate limits the attainable signal amplitude/energy, and shorter pulse duration is required for higher

frequencies, which also reduces the excitation energy. Furthermore, the transducer spectral response is not flat (Fig. 1.16) because of the non-flat spectrum of the excitation signal.

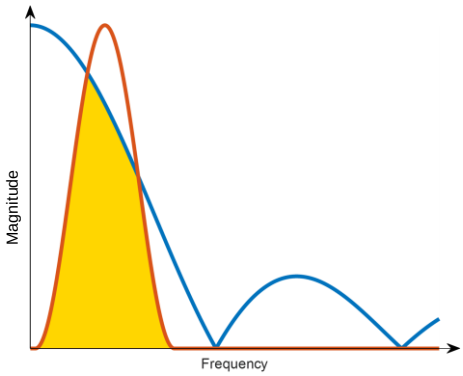

Fig. 1.16. Spectral density of the rectangular pulse is low at higher frequencies

Once the signal amplitude is limited, the energy can be increased by using longer duration toneburst with a fill-in frequency matched to the transducer frequency. Refer Fig. 1.17 for toneburst excitation spectra comparison.

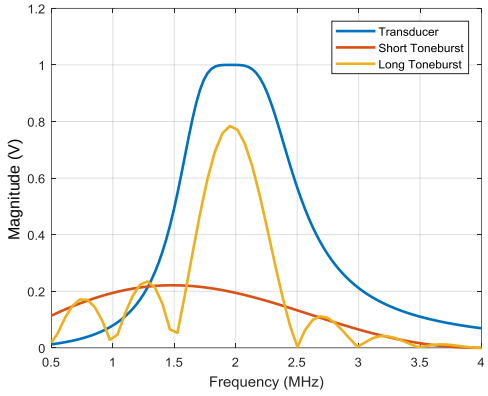

Fig. 1.17. Spectral content when transducer excited by toneburst (short: 1 period, long: 4 periods)

It can be seen that the shorter toneburst has wide bandwidth, but low energy, while a long toneburst has large energy, but its bandwidth is narrower than the transducer bandwidth. The toneburst energy can be increased further, but the bandwidth will be reduced significantly. Bandwidth is essential for resolution: as a wider bandwidth allows two reflections to be seen separately.

Refer to Fig. 1.18 for two reflections comparison in the case of pulse and toneburst excitation. It can be seen that overlapping occurs in the case of toneburst excitation due to the narrow signal bandwidth. Meanwhile, the pulse signal has a wide bandwidth, therefore the two reflections can be separated.

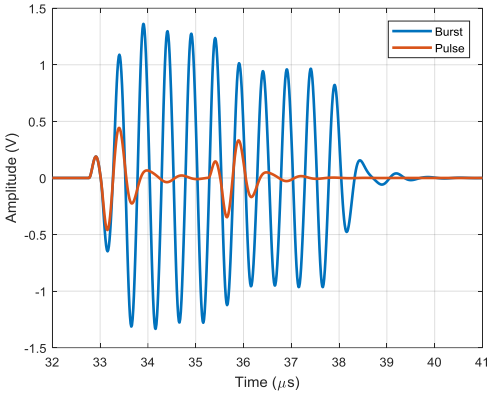

Fig. 1.18. Two reflections comparison in case of pulse and toneburst excitation

It can be concluded that classical signals have an energy and bandwidth conflict: increasing the duration increases the energy, but reduces the bandwidth. Yet effective bandwidth can be traded to SNR, because an effective bandwidth is related to the pulse duration directly, but SNR depends on pulse duration by square root. This means that by increasing the transducer center frequency four times increases the effective bandwidth four times; meanwhile the energy is decreased only twice when decreasing the pulse duration four times.

It is notable that simple signals cannot be compressed using correlation processing (equation (1.3). Refer to Fig. 1.19 for the compression result when rectangular pulse and toneburst signals are used (Fig. 1.18).

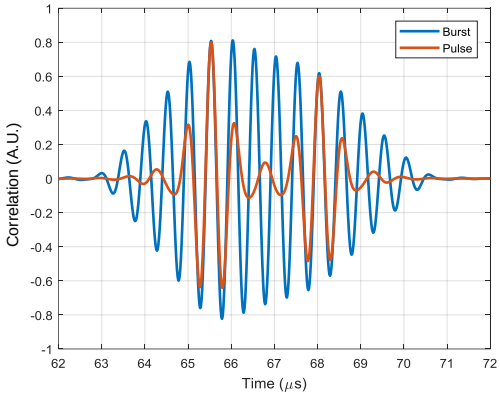

Fig. 1.19. Result of signal compression using correlation processing

It can be noted that there was no resolution improvement for both signals. The reason is that simple signals have an inverse relationship between signal duration and bandwidth, therefore the signal duration after correlation processing remains the same.

1.5. Excitations using SS signals

Spread spectrum (SS) signals are free from the aforementioned conflict, as energy and bandwidth can be programed independently. It is essential that SS signals

can be long without affecting the bandwidth. This way, the signal energy can be increased without the need to increase the amplitude. On the other hand, the SS signals spectrum can be adjusted independently of the signal duration. Refer to Fig. 1.20 for a SS signal (wideband 10 μs (1-10) MHz chirp, red curve, passband-matched 10 μs (4-6.5) MHz chirp, orange curve) spectral density comparison to pulse signal (blue curve).

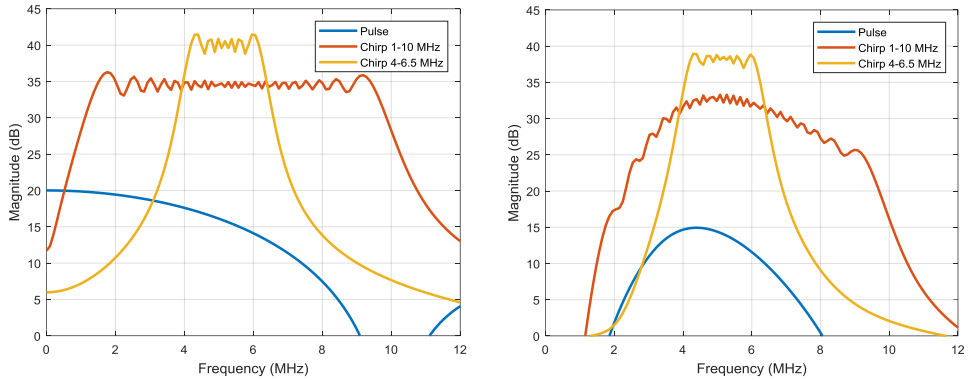

Fig. 1.20. Spectral density comparison of pulse and SS (chirp) signals: excitation signals (left) and after passing the transducer (right)

It can be seen that the energy of the SS signal is higher and the spectral bandwidth can be easily controlled. Some SS types have the ability to control the shape of the spectrum. Another essential advantage of SS signals is that they are compressible: their duration can be significantly reduced using matched filters (correlation processing). Refer to Fig. 1.21 left for SS signal and pulse signal response in the case of multiple reflections.

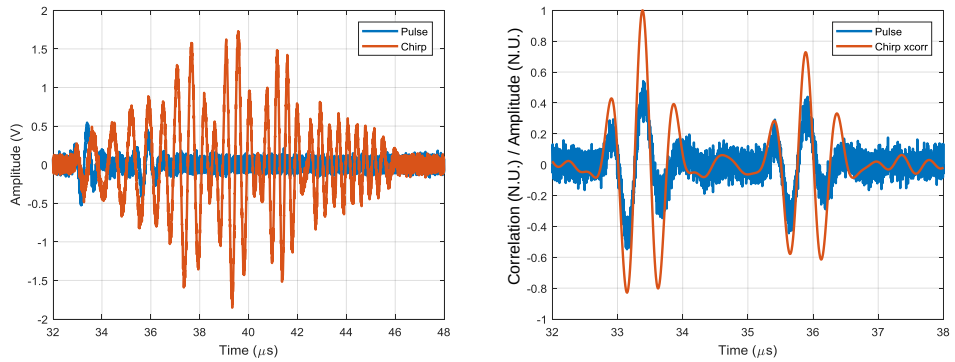

Fig. 1.21. Comparison of two closely placed reflections using pulse and SS excitation in time domain (left) and compression results (right)

It can be seen that the much longer SS duration causes a reflections overlap. However, due to its compressibility properties, the SS signal can be compressed using correlation processing (Fig. 1.21 right). It is also notable that the SS signal temporal

resolution is improved due to compression and can be matched to the resolution of pulse. Essentially, the SNR of SS was significantly improved due to the higher energy.

It can be concluded that the SS signals are a better option for high frequency and wideband excitation, although the pulse requires high amplitude, however the semiconductor switch has a *dV/dt* limit. The channel parameters of the switch and the load define the maximum *V/μs* slew rate. The rise and fall front duration is increased for fixed *dV/dt* if voltages are high. This results in a bandwidth limitation $f_{max}=1/(\pi \cdot t_{rise})$. On the other hand, SS can use lower amplitudes, so t_{rise} is short, resulting in a wider excitation bandwidth. SS signals offer a better excitation energy concentration. Note that the pulse and spike energy is concentrated at low frequencies, while the SS signals can concentrate the energy to the passband. It must also be noted that the SNR can be improved for pulse signals by averaging, however averaging is complicated in the case of a dynamic situation (on line NDT inspection, temperature variation, and vibrations). Unfortunately, SS signals bring additional problems that are discussed in the chapters below.

1.5.1. Arbitrary waveform signals

The best example of arbitrary waveform is the noise signal. It has very good correlation properties and can cover any bandwidth. Unfortunately, only noise with sufficient bandwidth and very long duration would have acceptable correlation properties and uniform spectral coverage. Arbitrary waveform excitation signals should remove the aforementioned problems if it were possible to derive the signal waveform from the desired correlation function. Unfortunately, such derivation is not possible because the correlation function cancels the phase information of the original signal. Therefore, PSK and FM signals are used as SS signals. In this work, PSK and FM signals that are created from sinusoids and can be amplitude modulated and are addressed as arbitrary waveform.

But they also have their drawbacks. The excitation of arbitrary waveform signals requires digital-to-analog converters (DAC) and analog amplifiers, which leads to complicated electronics and reduced excitation efficiency. Furthermore, not all arbitrary waveform signals can be practically realized (due to extremely large amplitudes, large dynamic range, complex numbers etc.).

1.5.2. PSK signals

Not all noise-like signals offer good correlation properties. Several pseudo noise sequences with the desired correlation properties have been derived: Barker, m-sequences, Kasami, Gold, Walsh Hadamard, Golay [57,35]. Since the bandwidth of these pseudo noise signals starts from DC but the ultrasonic transducer does not pass low frequencies, phase shift keying (PSK) is used to modulate the signal so the main energy is concentrated at the transducer center frequency [35]. The modulation is carried out by manipulating the initial phase of the chip (fragment of toneburst) according to a sequence code. PSK signals are widely used in ultrasonic measurements due to their benefits: orthogonality, simplicity of derivation and generation and compressibility. Orthogonality is achieved if the complex spectra of

PSK signals are orthogonal. Unfortunately, other SS properties of PSK signals have shortcomings [97].

PSK signals exhibit self-noise, i.e. sidelobes are present in their correlation function. Fortunately, self-noise becomes prevailed by random noise beyond certain sequence length (Fig. 1.22), because self-noise decays faster than random noise [57].

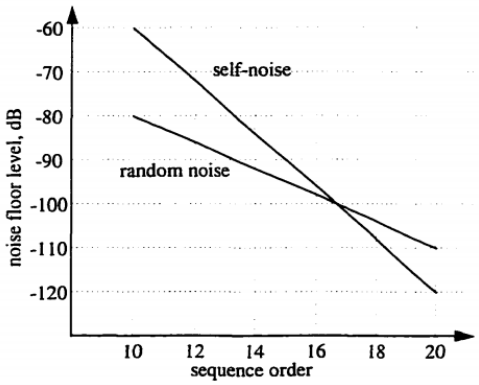

Fig. 1.22. Sequence length influence on self-noise and random-noise level [57]

Self-noise can be evaluated as the ratio of the sidelobes to mainlobe level:

$$SLL = 20\lg\left(\frac{A_{SL}}{A_{ML}}\right), \tag{1.23}$$

where A_{SL} is the maximum amplitude of the sidelobes and A_{ML} is the amplitude of the mainlobe. A disadvantage of PSK signals is that the sidelobes level is fixed, and it is defined by the length N of the sequence [98]. For example, Barker code SLL is $1/N$, sidelobes of the m-sequence with M combinations are [58]:

$$SLL = \sqrt{\frac{N^2(M-1)}{NM-1}}, \tag{1.24}$$

or approximately $1/\sqrt{N}$. It should be noted that equation (1.24) is valid only for periodical correlation. For aperiodic correlation, the SLL is even higher. For instance, with N=128 the SLL is -15 dB, with one 5 MHz period chip length, which would corresponded to 25.6 μs. In some cases, the resulting signal length can become unacceptable. It can be concluded that the sidelobes' level cannot be the controller if the signal length is fixed. Furthermore, there is a limit for the Barker code: minimum sidelobe level is -22.3 dB.

Another disadvantage of PSK signals is that they have very large spectral leakage. Spectral roll-off is defined by chip spectrum (*sinc* function): 6 dB per octave. Refer to Fig. 1.23 for spectral leakage comparison in the case of N=15, N=255 (chip fill-in frequency was 5 MHz and chip length was one period). Ten different m-sequences are plotted. It can be seen that the spectral leakage is not reduced by the code length. The transducer will dampen the components that are out of the passband,

therefore this energy will be lost and SNR reduced. Furthermore, because of these components, loss the correlation performance (SLL) will suffer.

Yet another disadvantage of PSK signals is that the shape of the spectrum is defined by the chip duration. Note that the shape of the spectrum is always the same and corresponds to a *sinc* function. The only way to change the position of the spectral zeros is to change the chip duration. When trying to fit the spectrum of PSK to the ultrasonic transducer bandwidth, a problem is that the bandwidth is defined by the shortest chip in a sequence [68]. If an integer number of half-periods is used for the chip, then bandwidth adjustment is discrete and usually does not fit the transducer bandwidth. For the analyzed case, the bandwidth of PSK signal cannot be increased further because the chip length is already at its minimum (one period).

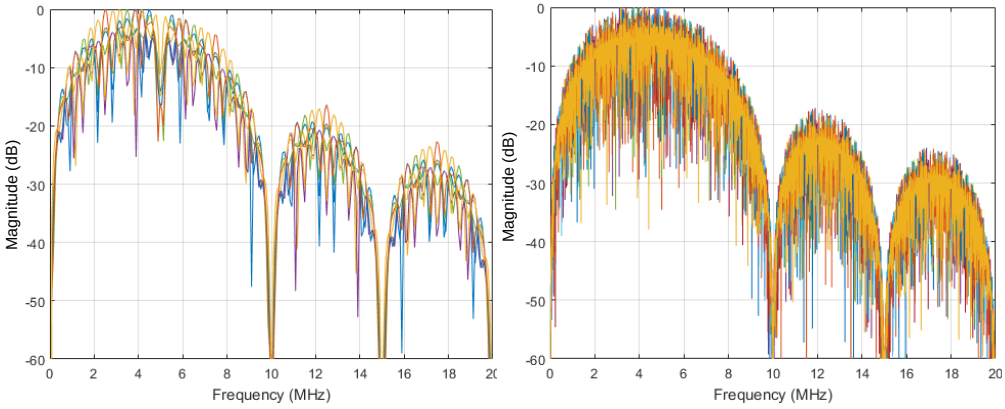

Fig. 1.23. Spectrums PN sequence with different lengths N=15 (left), N=255 (right)

Notable that PSK spectrum is not smooth, even within the passband: spectral dips can reach -40 dB (Fig. 1.23 right at 4.5 MHz).

It can be concluded that the SS PSK signals do not have the ability to program the spectral shape; have inherent spectral zeros and dips that cannot be tolerated by spectroscopy and will limit the capabilities of the inverse filtering.

1.5.3. Chirp signals

Another SS class are frequency modulation signals. Usually these signals are addressed as chirp. Linear frequency modulation (LFM) is the most common case:

$$s(t)\big|_{t=0..\tau_{chirp}} = U_{chirp}\sin\left(f_1 t + \frac{\Delta F}{2\tau_{chirp}}t^2\right), \tag{1.25}$$

where f_1 is the minimum frequency, ΔF is the frequency deviation, τ_{chrip} is the duration and U_{chirp} is the signal amplitude.

The non-linear version uses non-linear frequency modulation (NLFM):

$$s(t)\big|_{t=0..\tau_{chirp}} = U_{chirp}\sin\left(\phi_{chirp}\right), \tag{1.26}$$

where φ_{chirp} is the instantaneous phase, which can be any non-linear function.

Chirp signals offer several advantages: simple analytical description, ease of generation and compressibility. The spectral content of chirp signals and the correlation mainlobe width can be easily controlled by changing f_1 and ΔF. On the other hand, the amount of delivered energy can be controlled by τ_{chrip} or U_{chirp}. The NLFM version offers programmable spectral shape. In addition, chirp SS signals can avoid spectral zeros: rectangular pulse, tone burst, PSK sequences possess spectral zeros, which cannot be tolerated by spectroscopy and inverse filtering [55,59].

Unfortunately, chirp SS signals also have some disadvantages. The essential disadvantage comes from its constant envelope property: the spectral response is convolved with the *sinc* function of the envelope spectra because of the sharp rise and fall of the envelope (Fig. 1.24 left). Due to this, Fresnel ripples are introduced in the spectral response (Fig. 1.24 center). These ripples create far-range sidelobes (Fig. 1.24 right), while the rectangular shape of the chirp spectrum creates near-range sidelobes (Fig. 1.24 right).

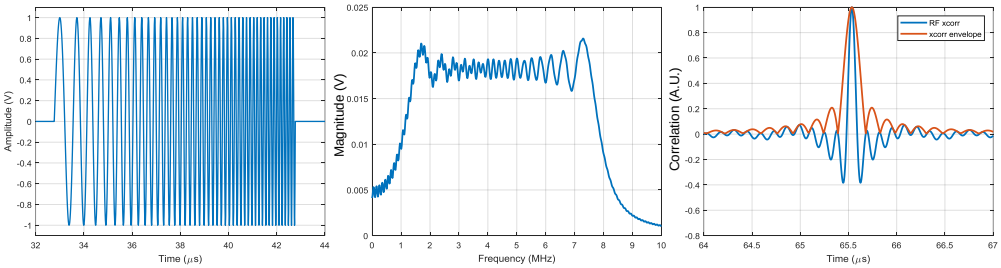

Fig. 1.24. Chirp signal (left), its spectrum (center) and corresponding correlation function (right)

It can be seen that the correlation function of the chirp has *sinc*-like envelope with sidelobes level at only -13.2 dB regardless of the time-bandwidth product. Far-range sidelobes can be reduced by tapering the chirp signal so that the sharp rise and fall of the envelope is avoided. Refer to Fig. 1.25 for the tapering effect demonstration on the same chip signal.

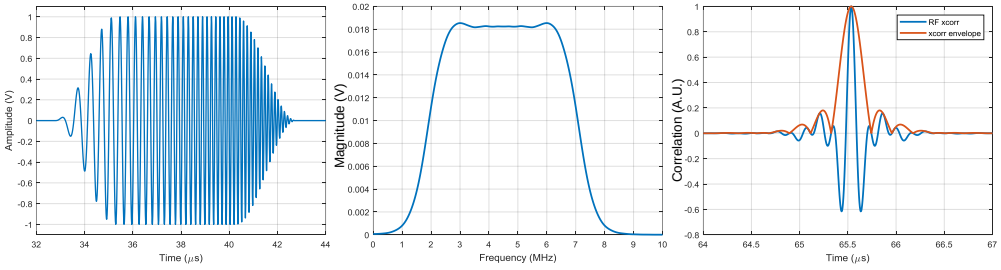

Fig. 1.25. Tapered chirp signal (left), spectrum (center) and correlation function (right)

Fig. 1.24 and Fig. 1.25 results were obtained without accounting for the influence of the transducer, but the transducer further reduces the signal bandwidth. Refer to Fig. 1.26 and Fig. 1.27 for results with the transducer influence accounted.

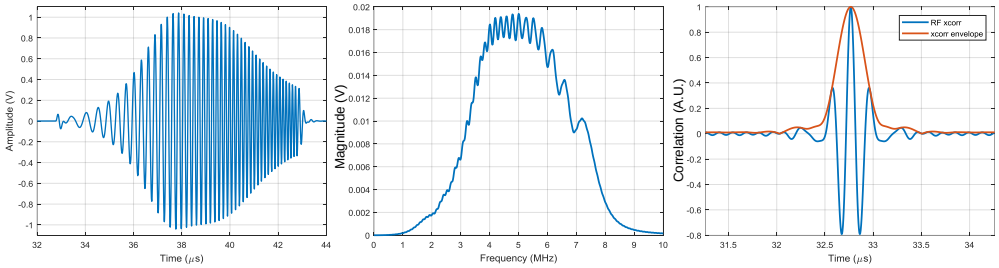

Fig. 1.26. Transducer output when chirp signal is used for excitation (left), resulting signal spectrum (center) and the correlation function (right)

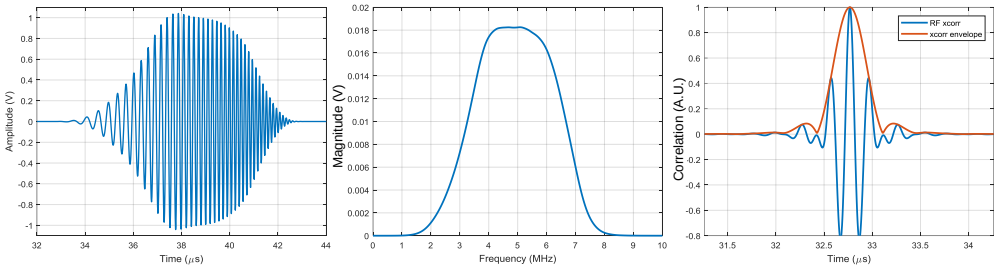

Fig. 1.27. Transducer output when tapered chirp signal is used for excitation (left), resulting signal spectrum (center) and the correlation function (right)

It can be seen that near-range sidelobes are still present. Reduction of the near-range sidelobes can be accomplished using mismatched filtering. Refer to Fig. 1.28 for mismatched filtering results of the same data when the Dolph-Chebyshev window was used to create the mismatched reference signal.

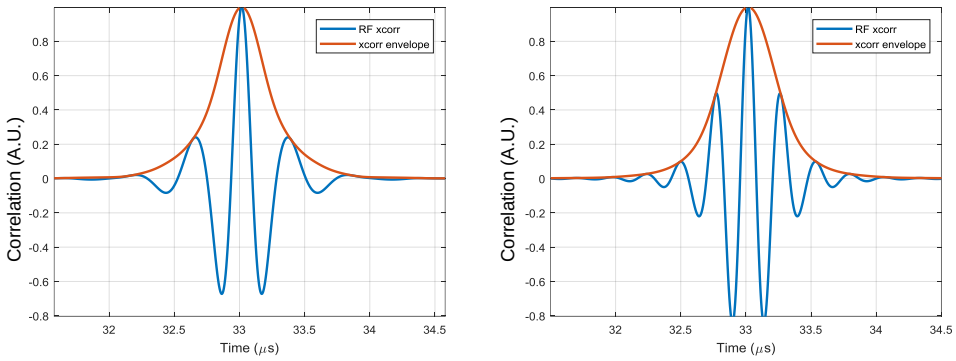

Fig. 1.28. Correlation function in case of mismatched filtering: results for excitation signal (left) and transducer output (right)

It should be noted that such SS signals correspond to arbitrary waveform and therefore a DAC and highly linear power amplifier are needed for such signal

excitation, which complicates the acquisition electronics. Furthermore, the majority of time the signal amplitude is not at the full available swing (Fig. 1.25 left).

Usually, the excitation signal is selected without accounting for the transducer influence. Not only a portion of the signal energy is lost (compare Fig. 1.25 left and Fig. 1.24 left) but the correlation and spectral properties remain unpredictable. It is worth reminding that smooth and wideband spectral response is especially important in spectroscopy [60].

Chimura et al. proposed to use amplitude modulation to compensate for the spectral losses [36]. Such approach allows to achieve an ideal compensation, but significantly reduces the economy of the excitation because the full analog amplifier voltage swing cannot be exploited. It was proposed in [37] to use the combination of amplitude and frequency modulation to improve excitation efficiency.

1.6. Rectangular excitation signals

Chirp or nonlinear chirp excitation seems the most effective form of excitation, since sinusoid amplitude can be selected to be at the full swing of the power amplifier. Still, such an approach requires a DAC and linear power amplifier, which increases the acquisition system weight, size and cost. Pollakowski and Ermert expanded the idea of nonlinear frequency modulation [18] by using the nonlinear pseudo-chirp for excitation (rectangular version of sinusoidal chirp). Use of such a pseudo-chirp explores better the swing of the excitation electronics, as the fundamental harmonic amplitude is 1.3 times large than the pseudo-chirp amplitude. Furthermore, the excitation electronics are more efficient (switch mode operation of the output stage) and less complex [61]. Therefore, the cost, weight and size of the acquisition electronics are reduced. Then, the analog version of the aforementioned signals can be converted into rectangular ones [25] (Fig. 1.29).

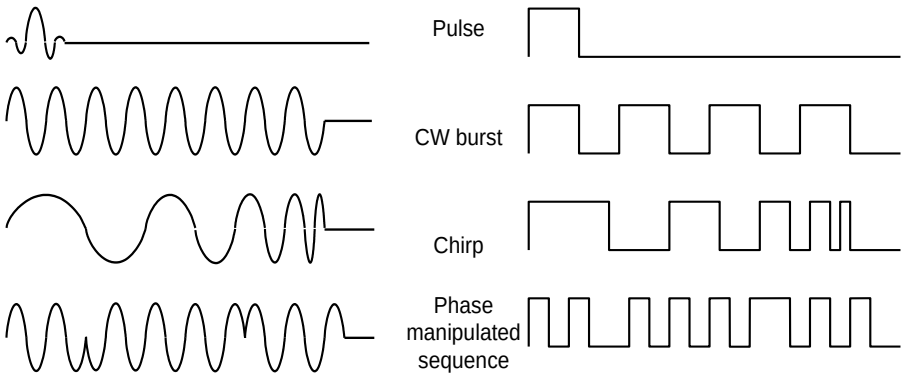

Fig. 1.29. Proposed analog (left) excitation signals conversion to rectangular (right)

Pollakowski and Ermert proposed to match the magnitude of the excitation signal to the transducer transfer function [18], improving both the resolution and SNR at reduced SLL. This thesis expands this idea further: rectangular signals are aimed and optimization is accounting for the complex transfer function of the complete system.

1.7. Conclusions of the 1st chapter

The signal energy, the effective and envelope bandwidth and the noise level define the quality of the measurement. The electronics and the transducer limit the excitation amplitude, noise floor and bandwidth. Pulse, step and toneburst are simple yet non-compressible signals. The simplicity of the electronics required for pulse signal generation and the ease of results interpretation are the main reasons for its wide usage and this property should be retained. Unfortunately, the spectral shape of simple signals is not flat, and the bandwidth is tied with energy. Furthermore, a large part of the spectral content is outside of the transducer passband. These properties tamper with the simple signals application in high fidelity measurements.

On the other hand, spread spectrum signals offer independent control over energy and bandwidth. Furthermore, some SS signals offer spectral shape control. Unfortunately, SS signals bring additional problems: the spectral shape for PSK and LFM signals is fixed, some SS signals (like LFM) have high correlation sidelobes, not all signals can be realized practically and the complexity (so the size, losses and cost) of the excitation electronics increases if arbitrary waveforms are required (in case of harmonic waveform, envelope tapering or amplitude modulation).

It has been shown that some SS signals can be converted into rectangular waveform. Such signals explore better the output swing of the excitation (fundamental harmonic amplitude is 1.3 times larger), and the excitation electronics are more efficient (switch mode operation of the output stage) and less complex, therefore the cost, weight and size of the acquisition electronics is reduced. Yet it remains unclear what properties can be obtained and how these signals behave in actual applications.

Next chapter is dedicated to study the rectangular versions of existing signals in ultrasound applications and rectification of the desired signal properties.

2. RECTANGULAR SPREAD SPECTRUM SIGNALS IN APLICATIONS

SS signals can be converted into rectangular waveform. The aim of this chapter was to investigate how rectangular SS signals behave in ultrasonic imaging and measurement applications, what properties can be obtained, and what properties are required. SS signals advantage over simple (pulse and toneburst) signals have been demonstrated.

2.1. Subsample ToF estimation in digital domain

Time of flight was used as quality metrics throughout the majority of applications analyzed below. ToF estimation techniques and errors expected have been presented in chapter 1.1. Modern ToF estimation is carried out in the digital domain; therefore the discrete version of cross-correlation function x_m is used:

$$x_m = \sum_{k=1}^{K} r_{k-m} \cdot s_k \ , \tag{2.1}$$

where r is the reference signal and s is the received signal. Then ToF estimate is:

$$ToF_{DC} = \arg\left[\max(x_m)\right]. \tag{2.2}$$

Expected ToF accuracy is higher than the sampling period due to high SNR of SS signals, therefore subsample interpolation (Fig. 2.1) has been used [40].

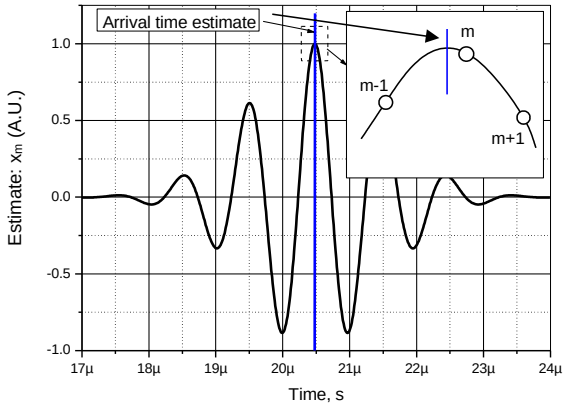

Fig. 2.1. Interpolation of the correlation function peak for subsample estimation of the TOF [17]

The *ToF* estimate was treated as the sum of the rough estimate ToF_{DC} obtained using correlation function and the subsample correction ΔToF:

$$ToF = ToF_{DC} + \Delta ToF \ . \tag{2.3}$$

In an ideal case, interpolation should use the *sinc* function to obtain the subsample correction ΔToF. However, for faster processing speed, truncated versions where used to obtain correction ΔToF instead of using *sinc* interpolation.

Parabolic interpolation [40] used three points around the peak m (x_{m-1}, x_m and x_{m+1}) for subsample correction ΔToF_p:

$$\Delta ToF_p = -\frac{b}{2af_s} = \frac{x_{m-1} - x_{m+1}}{2f_s\left(x_{m-1} - 2x_m + x_{m+1}\right)}. \tag{2.4}$$

Subsample correction ΔToF_{cos} for cosine interpolation function [40] was:

$$\Delta ToF_{\cos} = -\frac{\theta}{f_s\omega_0},\ \omega_0 = \arccos\left(\frac{x_{m-1} + x_{m+1}}{2x_m}\right),$$
$$\theta = \arctan\left(\frac{x_{m-1} - x_{m+1}}{2x_m \sin\omega_0}\right). \tag{2.5}$$

Interpolation using phase spectrum [40] was considered as ideal:

$$\Delta ToF_{FFT\phi} = \frac{\sum_{m=1}^{M} \frac{\phi\left(X^0{}_m\right)\cdot\left|X^0{}_m\right|^2}{\omega_m}}{M\sum_{1}^{M}\left|X^0{}_m\right|^2}. \tag{2.6}$$

Parabolic interpolation is the fastest, it was found to produce the lowest random errors but exhibits the highest bias errors. Cosine interpolation is of comparable speed and has lowest bias errors [41] but slightly higher random errors. Interpolation using phase spectrum requires a much longer processing time, but is free from bias errors. It has significantly higher random errors.

2.2. Composite cure monitoring

Manufacturing of composite products involves the curing procedure. It is important to establish the moment when epoxy of the composite is cured, so the mold can be released for the next part of the production. Usually this is done by multiple trials, which increases manufacturing time and production waste. While transitioning from viscous liquid to rigid and highly cross-linked polymer, solid epoxy goes through three phases: liquid, gelation and solidification. These phases are hard to spot in a nonintrusive way. Ultrasound velocity, attenuation or non-linearity can be used to make the decision [87]. The experiment presented below used the velocity for composite cure monitoring, because it can be easily established from the ToF measurement [62]. Ultrasound velocity is obtained as:

$$c_{epox} = \frac{L_{epox}}{ToF}, \tag{2.7}$$

where ToF is the ultrasonic signal propagation time and L_{epox} is the distance traveled in the epoxy. A dual component epoxy system was analyzed: XB3404-1 hardener and Araldite LY1564 base. Refer to Fig. 2.2 for the experiment setup. Two 2 MHz center frequency transducers TF2C6N (from Doppler Inc.) were placed against each other at

a 5 mm distance. Excitation was carried out using a bipolar pulser SE TX07-00 [20]. The received signal, after being conditioned with a programmable gain block, was digitized using a 100 Ms/s 10 bit acquisition system [14].

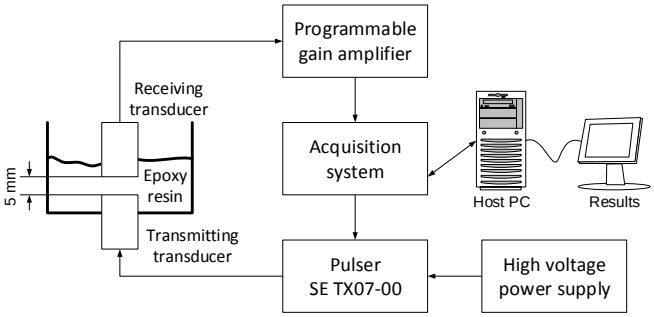

Fig. 2.2. Epoxy cure monitoring experiment setup

Fig. 2.3 shows the four signals used in the experiment: a 2 MHz 3 μs toneburst, 250 ns pulse, 3 μs narrowband (0.7-3.5) MHz and wideband (0.5-5) MHz 3 μs chirp.

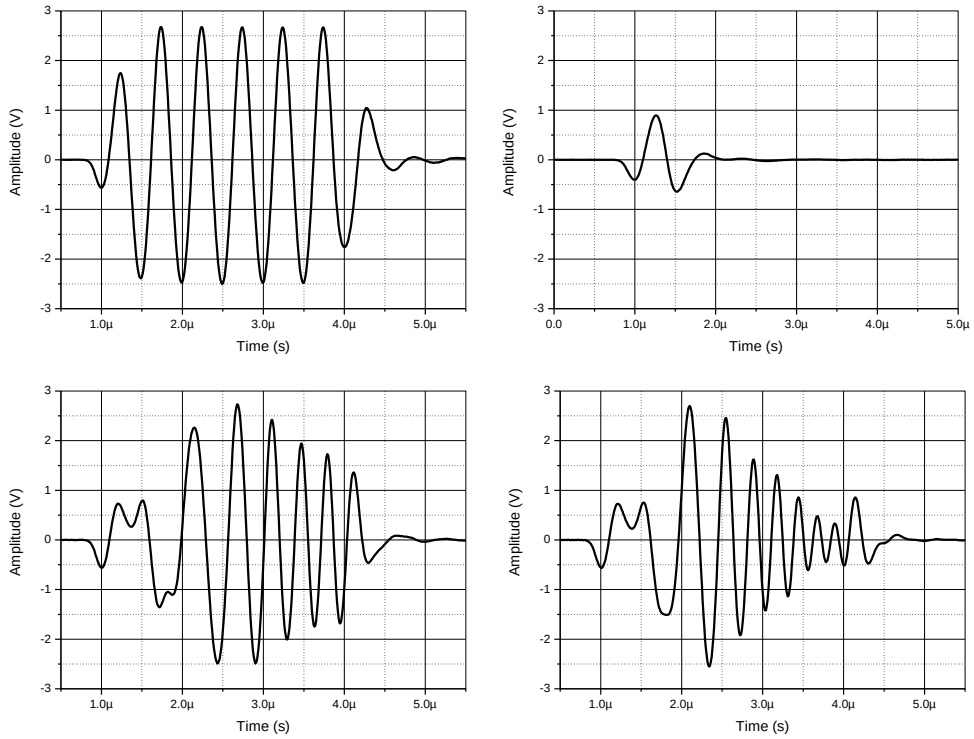

Fig. 2.3. Received signal, when excited with toneburst (top left), pulse (top right), (0.5-5) MHz chirp (bottom left) and (0.7-3.5) MHz chirp (bottom right)

Two transducers were placed face to face and the through transmitted signal was recorder as the reference. Then the transducers were covered by protective scotch tape in order to avoid damage from the epoxy adhesion and placed at a 5 mm distance. The

curing process was deliberately slowed down by performing the experiment at room temperature instead of the specified 80°C. In this way, thermal damage to the transducers was avoided. Signals recorded during the experiment were used to calculate ToF using cross-correlation with the reference signal. In this way, the ToF bias in electronics and transducers was eliminated. The experiment was carried out for 144 h. The obtained ToF was converted to ultrasound velocity in the epoxy using the following equation (2.7) (refer Fig. 2.4).

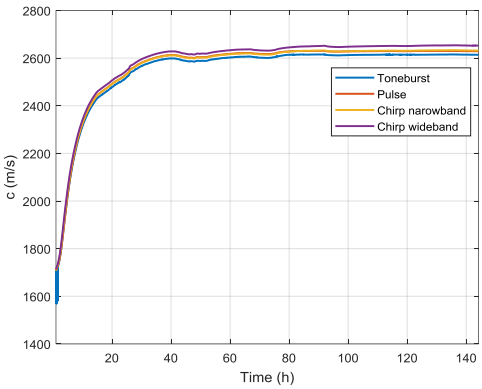

Fig. 2.4. Ultrasound velocity variation during epoxy curing

From the analysis of Fig. 2.4 results it can be concluded that the transition from liquid state (1700 m/s -1900 m/s) to gelation state (1900 m/s to 2500 m/s) can be clearly distinguished, but the solidification phase has a slow convergence to 2650 m/s. Since the decision about a sufficient solidification is done at a slightly varying region of the velocity curve, it is important to ensure high accuracy of ToF estimation. Therefore, it is important to have low random errors of ultrasound velocity estimation.

Four different type signals (Fig. 2.3) were used in order to evaluate which signal gives the best measurement accuracy. Toneburst signal was selected with the assumption that it will be able to concentrate the majority of the excitation energy into the transducer passband, but its correlation function is not sharp, therefore subject to abnormal ToF estimation errors. Pulse signal is relatively wideband but has low energy. Low frequency narrowband (0.7-3.5) MHz 3 µs chirp has good energy concentration into the transducer passband. Wideband (0.5-5) MHz 3 µs chirp has energy spread beyond the transducer passband (wider effective bandwidth is expected), but has lower energy than the narrowband chirp.

Results in Fig. 2.5 were filtered using an unbiased moving average filter in order to rectify the ultrasound velocity trend:

$$c_{epoxAvg_n} = \frac{1}{M} \sum_{m=-\frac{M}{2}}^{\frac{M}{2}} c_{epox_{(n+m)}}, \tag{2.8}$$

where M is filter order, $c_{epoxAvg_n}$ is the moving average filter output for n-th sample. A sliding 1 h window was used (M=50) to extract the average velocity value. This filter

output was considered as a random error-free measurement result. To obtain the measurement error, the filter result was subtracted from the original ultrasound velocity:

$$err(c)_n = c_{epox_n} - c_{epoxAvg_n}. \tag{2.9}$$

Random errors evaluation results are presented in Fig. 2.5.

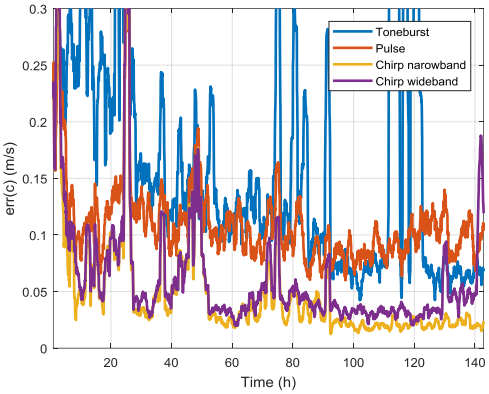

Fig. 2.5. Random errors during epoxy curing process monitoring

From Fig. 2.5 it can be concluded that the toneburst signal exhibited the highest abrupt errors. As expected, SS signals outperformed the pulse signal due to their wide bandwidth and higher SNR. Narrowband chirp, matching transducer passband, had slightly lower random errors than the wideband one. In the case of toneburst, the random errors were less than the SS signal, until attenuation influence reduced the relative noise margin. Then large anomalous errors occurred due to the correlation peak shift to sidelobe. It should be noted that the chirp spectrum does not match the transmission function shape, therefore its correlation sidelobes are high. It is desirable to use a signal whose spectrum is matched to the transmission; so sidelobes are lower.

2.3. Systematic errors reduction in flow velocity measurement

The transit time of the ultrasonic pulse can be used to measure the flow velocity [63]. With two ultrasonic transducers placed at the ends of the measured flow (Fig. 2.6), there is a difference in the ultrasound propagation time (ToF) between upstream and downstream signals.

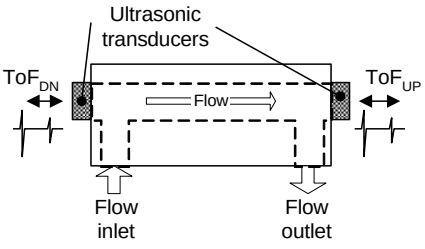

Fig. 2.6. Transit time flow measurement setup [8]

Then, ultrasonic signal sent against the flow will take a longer ToF_{up} than the signal send down the flow ToF_{down} [63]:

$$ToF_{up} = \frac{L}{c - v}, \tag{2.10}$$

$$ToF_{down} = \frac{L}{c + v}, \tag{2.11}$$

where c is the ultrasound speed in the measured liquid, L is the distance between transducers and v is the velocity of the measured flow.

Assuming that the whole ultrasonic beam is matched with a flow, the mean liquid velocity v can be obtained as [63]:

$$v = \frac{L\left(ToF_{up} - ToF_{down}\right)}{2 \cdot ToF_{up} \cdot ToF_{down}}. \tag{2.12}$$

The correlation peak position was used as the ToF estimator, using in this case a parabolic interpolation for the ToF subsample estimation.

The excitation used was of low voltage (4V pp), the received signals were amplified to 30 dB and digitized with a 100 Ms/s 10 bit acquisition system [14]. The whole experiment setup is presented in Fig. 2.7.

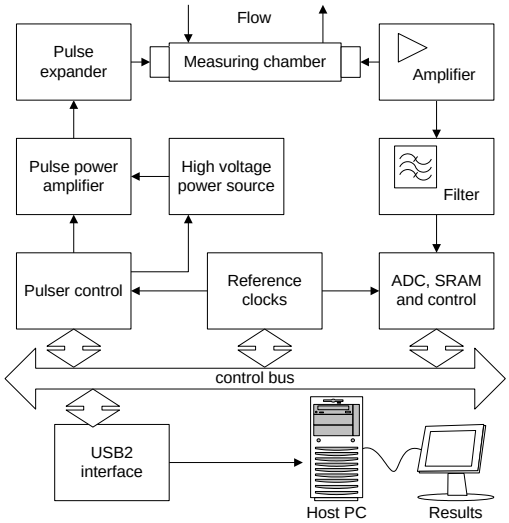

Fig. 2.7. Flow measurement bias errors investigation experiment setup

Differential ToF dominates in equation (2.12):

$$\Delta ToF = ToF_{up} - ToF_{down}. \tag{2.13}$$

ΔToF is most affected by the variability of the transfer function of the ultrasonic transducer. Therefore experimental investigation was focused on the analysis of the differential ToF.

At high flow rates, the ΔToF is dominated by the flow influence, but at low flow rates it becomes extremely sensitive to any asymmetry in signal propagation. In order to eliminate the liquid ultrasound velocity variation with temperature, the experiment was carried out with transducers in direct contact and the arrangement was placed on a heating plate. After starting the acquisition, heating was turned on and the temperature increased from 20°C to 44°C.

In the research presented in [8], it was indicated that variations in the complex transfer function of the ultrasonic transducer creates a bias error in the ToF estimation, which in turn increases the flow measurement errors if the flow velocity is small. The experiment presented below is based on the assumption that the variability of the transfer function of the ultrasonic transducer can be reduced if wideband signals are used for excitation.

Three types of signals were used: narrowband but high energy (toneburst), wideband with high energy (chirp) and wideband but low energy (pulse and step). Both chirp and toneburst signals had high energy due to their long duration: 30 μs duration spread spectrum (chirp) and toneburst signals. Though of similar energy, their spectral content was different (refer to Fig. 2.8 for spectral comparison).

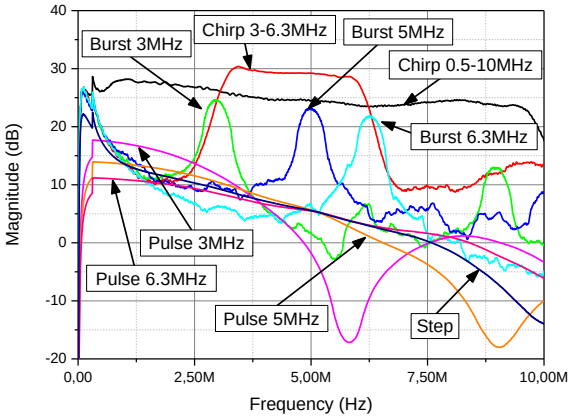

Fig. 2.8. Spectrums of the signals used in experiment

Two types of chirp signals were used: (3-6.3) MHz, covering the transducer passband and (0.5-10) MHz, exceeding the passband. Three toneburst signals were used: 5 MHz, matched center frequency, 3 MHz, lower than center frequency and 6.3 MHz, higher than center frequency, all within the passband. Step and pulse signals are wideband, but slightly more energy is concentrated at low frequencies (refer to Fig. 2.8). All nine signals were acquired sequentially with the period of one second, and the ToF was estimated. Fig. 2.9 shows the variation of the ΔToF in the case of excitation with high energy signals (Fig. 2.9 left) or low energy signals (Fig. 2.9 right).

Results indicate that the best performance was obtained for the spread spectrum (chirp) signals, for which the thermal trend over 20°C range is only 50 ps. It is worth pointing out that the wideband chirp (beyond transducer passband) trend was of

opposite polarity than that of the chirp covering the passband. As expected, step and pulse signals exhibited significantly larger random errors and bias errors.

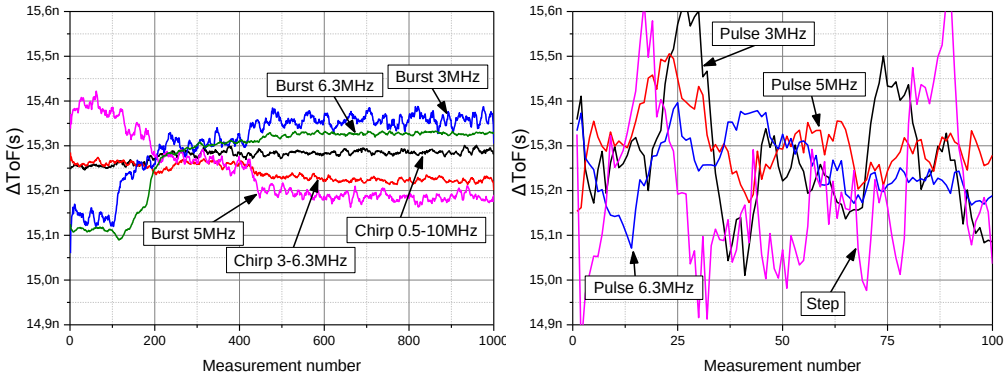

Fig. 2.9. Signal SNR influence on ToF offset: high SNR (left) and low SNR (right) signals comparison

It can be concluded that temperature effect on the ToF bias errors is minimized and random errors are minimized when high SNR wideband SS signals are used. It can be explained because the SS signals avoid resonances. Pulse excitation possess resonant properties (positive and negative fronts) which can be adjusted to match the transducer center frequency (approximately half of the period), but due to temperature or loading effects this frequency changes, causing significant bias errors in the amplitude and ToF measurement [8]. However, it remains unclear what results are obtained if the signal was able to provide a bandwidth match or spectral losses compensation.

2.4. ADC dynamic range influence on ToF errors in case of SS signals

Signal dynamic range *DR* defines the ADC resolution (bits) [63]:

$$b = \frac{DR - 1.76}{6.02}, \tag{2.14}$$

$$DR = 20\lg\left(\frac{U_m}{\sigma_n}\right), \tag{2.15}$$

where U_m is peak signal amplitude, σ_n is noise rms value. If the signal energy is spread in time, as is the case with SS and toneburst signals, lower SNR is obtained.

Noise energy is spread over time and frequency. Meanwhile, energy of the pulse excitation is concentrated at one time instant. Therefore, a large dynamic range of the incoming signal is obtained and acquisition requirements (ADC resolution) are high. An assumption has been made that the dynamic range of the SS signal is lower due to energy spread in time. Therefore, ADC resolution can be reduced due to the lower initial *DR*, which is used to calculate the ADC resolution. After the acquisition, SNR

is increased due to the processing gain of the correlation function, so similar results should be obtained using lower ADC resolution.

An experiment has been carried out to confirm such an assumption. Refer Fig. 2.10 for experiment explanation.

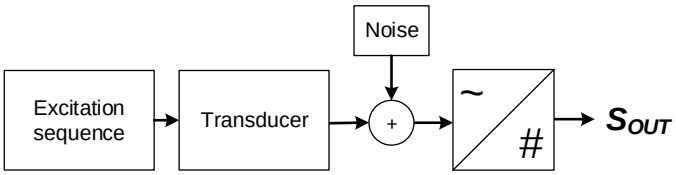

Fig. 2.10. Experiment structure for SS signal influence on ADC dynamic range evaluation

The ultrasonic transducer was simulated by a passband filter with 5 MHz center frequency and 80 % bandwidth. The excitations used were a 100 ns pulse (matched to 5 MHz frequency) and a (0.1-10) MHz 10 μs chirp.

Noise was added to the signal at the transducer output and then the signal was digitized using a 4 to14 bits ADC. The resulting signal was used to estimate the ToF using equations (2.5) and (2.3). The obtained ToF was processed to extract the random errors using:

$$\delta = \sqrt{\frac{\sum_{i=1}^{N}\left(x_i - \bar{x}\right)^2}{N-1}}\,. \tag{2.16}$$

Refer to Fig. 2.11 for ToF estimation of random errors obtained at -50 dB SNR (equation (2.15)).

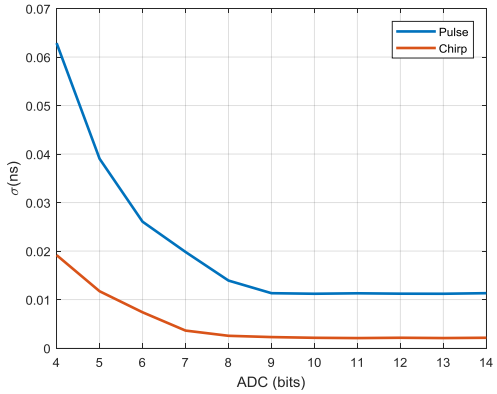

Fig. 2.11. Radom errors of ToF estimation in case of chirp and pulse excitation

It can be seen that the use of SS for excitation reduces the signal dynamic range, which in turn allows the use of a lower ADC resolution. Detailed examination of ToF errors in the case of 8 bit ADC resolution and the same SNR as in Fig. 2.11 is presented as *lagplot* in Fig. 2.12.

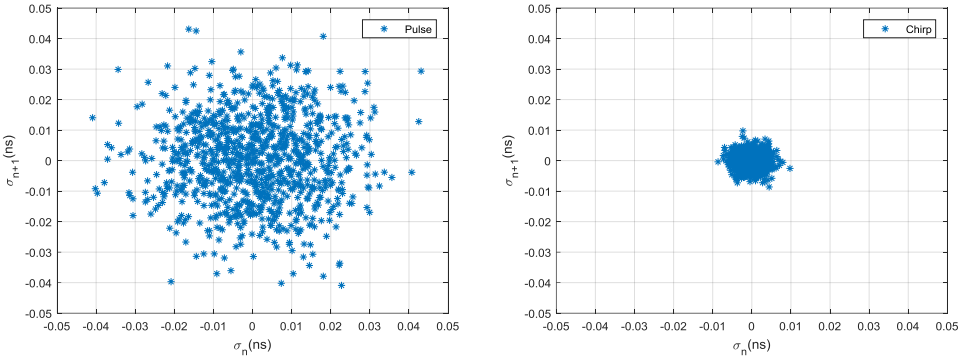

Fig. 2.12. *Lagplot* of the ToF errors in case of pulse (right) and chirp (left) excitation

It can be concluded that SS allow to reduce the dynamic range of the signal, therefore a reduction of the required ADC bits is possible.

It is notable that the single pulse amplitude has to be high in order to maintain the energy, therefore not just achieving excitation voltage is problematic but also the nonlinearity effects in propagation media and electronics are increased. Alternatively, the SS signal can be spread over a long period in time so instantaneous amplitude is much lower. As a consequence to this reduced amplitude, the nonlinearity effects in propagation media (as well as in electronics) are minimized [6].

2.5. Electromagnetic interference reduction using SS signals

Electromagnetic interference (EMI) is unavoidable in ultrasonic testing. The essential path for EMI propagation is the cable, used to connect the ultrasonic transducer. Usually it has to be flexible (i.e. small wire diameter, low percentage of shielding braid; thin, single layered braid) and coaxial. While providing significant protection against RF interference at high frequencies, coaxial cables are not a suitable alternative at the (0.1-10) MHz range because of braid quality issues [65].

The situation is further complicated by the growing use of SMPS (Switched-mode power supply): laptops, main supply for equipment, and the high voltage supply for excitation. Automated NDT complicates the situation further: step or brush/brushless motors are used to move the transducer across the inspection surface. Half or full bridge output is usually used to drive the motor. Every transition of the SMPS or motor drive creates a current spike in the cables. However, since the same umbilical cable usually carries the coaxial cable for transducers and control for motors, and is long (can reach 100 m), significant EMI is coupled to the signal cable. Unfortunately, this EMI is similar to the signal used for transducer excitation (both pulse and spike).

EMI problems may cause problems in the products monitoring systems, which are in factories where high current motors, heating elements or other equipment are installed. The experiment below is used to analyze the EMI problem. Cheese production process monitoring in a thermally stabilized chamber was investigated. Cheese production involves milk curdling, when protein molecules attract one another

and form clumps due to the changes in pH of their solution. It is important to start the cutting of the curd before the clumping reaction is complete. This decision is usually made manually, but the process can be automated if ultrasonic monitoring is used. Ultrasound velocity and attenuation change significantly during the curdling process, therefore a system can be used in the same way as in chapter 2.2. Curdling occurs more rapidly at warmer temperatures, therefore the milk was placed in a thermally stabilized chamber during the experiment. Refer to Fig. 2.13 for chamber details.

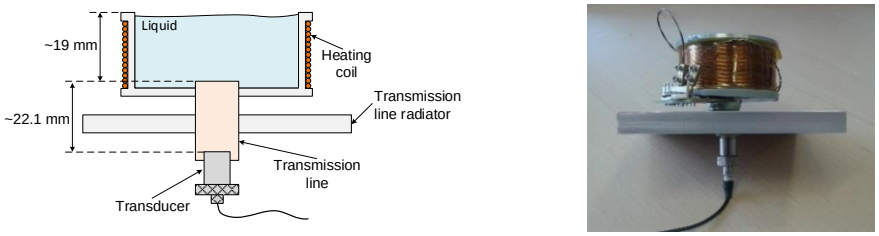

Fig. 2.13. Experiment setup (left) and measurement chamber (right)

The heating element used for temperature control is very close to the measuring channel. The amount of heat is controlled by pulse width modulation (PWM). These signals have sharp rise and fall times which create EMI (Fig. 2.14) despite the delay line used with an additional aluminum radiator.

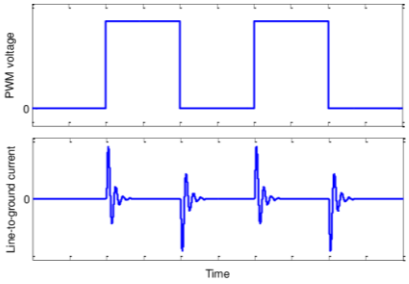

Fig. 2.14. Driving PWM signal (top) and EMI created (bottom)

Signal attenuation in milk gets very high at the end of curdling, therefore high gain was used in the receiving channel. High gain and the sharp PWM edges caused significant EMI. The setup of the experiment is presented in Fig. 2.15.

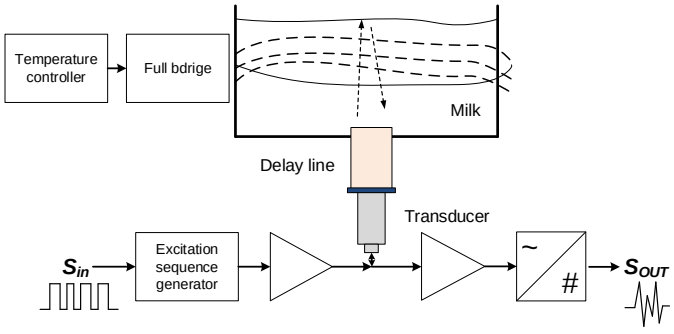

Fig. 2.15. Cheese curdling experimental setup, when EMI was encountered

Ultrasound excitation has been done using a bipolar pulser SE TX07-01 [20], combined with a temperature control system SE HEATER-01-00. The excitation voltage was 10V pp, and received signals were amplified to (30-60) dB and digitized by a 100 Ms/s 10 bit acquisition system [14]. The transducer (5 MHz TF5C6N from Doppler Inc.) was used in reflection mode, were the reflection from the milk surface was registered. Ultrasound path lies thought two materials: the transmission line and curdling milk (Fig. 2.16 left). Ultrasound velocity was measured using ToF between the liquid surface and transmission line (Fig. 2.16 right).

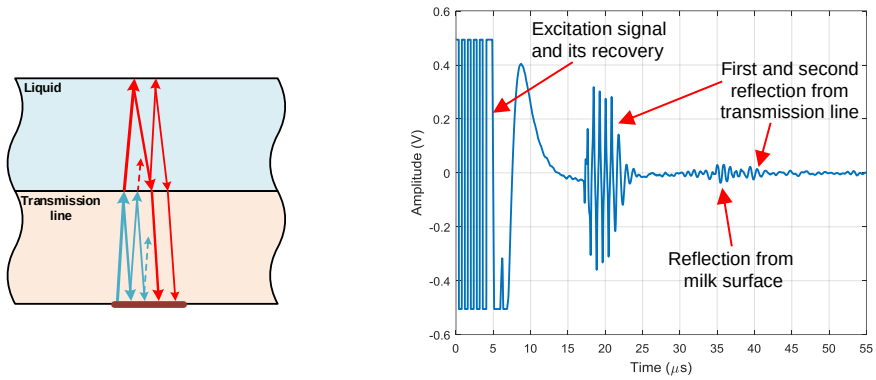

Fig. 2.16. Signal path (left) and the corresponding signal obtained (right)

It can be seen that the reflection from the milk surface is relatively weak and can be easily disturbed by EMI. Four signals were used in the experiment: a 5 MHZ pulse, a 5 MHz 1 µs toneburst, a (3-7) MHz 1 µs chirp and a (3-7) MHz 3 µs chirp. Refer to Fig. 2.17 for spectrum comparison of the excitation signals.

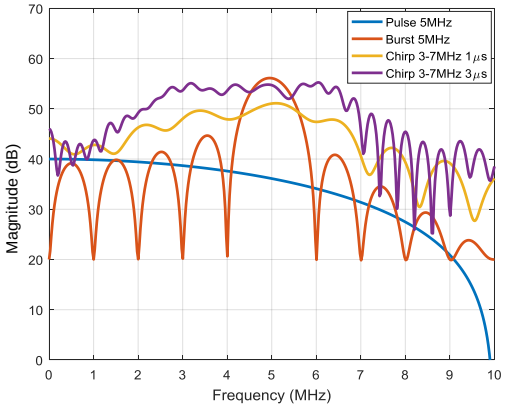

Fig. 2.17 Excitation signals spectrum, used in cheese curdling monitoring

It can be seen that the spectral density of the pulse signal is the lowest, yet this signal exhibits a wide bandwidth with a large portion of energy concentrated at low frequencies. Toneburst has the highest spectral density at 5 MHz, but the narrowest bandwidth. This signal should have the best propagation through the transducer, because it corresponds to the transducer center frequency. Long chirp has almost the

same spectral density as a toneburst at 5 MHz because it is three times longer. It is essential that the long chirp has a wide bandwidth which covers the transducer passband at -20 dB. Short chirp has the same wide bandwidth with lower energy, just 6 dB of that of the long one. Pulse excitation waveform is very similar to EMI, while toneburst and chirps differ from EMI pulses. Refer to Fig. 2.18 for examples of EMI induced by PWM.

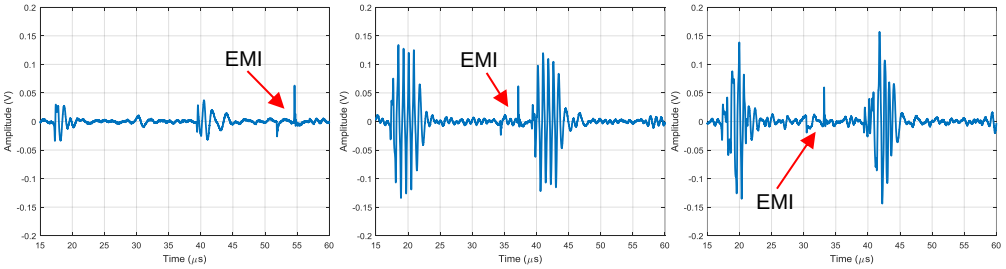

Fig. 2.18. EMI induced by PWM of the heating element in case of pulse (left), toneburst (middle) and short chirp (right) excitation signals

It can be seen that the EMI signal amplitude is higher than the pulse but lower than the long signals. These EMI pulses can cause errors in ToF estimation. Fig. 2.19 demonstrates the ultrasound velocity variation during the experiment.

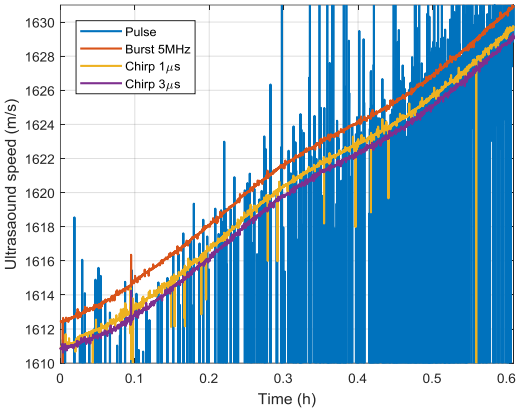

Fig. 2.19. Measured ultrasound velocity in curdling milk in case of EMI presence for various probing signals used

Abrupt velocity measurement errors occur in the case of pulse excitation, while toneburst and chirp excitation provide more robust results. It is also notable that toneburst has an offset in the measured ultrasound velocity. The shape of the pulse signal is the same as the EMI generated by the heating element. Pulse amplitude has to be high in order to exceed the EMI energy, while the SS signal can be spread over a very long period and not requiring high amplitude. Furthermore, the SS signal correlation with the EMI signal is much lower. The toneburst also exhibited a high EMI immunity, but the efficiency of the toneburst will decrease during curdling. Therefore, anomalous errors will appear due to the increased attenuation and relative

noise margin reduction. It can be concluded that the use of SS signals for excitation allows a reduction in the EMI influence.

2.6. Imaging using time of flight

Time of flight can be converted into traveled distance and then be used for imaging. In order to analyze the effect that the type of excitation has on the resulting quality of the imaging, a simple experiment was designed, in which a coin is scanned to obtain ToF images of both surfaces. A 25 mm diameter coin was immersed in water. The sample was hanging on two steel supports at 25 mm distance from the transducer surface; which corresponds to the focal distance. An area of 25x25 mm was scanned using 200 μm steps. A 20 MHz (6 mm diameter) transducer IRY120 from NDT Transducers was used, and a wideband, 1 μs duration chirp ranging from 10 MHz to 30 MHz and 20 ns pulse were used for excitation. The excitation amplitude was 5 V. Front face (top) and backwall (bottom) surfaces are presented in Fig. 2.20. Note the better reconstruction of the small details in the case of chirp excitation. It can be seen that the backwall reconstruction quality is much better when the chirp excitation is used.

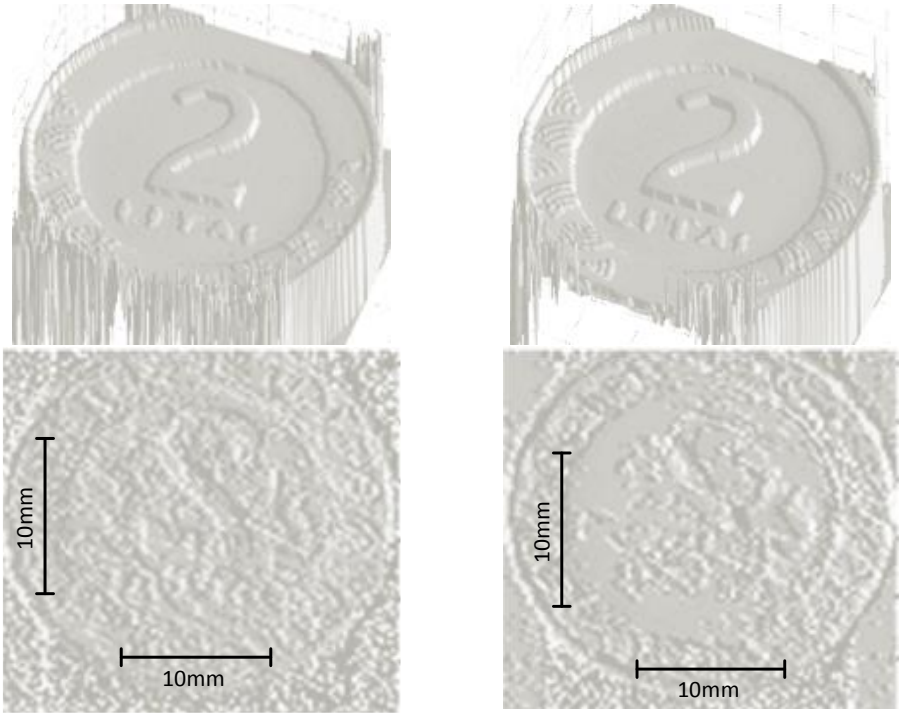

Fig. 2.20. Coin profile image obtained by time of flight estimation using same amplitude pulse (left) and spread spectrum (right) signals for excitation

It can be concluded that excitation using SS signals can be carried out using very low excitation voltages. However, correlation sidelobes cause ToF variation of neighboring reflections if thin samples are studied: therefore new rectangular SS signals with lower sidelobes are needed.

2.7. Spectroscopy using SS signals

It was shown in [64] that spectroscopy measurements can be done even in the case of overlapping reflections. It was concluded that both wide bandwidth and high SNR have to be ensured at resonances. The analysis below is aimed to demonstrate the superiority of SS signals in spectroscopy applications. Two investigations have been carried out: i) high porosity composite air coupled thickness measurement and ii) immersion imaging of the integrated circuit using a reflected signal spectrum.

The investigation presented below was aimed at analyzing how SS signals can be used to do the imaging beyond the transducer passband. Medium frequency (5 MHz) transducer was used for high frequency (up to 25 MHz) imaging using spectroscopy. The test object was a BGA chip STR710FZ2H6, which has 12x12 ball pins with 0.8 mm pitch on the bottom and is 10x10 mm size. Imaging was performed using an immersion setup, with a focused 20 MHz 6 mm diameter transducer IRY210 from NDT Transducers. An area of 12x12 mm was scanned using 50 μm steps. The sample was placed on a Plexiglas slab (Fig. 2.21) at the focal distance (19 mm).

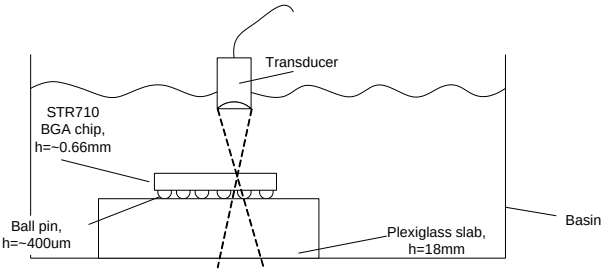

Fig. 2.21. Experimental setup used for integrated circuit imaging

Two +/-30 V amplitude rectangular signals were used: a wideband 1 μs chirp (5-35) MHz and a one period 16 MHz toneburst. It is essential that the excitation signal's bandwidth is much wider than the transducer passband. Spectroscopy at relatively low frequencies (7 MHz) reveal the internal structure (Fig. 2.22) and SNR is high for both signals.

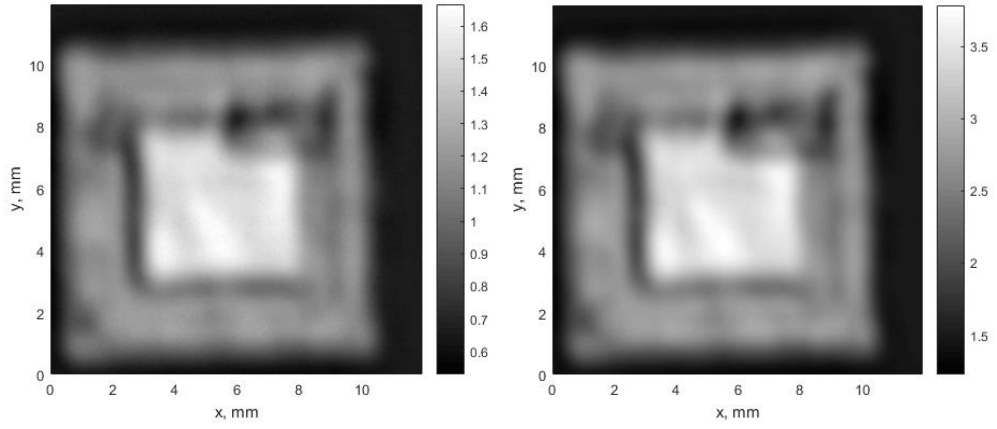

Fig. 2.22. Image at 7 MHz using toneburst (right) and chirp (left) excitation

Image obtained is low resolution, because the transducer beam width is just 0.7 mm at this frequency [39]. The transducer beamwidth is defined by the ratio of the wavelength and the transducer diameter, therefore resolution at higher frequencies should be better. At 20 MHz the transducer beamwidth is reduced three times (to 0.25 mm) and provide better details (Fig. 2.23).

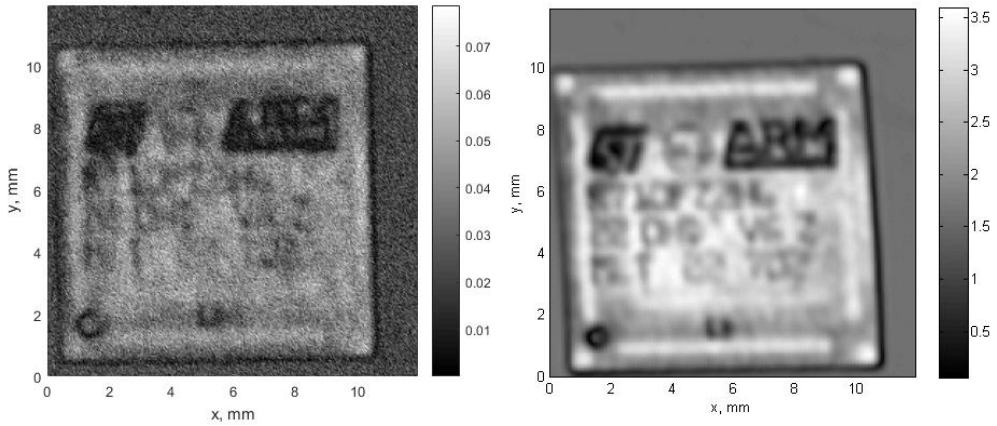

Fig. 2.23. Image at 20 MHz using toneburst (right) and chirp (left) excitation

It should be noted, that SNR is lower for toneburst, while chirp maintains high SNR. Toneburst spectroscopy image at 25 MHz (Fig. 2.24 left) is significantly masked by noise, while chirp is able to produce clear, noise-free image even at 32 MHz (Fig. 2.24 right).

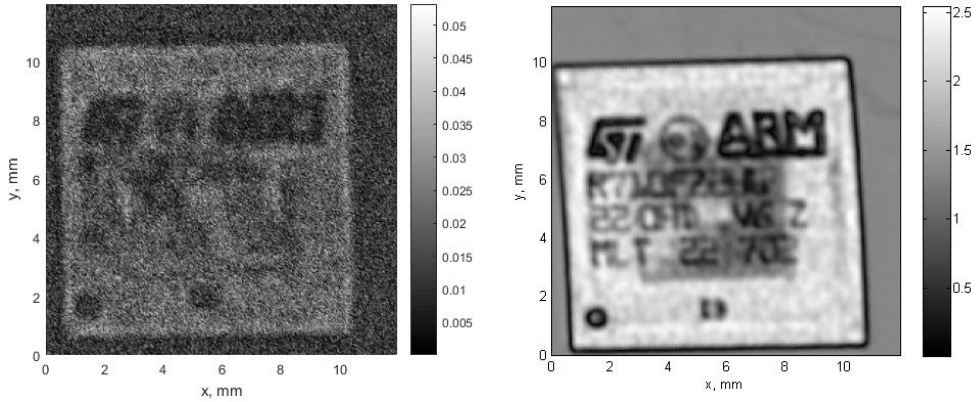

Fig. 2.24. Image at 25 MHz using toneburst (right) and at 32 MHz chirp (left) excitation

It should be noted that both 20 MHz and 32 MHz are beyond the transducer passband, yet imaging is still possible. It can be concluded that SS signal has better bandwidth coverage and better SNR, yet it has no possibility to program the spectral content of the excitation to compensate for transducer spectral losses.

Estimation of ToF in thin materials requires advanced signal processing techniques (deconvolution, inverse filtering, etc.), but it can be easily carried out using

resonant spectroscopy [64]. Material properties, like thickness, velocity, attenuation and density can be estimated.

Transmittance resonance spectroscopy uses signal s received with sample inserted (Fig. 2.25 right), normalized in the frequency domain by the reference s_R signal received without sample (Fig. 2.25 left):

$$T(\omega) = \frac{S(\omega)}{S_R(\omega)}. \tag{2.17}$$

Fig. 2.25. Measurement setup: without sample (left) and with sample (right)

Pulse signals are usually used, but wide bandwidth is not enough for such measurements in the case of composite materials with large structural noise: high energy is needed. Toneburst is narrowband, and therefore cannot cover the required bandwidth. SS signals are offering both properties. The experiment provided below was aimed at demonstrating this advantage. The measurements were carried out using two air-coupled wideband 0.6 MHz transducers. The sample under analysis was a high porosity glass fiber reinforced plastic (GFRP) sample milled to different thickness steps (Fig. 2.26).

Fig. 2.26. GFRP sample used in experiments

The thickness of the steps was measured using a digital caliper before the experiment (Table 2.1). This thickness was used to estimate the first resonance frequency, assuming 2600 m/s velocity.

Table 2.1. Measured material thickness and estimated first resonance frequency

Step No.	Thickness (mm)	f_0 (MHz)
1	0.85	1.53
2	1.75	0.74
3	2.75	0.47
4	3.85	0.34
5	4.60	0.28
6	5.70	0.23
7	6.70	0.19
8	6.75	0.189

Three different excitation signals were used in the experiment: a pulse matched to 750 kHz, a chirp 30 µs and a chirp 100 µs. The excitation was 200 V and the reception channel gain was 69 dB. Material attenuation is very high due to porosity (refer Fig. 2.27, Fig. 2.28 and Fig. 2.29 for 6.7 mm thickness of case data), therefore spectroscopy data has a low SNR (labeled as "Transmission", orange curve).

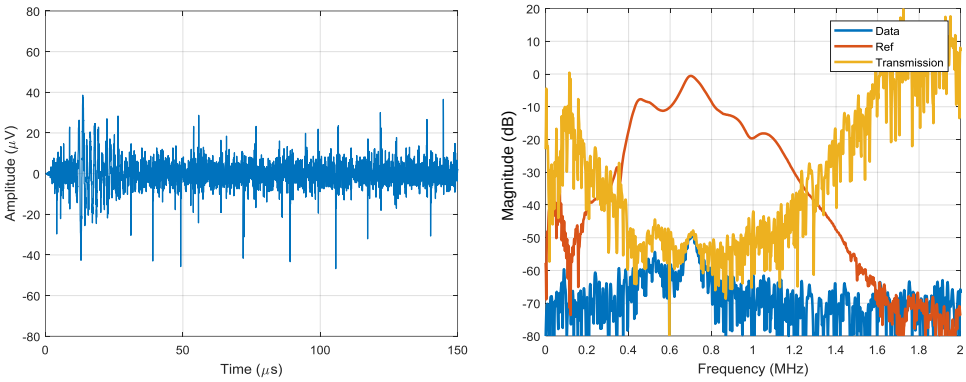

Fig. 2.27. Through transmitted signal (left) and its spectrum (right) for the 6.7 mm thick composite when pulse optimized for 750 kHz was used for excitation.

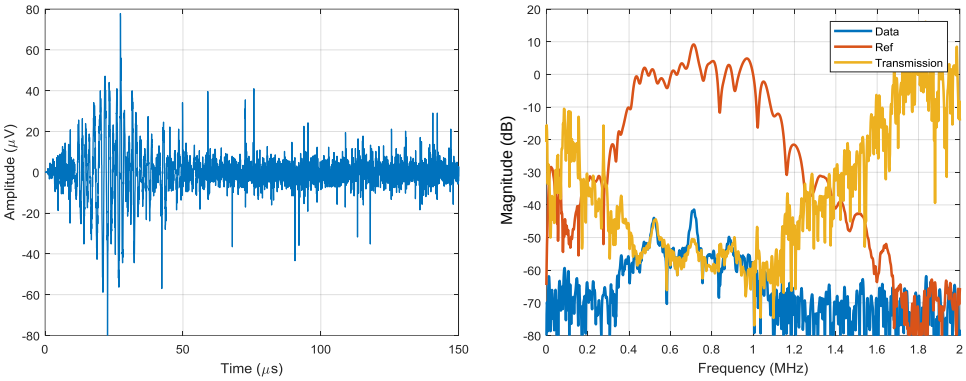

Fig. 2.28. Through transmitted signal (left) and its spectrum (right) for the 6.7 mm thick composite when 30 µs chirp was used for excitation

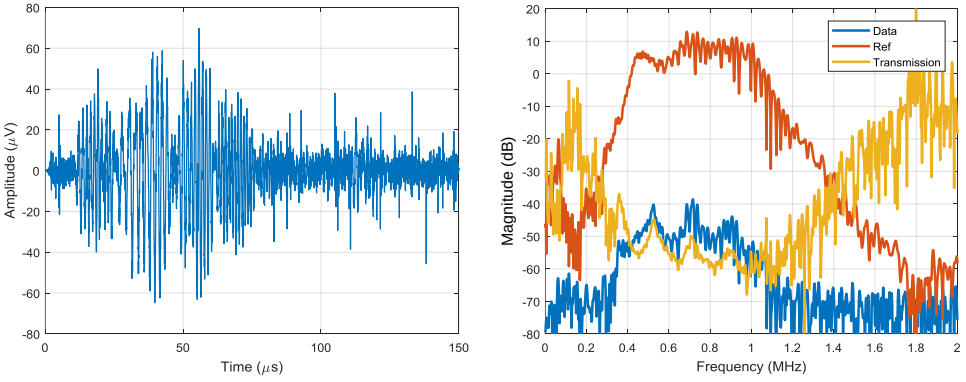

Fig. 2.29. Through transmitted signal (left) and its spectrum (right) for the 6.7 mm thick composite when 100 µs chirp was used for excitation

Measurements without sample (labeled as "Ref", red curve on right figures) and measurements with sample inserted (labeled as "Data", blue curve on right figures) are 50 dB lower in case of 6.7 mm thickness.

In all cases, it is very difficult to identify the signal without data averaging. Measurements at every thickness were repeated 100 times, so that result errors can be estimated. It can be seen that only one resonant peak (orange curve) can be barely visible in the case of pulse excitation (Fig. 2.27), while four resonant peaks can be located in the case of long chirp excitation (Fig. 2.29). The obtained transmission function was used to fit the layer model (inverse solution in [64] equations (1.18), (1.20)) in the range from 0.4 MHz to 0.9 MHz. Fig. 2.30 shows the results variability for velocity (left) and thickness (right) for all 100 measurements.

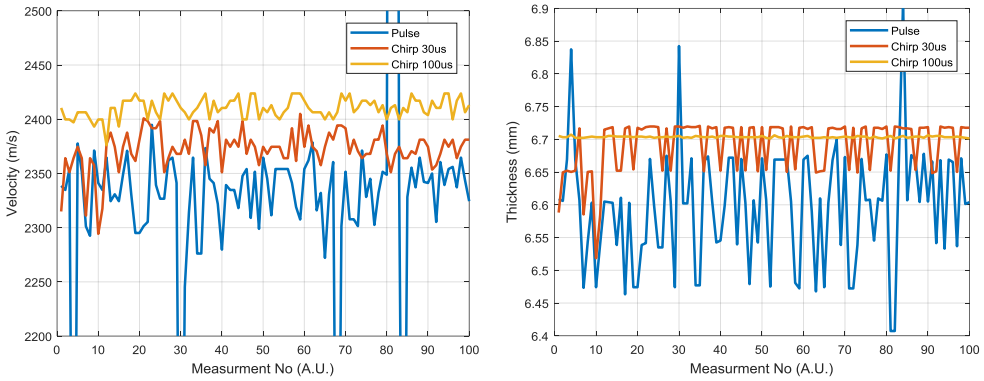

Fig. 2.30. Velocity (left) and thickness (right) results

Results of Fig. 2.30 were used to obtain the variability of the measurements which is provided in Table 2.2.

Table 2.2. Variability of the measurements versus signal type

Signal	Std thickness (mm)	Std velocity (m/s)
Pulse	87.679	224.281
Chirp 30 µs	39.907	18.310
Chirp 100 µs	1.167	9.110

It can be concluded that the spectroscopy measurements' quality improvement can be achieved using SS signals. It is essential that signals overlap is the desired property here, therefore long chirp signals are advantageous.

2.8. Conclusions of the 2nd chapter

It has been demonstrated that ultrasonic signal velocity can be used in epoxy cure monitoring. It was concluded that the toneburst signal exhibited the highest abrupt errors, therefore its performance was the worst. The toneburst signal was selected under the assumption that it will be able to concentrate the majority of the excitation energy into the transducer passband, but its correlation function is not

sharp, therefore subject to abnormal ToF estimation errors. As expected, SS signals outperformed simple signals, due to their wide bandwidth and higher SNR. Narrowband chirp, matching the transducer passband, had slightly lower random errors than the wideband one due to a better bandwidth match.

Transit time ultrasonic flow measurement is using the ultrasonic signal ToF for velocity estimation. Temperature variations alter the complex transfer function of the ultrasonic transducers. This causes a bias error in the ToF estimation, resulting in a flow measurement bias error, which becomes significant at low flow velocity. It was demonstrated that the temperature effect and random errors are minimized when wideband SS signals are used. Yet, standard rectangular SS signals have a shortcoming in this application - they do not match the transducer bandwidth closely.

It has been demonstrated that the use of SS signals for excitation reduces the signal dynamic range, which in turn allows to use lower ADC resolution. In the case analyzed, pulse excitation demanded 9 bit ADC resolution, while the same results were obtained using 5 bit ADC resolution when the SS signal was used.

The electromagnetic interference caused by the thermal chamber PWM control has been studied in curding monitoring. It was established that anomalous measurement errors occur in the case of pulse excitation, while toneburst and chirp excitation provide much better results, although measurements using CW toneburst had bias errors. It was concluded that the use of SS signals for excitation results in a significant reduction of the influence of EMI.

Coin imaging using ToF has been studied when excitation amplitude was very low (5 V). It was concluded that the backwall reconstruction quality is improved in the case of SS excitation, therefore very low excitation voltage can be used. Yet, standard rectangular SS signals have a shortcoming in this application: correlation sidelobes cause ToF variation of neighboring reflections.

Thickness measurement using spectroscopy has been studied. It was concluded that a significant quality improvement can be achieved using SS signals: more than one resonant peak can be obtained (4 vs. 1 in the case of pulse and CW toneburst excitation). Yet, standard rectangular SS signals have a shortcoming in this application: transducer AC response cannot be compensated, therefore the passband frequencies have significant SNR, while out of band SNR is lower.

IC imaging using spectroscopy has been studied. It was concluded that the SS signal has better SNR and bandwidth coverage, therefore imaging can be carried out beyond the transducer passband evenly and with better energy. Frequencies of 20 MHz and 24.79 MHz can be exploited with 5 MHz transducer using +/-10 V amplitude excitation. Yet, standard rectangular SS signals have a shortcoming in this application: it is not possible to program the received signal frequency content in order to get better SNR in the band of interest.

These tasks were formulated for the next stage of research:

1. Development of a new type of the rectangular excitation signals capable to solve the shortcomings of the conventional signals. Design of the APWP optimization technique; rectify performance parameters to be used as convergence criteria; propose the candidate set generation algorithm; propose simple system transfer model for optimization.

2. Investigate the performance of APWP signals using the metrics rectified.
3. Demonstrate the APWP signals performance in imaging and measurement.

3. APWP SIGNALS DEVELOPMENT

It has already been indicated that simple signals like pulse or toneburst do not provide energy and bandwidth simultaneously, which are essential in ultrasonic imaging and measurements. Spread spectrum signals do not have this disadvantage. Several types of SS signals are in use: phase manipulated sequences [68,72,96], chirp [18] and arbitrary waveform excitation [24]. It was also demonstrated that it is advantageous to use rectangular versions of SS signals: simplicity and efficiency of excitation electronics is achieved [67]. Yet, application of rectangular signals causes additional spectral ripples and an increase of the sidelobes. On top of that, existing rectangular SS signals have the shortcomings indicated in the previous chapter.

Demand of the new SS signals with following parameters is indicated:

- simple excitation electronics (rectangular signals);
- programmable spectral shape, parameters;
- programmable correlation parameters;
- transducer and/or the system frequency response have to be accounted for during the optimization process.

Design of such signals is presented in this chapter.

3.1. APWP principle

There have been attempts to develop such signals. In [69,70,71] it was proposed to use chaotic pulse position sequences and to optimize these by randomly searching for the optimal candidate. Chaotic pulse position-width modulation was suggested in [66]: crosstalk between adjacent channels was reduced by changing the modulation sequence.

APWP principle is different: i) the construction of the excitation signal is based purely on binary, unmodulated pulses; ii) pulses can be unipolar or bipolar; iii) zeros are allowed to be introduced between the pulses, therefore changing the pulse position and width in such a way; iv) the optimization of the sequences is carried out taking into account the transmission function of the whole system (pulser, transducer, filters, amplifiers, etc.). Using this approach, the efficiency of the excitation electronics is increased. On the other hand, the complexity of the electronics and the size, cost and weight of the acquisition equipment are reduced. It is essential that APWP signals should possess the properties of SS signals: wide bandwidth and high SNR.

The novelty of the presented APWP signals is the optimization of the APWP train accounting of the signal transmission through the system. Consequently, the optimization process, correlation sidelobes, spectral shape and bandwidth of APWP signals can be programmed to adapt to system spectral distortions. No specific modulation is used: this means that the APWP sequence better fits the AC response of the system.

The generation of APWP signals depends on the topology of the excitation generator. One to two switching elements is enough to generate a positive rectangular pulse [56,61,92], in this case the generated pulses will be of single polarity (Fig. 3.1).

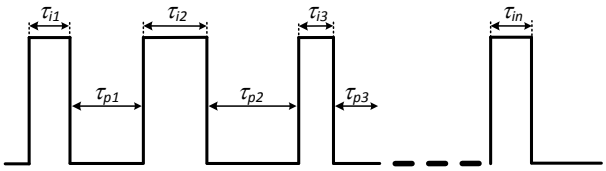

Fig. 3.1. Unipolar APWP signals

These unipolar APWP signals can be described as a sequence of interleaved pulses with duration τ_i and spacing τ_p between them:

$$s_T(t) = 1(\tau_{i1}) + 0(\tau_{p2}) + 1(\tau_{i2}) + 0(\tau_{p2}) + \ldots + 1(\tau_{in}) + 0(\tau_{pn}). \qquad (3.1)$$

Energy is increased twice using bipolar excitation [39] (Fig. 3.2).

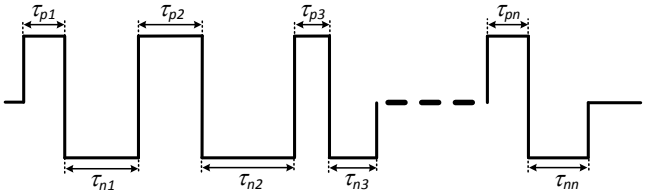

Fig. 3.2. Bipolar APWP signals

In this case, the APWP signal can be described as a sequence of interleaving high and low level pulses [67] of duration τ_p and τ_n respectively:

$$s_T(t) = 1(\tau_{p1}) - 1(\tau_{n2}) + 1(\tau_{p2}) - 1(\tau_{n2}) + \ldots + 1(\tau_{pn}) - 1(\tau_{nn}). \qquad (3.2)$$

Typical sequence presented above can be modified by adding additional spacing between pulses (Fig. 3.3) providing additional flexibility.

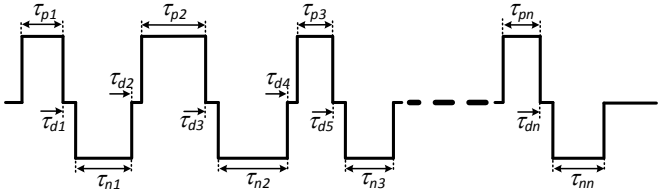

Fig. 3.3. Bipolar APWP signals with additional pauses

In this case, the APWP signal is described as interleaved high τ_p and low τ_n level pulses with short pauses τ_d between them:

$$s_T(t) = 1(\tau_{p1}) + 0(\tau_{d1}) - 1(\tau_{n1}) + 1(\tau_{p2}) + 0(\tau_{d2}) - 1(\tau_{n2}) \ldots + 1(\tau_{pn}) + 0(\tau_{dn}) - 1(\tau_{nn}). \quad (3.3)$$

Two essential tasks are envisaged for APWP signals: i) SNR and bandwidth improvement without losing correlation properties or even improving, and ii) spectral shape programmability.

Now it arises the need for an optimization method that estimates the optimum durations and positions of the pulses.

3.2. Performance parameters

Optimization requires a convergence parameter. Signal properties which have to be improved can be used. Performance parameters are analyzed in this section.

Once it is identified that the SS properties are expected from the APWP, then these signals could be compressed. It is essential to point out, that many ToF estimation or imaging applications are based on the correlation function. Normalized cross-correlation function (NCCF) was used (Fig. 3.4).

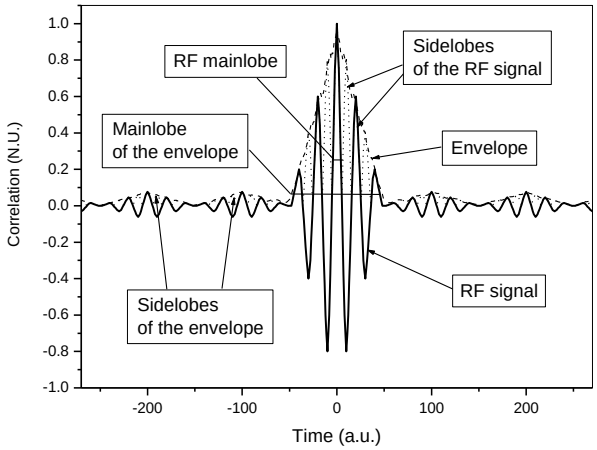

Fig. 3.4. Parameters of the signal correlation properties [34]

NCCF is obtained by dividing CCF to the geometric mean of signal st_n and the reference signal sr_n energies:

$$Cx_m = \max\left| x_m \Big/ \sqrt{\sum_{n=1}^{N} |st_n|^2 \sum_{n=1}^{N} |sr_n|^2} \right|, \tag{3.4}$$

where N is the signal length.

SS compression quality can be evaluated by the parameters presented below.

The mainlobe width of the RF signals NCCF, τ_{RF} (Fig. 3.4) represents the imaging resolution [3,82]. In discrete terms, the mainlobe width $n\tau_{RF}$ is obtained as:

$$n\tau_{RF} = \arg\left(Cx_m = 0.5\big|_{m>m_{peak}} \right) - \arg\left(Cx_m = 0.5\big|_{m<m_{peak}} \right), \tag{3.5}$$

where m_{peak} is the position of the correlation peak.

The ratio of the RF sidelobes peak to the mainlobe peak level (denoted by SLL_{RF}) can be used to express the imaging contrast capability [1,2] if the RF signal is used for imaging:

$$SLL_{RF} = 20\lg \frac{\max\left[x_m\right]\big|_{m\neq\pm 0.5n\tau_{RF}}}{\max\left[x_m\right]\big|_{m=\pm 0.5n\tau_{RF}}}, \tag{3.6}$$

where $n\tau_{RF}$ is the RF correlation function mainlobe width.

The ratio of the envelope sidelobes to the mainlobe can be used to evaluate the conventional imaging contrast capability. The ratio of the RF sidelobes energy to the mainlobe energy (denoted by SLE_{RF}) can be used to evaluate the conventional imaging contrast capability [31]:

$$SLE_{RF} = 20\lg \frac{\sum_{m=+0.5n\tau_{RF}}^{N} \left(x_m\right)^2 + \sum_{m=-N}^{-0.5n\tau_{RF}} \left(x_m\right)^2}{\sum_{m=-0.5n\tau_{RF}}^{+0.5n\tau_{RF}} \left(x_m\right)^2}. \tag{3.7}$$

If NCCF is demodulated by taking the envelope (Fig. 3.4), then the mainlobe width of the NCCF envelope has to replace the metrics of the imaging resolution [31]. The envelope of the CCF is obtained by its Hilbert transform:

$$xe_m = \left|\mathrm{Hilb}\left(x_m\right)\right| = \left|\mathrm{IDFT}\left\{\mathrm{DFT}(x_m) \times 2\,\mathrm{H}(f_n)\right\}\right|. \tag{3.8}$$

where $H(f_n)$ is the Heaviside function.

Then NCCF C_{xm} in (3.5)-(3.7) is replaced by xe_m. Sidelobe to mainlobe ratio of the NCCF envelope represent the attainable contrast in imaging.

If the NCCF envelope is used in ToF estimation then Cramer-Rao lower error bound [46,47], equation (1.8) should be modified as:

$$\sigma_{ToFenv} \geq \frac{1}{2\pi\beta\sqrt{\frac{2E}{N_0}}}. \tag{3.9}$$

In which case, only the envelope bandwidth β, not F_e, defines ToF errors. Envelope bandwidth β can be used as performance parameter then.

CRLB is accounting only for the SNR at the main correlation lobe. If a narrowband signal is used (either because the transducer or the excitation signal are narrowband), RF correlation sidelobes are high (Fig. 1.2). Therefore, if the SNR is not sufficiently high (compare actual peak position and estimated peak position in (Fig. 1.2), abrupt ToF estimation errors will occur. CRLB and SLL can be combined to evaluate the correlation properties performance in such a case. One more performance parameter, relative noise margin (RNM), is defined and that accounts for the peak amplitude (*Pk* in Fig. 1.2), sidelobe amplitude (*SL* in Fig. 1.2) and SNR [25]:

$$RNM = \frac{Pk - SL}{SNR}. \tag{3.10}$$

The RNM parameter is important only in the case of narrowband transducers.

Some applications require specific signal properties, which may depend on the signal processing technique used for further analysis, such as split spectrum [81] or spectroscopy [64]. Few main spectral properties can be distinguished: maximum bandwidth at (-3 dB or -10 dB), spectral flatness in the main transmission bandwidth and how good the signal spectrum fit is to the desired spectral response (Fig. 3.5). The

desired spectral response is needed if spectral losses compensation is supposed to be used [90].

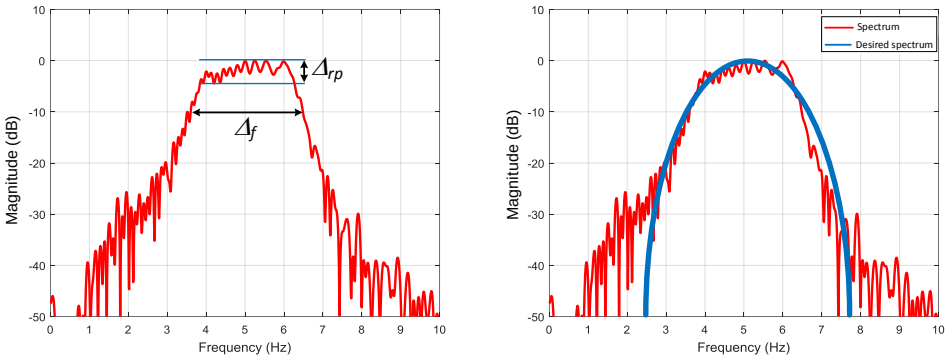

Fig. 3.5. Spectral quality evaluation parameters: bandwidth and spectral ripple (left) and goodness of fit to desired response (right)

Performance parameters were used in the optimization presented below.

3.3. Optimization of APWP signal

The main difference between APWP sequences and conventional signals is that APWP does not rely on any predefined modulation, this means that there is a higher degree of freedom for pulse duration and position in a sequence. A high degree of freedom and absence of mathematical methods for such sequences derivation requires full permutation of all possible pulse combinations. As a result of full permutation, APWP may turn to a rectangular version of chirp, PSK or toneburst signals.

The optimization algorithm structure is presented in Fig. 3.6. The convergence criteria for the optimization has to be based on the aimed signal application: if it is used in ToF estimation, then it has to gain the bandwidth, while correlation sidelobes and mainlobe width are essential in imaging. Then the optimization process has to find the APWP signal that offers the best performance parameter that has been selected.

Optimization starts with the constraints definition according to the application and equipment. In general, the maximum APWP sequence duration and pulses durations range must be defined. The maximum APWP sequence duration is limited by the dead zone length [99,100] or the interfering reflections temporal spacing. In further experiments these were selected in a range of 5 to 50 periods of the transducer center frequency. For the most frequently used 5 MHz transducer, this would correspond to 1 μs to 10 μs sequence length. The pulse durations range selection can be based on the bandwidth of the transducer used or on the desired signal bandwidth: minimal duration was half of the period of the highest frequency and maximal duration was set as half of the period of the lowest frequency. Therefore, the durations range has to be rounded to the sequence sampling period. For a 5 MHz, 80 % -6 dB bandwidth transducer and a 100 MHz sequence sampling frequency, as this would correspond to a range for the pulse durations of 70 ns to 170 ns or 7 to 17 clock ticks.

The essential disadvantage of APWP signals is that they must be optimized, direct derivation is not possible. Optimization involves testing of the candidate signals on a real acquisition system, because the response of the whole system has to be involved.

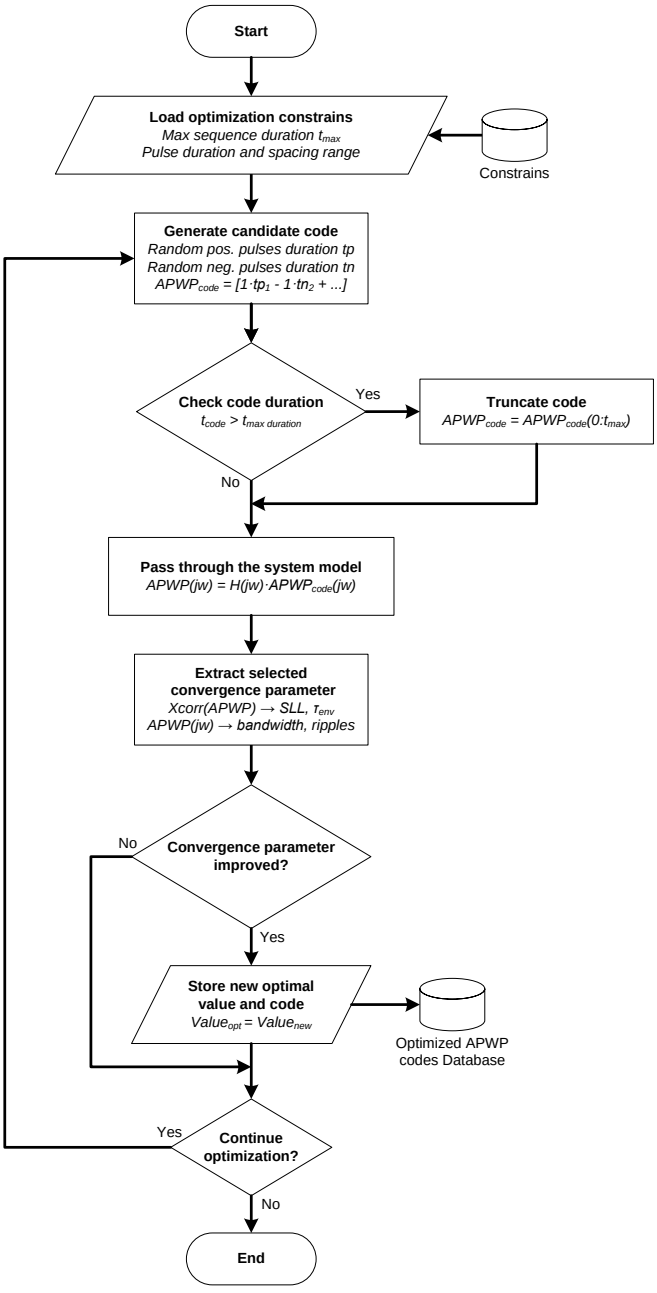

Fig. 3.6. The structure of the APWP signal optimization algorithm

The number of possible combinations is large. Note; assuming that the pulse can take three levels (1, 0 and -1) in a sequence, the range of durations used is N_{dur} and the number of pulses in sequence is N_{pulses}, the total number of combinations:

$$N_{tot} = \left(N_{dur} \right)^{N_{pulses}} . \tag{3.11}$$

As an example, with N_{dur}=10 and N_{pulses}=10, N_{tot} is 10^{10}. With one candidate signal processing time of 1 ms, full permutation would take four months. It was proposed to replace the real system experiment by a system transmission model in order to speed up the optimization iterations. Instead of doing the optimization iterations in a real environment, these can be accomplished mathematically. The model has to be simple to save optimization time.

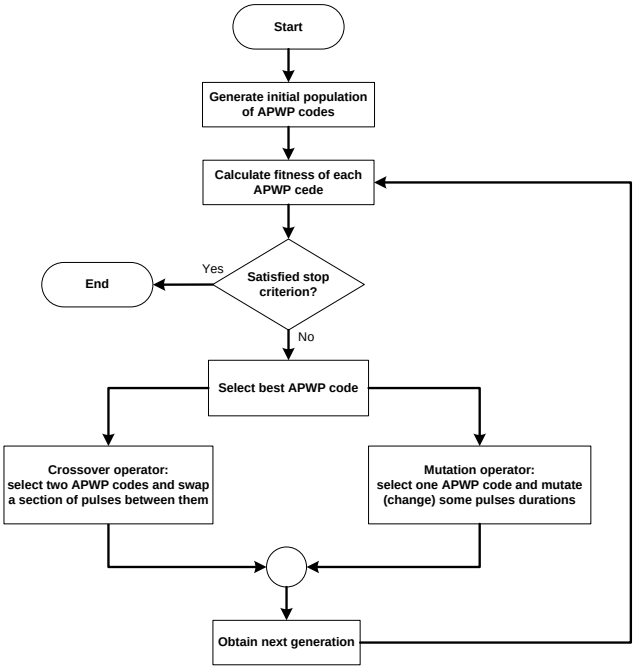

Fig. 3.7. General structure of genetic algorithm for APWP signal derivation

Furthermore, the actual number of permutations is higher if the total duration of the sequence is fixed, as the total number of pulses in a sequence increases significantly in the case of shorter pulses. Therefore, the Monte-Carlo technique was used, and instead of full permutation of all possible pulse combinations, random pulse durations and positions were exercised at each iteration. Uniform distribution of random numbers in the candidate code generation was used in order to cover the whole range evenly. Yet, the Monte-Carlo technique possess certain disadvantages: i) it does not take into account the convergence parameter; ii) external stop criteria (number of iterations) has to be used; iii) same code can be exercised several times. For these reasons, a genetic algorithm (Fig. 3.7) was used as an alternative to Monte-Carlo.

After generating the candidate APWP signal, it is passed through the system model and the simulated output is treated as a signal obtained with the real system.

Then, this signal is used to extract the desired optimization parameters (e.g. cross-correlation function or spectral properties) discussed in chapter 1.5. These parameters are compared to previous results and, if they are better, then the candidate signal together with the extracted parameter are stored in the optimization data base.

The next sections are devoted to show the performance of different models used in the optimization process.

3.3.1. Spectral model

The received echo signal s_R can be treated as carrying the information about the whole system (pulser, ultrasonic transducer and acquisition system) transmission properties:

$$S_R(\omega) = S_T(\omega) \cdot T_P(\omega) \cdot T_X(\omega) \cdot T_{ACQ}(\omega) + n(\omega), \tag{3.12}$$

where $T_P(t)$ is the transmission AC response of the pulser, $T_X(t)$ is the combined transmission AC response of the transducer in transmission, water path, reflection from interface and transducer in reception, $T_{ACQ}(t)$ is the transmission AC response of the whole acquisition system, including cables, preamplifier, filters and ADC response and $n(t)$ is a non-correlated additive white Gaussian noise. Then, using the excitation signal $S_T(\omega)$ (obtained as the Fourier transform of the mathematical representation of the signal loaded into the pulser memory) and the received echo signal $S_R(\omega)$ (obtained as the Fourier transform of the signal recorded in the acquisition system memory), the transmission AC response T_{sys} of the whole system can be obtained as:

$$T_{sys}(\omega) = \frac{S_R(\omega)}{S_T(\omega)}. \tag{3.13}$$

Experimental setup for the spectral model derivation is presented in Fig. 3.8.

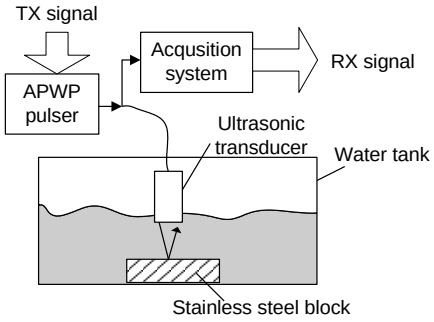

Fig. 3.8. System AC response measurement setup

A solid stainless steel block was placed into the water tank and reflections of ultrasonic signals from the block were collected. Wideband (86 %) composite (48 dB sensitivity) ultrasonic transducer TF5C6N (supplied by Doppler Ltd.) with center frequency 4.61 MHz was used in pulse-echo mode for experimental evaluation of such system model performance.

Pulse signal can be used for the model derivation, but spectral zeroes are present in pulse spectrum. Several pulses of duration 10 ns to 200 ns were used in order to reduce the noise influence and eliminate the spectral zeroes effect. Signals obtained were transformed to the frequency domain (refer to Fig. 3.9) and averaged.

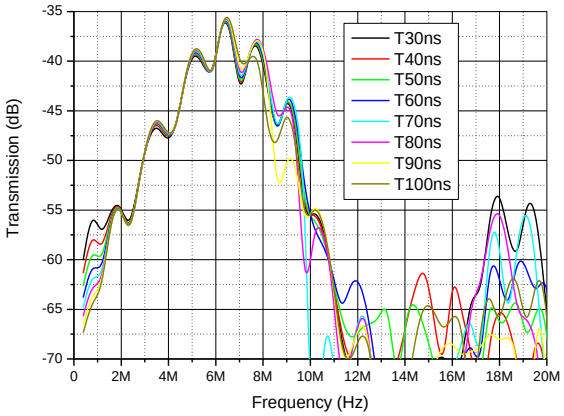

Fig. 3.9. System AC response when measured with square pulse

Chirp signals were also used because they do not have spectral dips. Two types of chirp signals were used: 0.1 MHz to 20 MHz and 1 MHz to 15 MHz. With these signals, the resulting system transmission AC response is presented in Fig. 3.10.

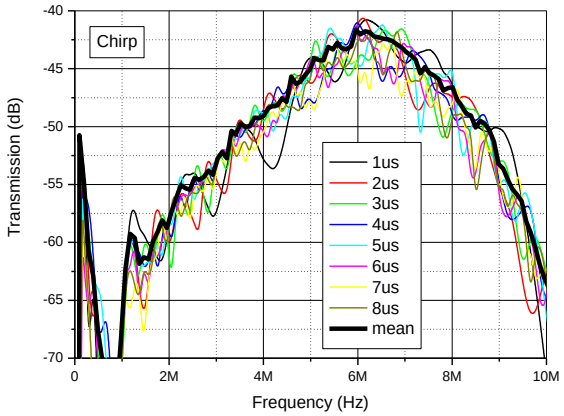

Fig. 3.10. System AC response when measured with chirp and mean value of all measurement (solid line)

All system transmission AC responses were combined to produce a single AC response (solid line in Fig. 3.10). This mean AC response T_{sys} was used to simulate the received signal $S_{Rnew}(\omega)$ for any candidate signal $S_{Tnew}(\omega)$:

$$S_{Rnew}(\omega) = S_{Tnew}(\omega) \cdot T_{sys}(\omega). \tag{3.14}$$

Signal $S_{Rnew}(\omega)$ was converted into time domain signal $s_R(t)$ using the inverse Fourier transform.

3.3.2. Convolutional model

The convolutional model (see explanatory diagrams in Fig. 3.11) was proposed as an alternative to the spectral model.

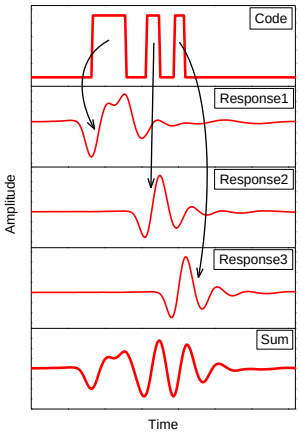

Fig. 3.11. Explanation of the convolutional model operation

This type of model is free from the spectral zeroes problem, which is present in the spectral model. The signals recorded at the receiving ultrasonic transducer in the experiment presented in Fig. 3.8 can be used to construct the response of the candidate APWP. The APWP signal is first submitted to duration analysis to extract the duration of the current APWP pulse. Once the required pulse durations is established, then the corresponding temporal response of the previously recorded pulse is added to generate the APWP signal response.

3.3.3. Models comparison

The convolutional model was compared against the spectral model using real signals recorded using several APWP codes. Fig. 3.12 shows the results of the correlation coefficient (3.4) between the simulated and the measured signals.

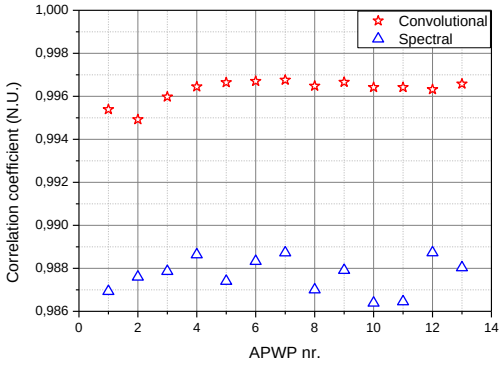

Fig. 3.12. Correlation coefficient between simulated and measured signals

It can be seen that the convolutional model is producing a closer correlation to the real signal than the spectral model. The lowest correlation coefficients are 0.995

and 0.986 for the convolutional and the spectral model respectively. The highest coefficients are 0.997 (convolutional) and 0.989 (spectral). Even the spread of the coefficients for the convolutional model is half as low.

The same signals were compared by mainlobe width. In this case, the difference between the correlation mainlobes obtained for the simulated and the measured in the real environment was obtained and threated as error (Fig. 3.13).

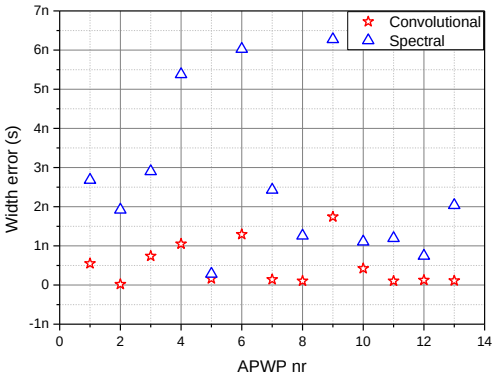

Fig. 3.13. Mainlobe width error of simulated signals for APWP codes

The maximum deviation of the mainlobe width for the convolutional model is 1.8 ns, and 6.3 ns for the spectral model. The mean error is low for the convolutional model but reaches 3 ns for the spectral model. The standard deviation of the mainlobe width reconstruction was small, yet significantly higher for the spectral model (1.2 ns versus 0.3 ns for the convolutional). It can be concluded that the convolutional model provides a better reconstruction of the correlation mainlobe duration.

The performance of the proposed models was also compared in terms of the correlation sidelobes level. Simulated sidelobe level deviation from real signals are presented in Fig. 3.14.

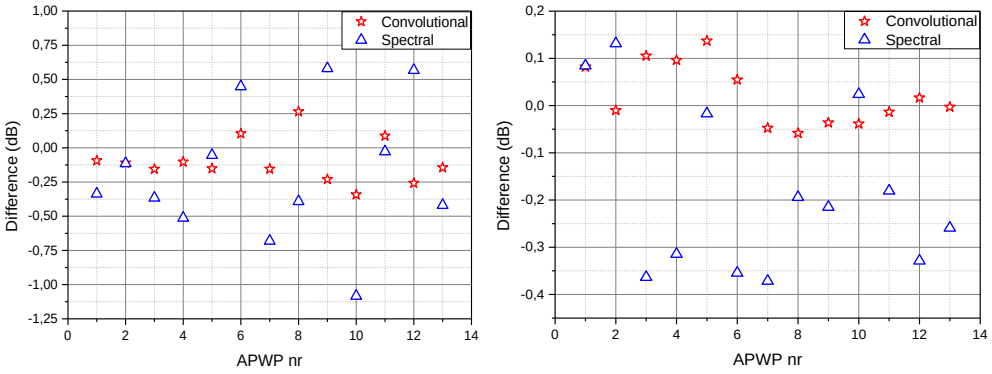

Fig. 3.14. Correlation sidelobe level (left) and sidelobe energy (right) difference

It can be concluded that both models have similar performance when the correlation sidelobe level and correlation sidelobe energy are compared. The performance of the convolutional model is only slightly better (0.3 dB peak error

against 0.6 dB for spectral model). Notable that, convolutional model is slower than the spectral one. In the case of 1024 signal samples and 30 pulses in APWP, the convolutional model requires 1024 comparison operations, 1024 shift and sum operations which are repeated 30 times, therefore 92160 in total. Conversely, the spectral model requires 21504 (1024x10x2+1024) operations in total, which is 4.2 times faster.

The analysis presented above revealed that both models are adequate in system simulation. The spectral model has lower performance compared to the convolutional one. In order to establish the source of this difference in the performance, the same system was used to acquire real signals at the pulser output (Fig. 3.15), and the obtained real signal was then compared against its simulated counterpart.

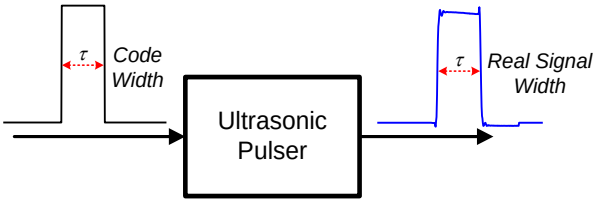

Fig. 3.15. Experimental setup for model adequacy investigation

The ultrasonic pulser was driven by different duration pulses. It was assumed that the reason for the model mismatch lies in the signal duration. To verify this assumption, the duration of the code τ_{code} was compared against the duration τ_{real} at the output:

$$\varepsilon(\tau_i) = \tau_{code} - \tau_{real}. \tag{3.15}$$

Results are presented in Fig. 3.16.

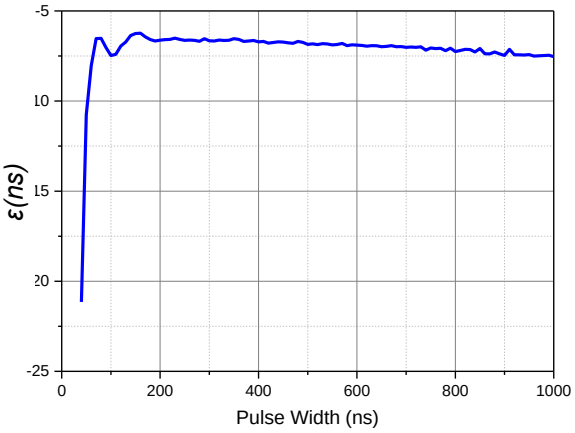

Fig. 3.16. Deviation of the pulse duration at pulser output from the set value

It can be seen that there is a significant pulse duration error in the pulser output. Systems using conventional probing signals are not affected by this problem, but for APWP correspondence between coded and actual pulse duration it is very important.

3.4. Conclusions of the 3nd chapter

A new APWP type of rectangular excitation signals was proposed:

i) excitation signal is based purely on binary, unmodulated pulses;
ii) pulses can be unipolar or bipolar;
iii) zeros can be inserted between pulses to change pulse position and width;
iv) the optimization of the sequences accounts for the transmission of the whole system (pulser, transducer, filters, amplifiers etc.).
v) excitation electronics efficiency is high, complexity of the electronics, size, cost and weight of the acquisition equipment reduced;
vi) signals have SS properties: wide bandwidth and high SNR;
vii) due to the optimization process, correlation sidelobes, spectral shape and bandwidth of APWP signals are programmable.

Performance parameters have been proposed:

- correlation properties: RF mainlobe width, envelope mainlobe width, RF sidelobes peak to the mainlobe peak ratio, sidelobes energy to the mainlobe energy ratio, envelope sidelobes to the mainlobe ratio and relative noise margin;
- spectral properties: effective bandwidth, envelope bandwidth, maximum bandwidth, spectral flatness and good signal spectrum fit to desired spectral response.

An optimization procedure has been designed. The procedure involves a numerical model of system transmission. Two models have been proposed and compared: spectral and convolutional. Good correlation agreement with real signals was found: highest coefficients are for convolutional (0.997 vs. 0.989 for spectral). Pulse duration error is low for the convolutional model but reaches 3 ns for the spectral model. It was concluded that the convolutional model provides a better reconstruction but is slower than the spectral one (4.2 times slower in the case of 1024 samples and 30 pulses).

4. APWP SIGNALS PERFORMANCE STUDY

APWP signals are expected to offer programmable correlation sidelobes and the ability to concentrate the excitation energy into the passband. The investigation below was to analyze to what extent these signals can be optimized.

4.1. Correlation properties

APWP signals optimization according to correlation properties is presented below. Optimized correlation properties were: maximum value of all the sidelobes beyond the first zero crossing, the energy of the sidelobes and the mainlobe duration.

A spectral transmission model [3] was used to optimize the transmitted signal as if it was used in a real-world experiment. Monte Carlo technique (10 000 iterations) was used to the APWP pulses and pauses durations. Results for mainlobe duration minimization are presented in Fig. 4.1.

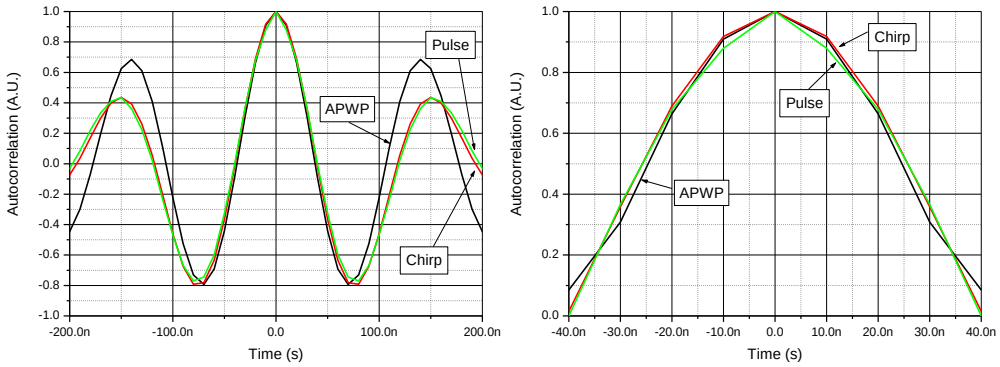

Fig. 4.1. Correlation mainlobe (RF-left, envelope-right) for pulse, chirp and APWP signals

It was expected that the pulse signal possess the lowest sidelobes, but it can be seen that the optimized APWP has similar properties to pulse performance. Results when the APWP signal was optimized for peak sidelobes level reduction are presented in Fig. 4.2.

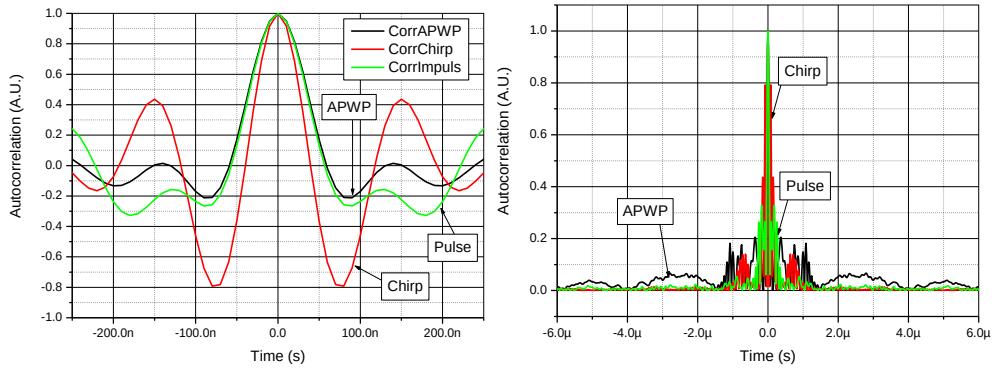

Fig. 4.2. Sidelobes' optimization: RF (left) and envelope (right) correlation function

Results when the APWP signal was optimized for sidelobes' energy minimization are presented in Fig. 4.3.

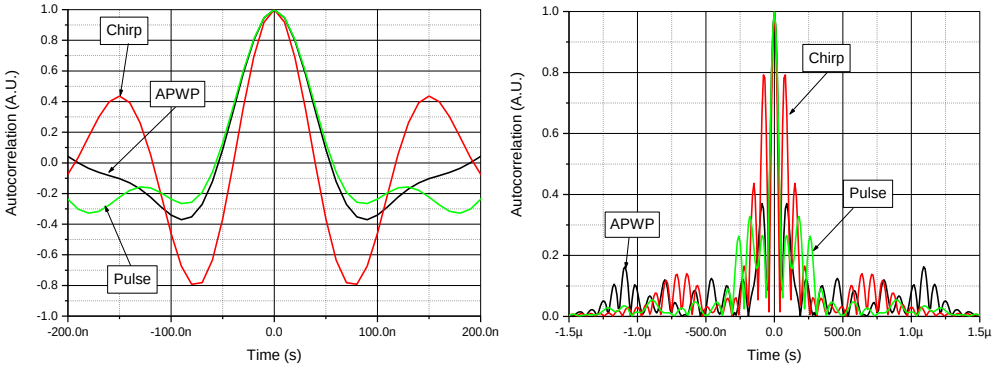

Fig. 4.3. Sidelobes' energy minimization result: RF correlation function (left) and correlation envelope (right)

It can be noted that APWP performance is better or similar to the classical chirp and pulse signals: in some cases, APWP performance was the best (mainlobe duration (Fig. 4.1) and sidelobes' energy (Fig. 4.3)). Initial investigation indicates that APWP signals can have properties similar to those of chirp and pulse signals.

The generated code (Fig. 4.4 left) was uploaded to the pulser memory of the ultrasonic system and then transmitted. The same transducer was used to transmit the signal into water. A stainless steel reflector was placed in the water and the received reflection recorded (Fig. 4.4 center). A spherically focused 60 % bandwidth 5 MHz center frequency ultrasonic transducer IRY405 (from NDT transducers LLC) was chosen for this analysis. The excitation was performed using a unipolar pulser. APWP signals optimization time diagrams are presented in Fig. 4.4.

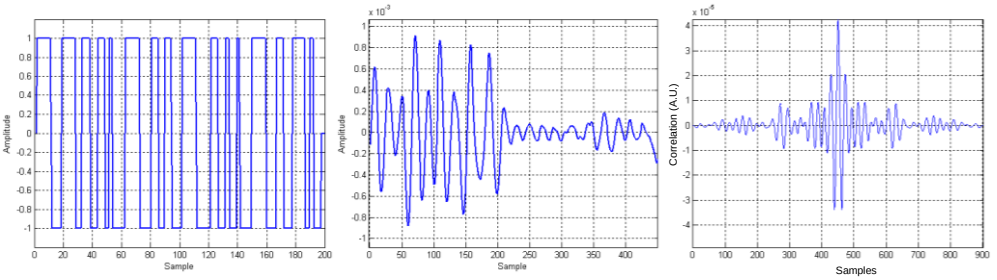

Fig. 4.4. APWP signals exploration stages: uploaded code (left), received signal (center) and autocorrelation function of the signal (right)

Signal was submitted for correlation processing and the sidelobe level evaluated. Codes were generated using Monte Carlo technique: randomly chosen combinations were evaluated but only the code with the lowest sidelobes were kept.

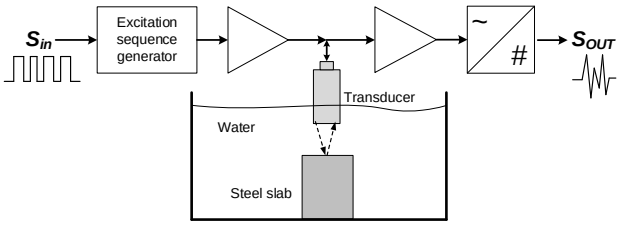

Fig. 4.5. System structure used for APWP signals investigation

Example of time diagrams and sidelobes level change over iteration steps is presented in Fig. 4.6. Left graph shows the correlation before optimization, and center graph is representing final optimization result.

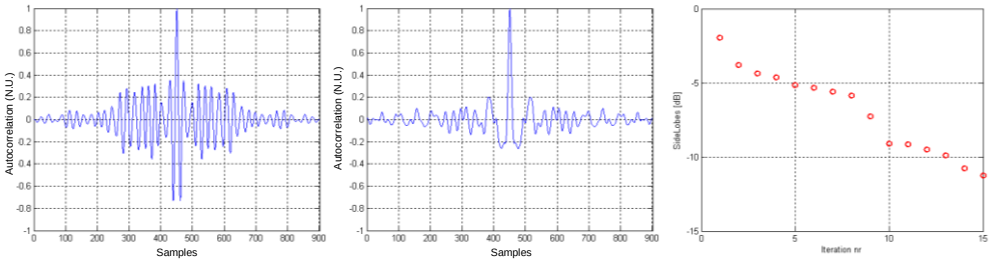

Fig. 4.6. APWP optimization using Monte Carlo: initial correlation function (left), correlation function at step 15 (center) and sidelobes level variation over iterations (right)

As a result of the ability to generate multiple APWP pulse trains, several signals can be simultaneously evaluated. It can be seen that the sidelobes were reduced by 11 dB.

4.2. Temporal resolution

Resolution of ultrasonic imaging demands wideband signals for excitation. If reduction of the RF sidelobes is required, this is equivalent to reducing the mainlobe width of the envelope. This in turn is equivalent to increasing the signal bandwidth. However, the ultrasonic transducer is limiting the bandwidth of the signal. Bandwidth compensation can be done by post processing but then SNR over the bandwidth is not ensured. A better approach would be to alter the frequency content of the probing signal so that more energy is placed at the components that will be attenuated. The optimization of the signals in the investigation presented below was carried out to achieve the lowest RF correlation sidelobes. An experimental comparison of APWP signals with conventional signals was done using the same system setup as above. The aim of this analysis was to decide which signal types are suited for signal optimization to achieve the lowest RF correlation sidelobes.

All signals considered were using unipolar rectangular pulses with amplitude 15 V. All spread spectrum signals were of 3 μs in duration in order to equalize the amount of initial energy. Three types of rectangular pulse signal were chosen: i) 50 ns duration (representing spike excitation); ii) 120 ns duration (representing best excitation) and iii) 220 ns duration (best RF sidelobe to mainlobe level ratio). In essence, the desired signal should provide a spectral dip at the transducer center

frequency, increasing the resulting signal bandwidth [49], therefore type iii pulse corresponds to such a case. Two types of CW toneburst signals were used: i) 4.5 MHz (representing best excitation) and ii) 7.45 MHz (representing lowest sidelobes and shortest RF mainlobe). Three types of chirp signal were selected: i) linear 3 μs duration chirp 1 MHz to 10 MHz (representing classical chirp where spectral shaping occurs naturally due to the transducer frequency response); ii) linear 3 μs duration chirp 1 MHz to 5 MHz (best RF sidelobe to mainlobe level ratio) and iii) nonlinear 3 μs duration chirp generated using adaptive 4-th order polynomial for instantaneous frequency generation (best RF sidelobe to mainlobe level ratio). RF sidelobe to mainlobe level ratio optimized APWP signal with 3 μs duration was selected as the representative of the type where there is most flexibility in the signal shape. Last type selected was a 13 elements Barker code, as a representative of spread spectrum signals where control of the spectral shape is not possible. The main signal parameters are presented in Table 4.1.

Table 4.1. Parameters and properties of the excitation signals used in investigation

Label	**Signal type**	SLL_{RF} **dB**	SLL_{Henv} **dB**	τ_{RF} **ns**	E_i **dB**	F_e **MHz**	β **MHz**
P50	Pulse 50 ns	-3.1	-22	73	0	4.9	2.0
P120	Pulse 120 ns	-3.3	-22	85	6	4.2	1.7
P220	Pulse 220 ns	-7.6	-22	108	4	3.7	2.3
CW5	Toneburst 4.5 MHz 3 μs	-0.3	-31	74	19	4.6	0.8
CW7	Toneburst 7.45 MHz 3 μs	-3.6	-7.1	53	7	7.1	4.0
Ch10	Linear chirp (1-10) MHz 3 μs	-3.7	-13.7	74	14	4.9	2.2
Ch5	Linear chirp (1-5) MHz 3 μs	-2.6	-14.9	87	16	4.1	1.6
NLch	Nonlinear chirp 3 μs	-13.1	-11.3	106	10	3.9	2.6
APWP	APWP 3 μs	-15.1	-10.7	103	10	4.0	2.7
B13	Barker13 (chip 1 period)	-2.5	-18.0	78	16	4.5	1.7

The obtained signals were compared by the level of the correlation RF sidelobes, correlation envelope sidelobes, mainlobe duration, energy, effective bandwidth and envelope bandwidth. Comparison results are presented in Fig. 4.7 and Fig. 4.8.

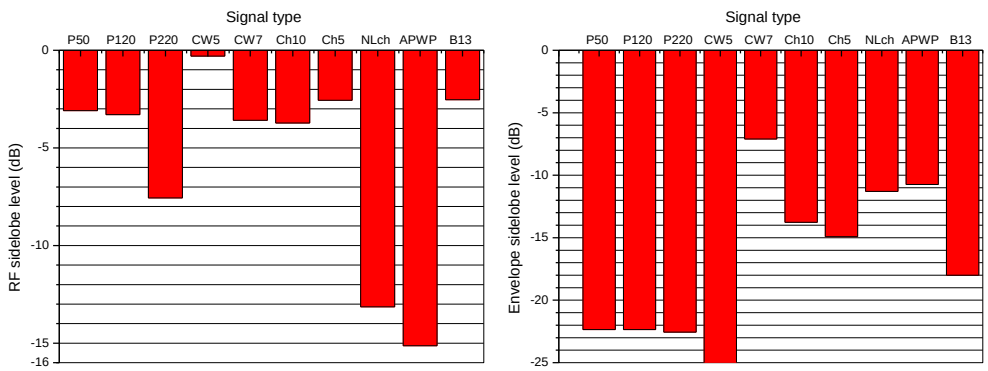

Fig. 4.7. Correlation sidelobes level peak vs. signal type: RF (left) and envelope (right)

It can be concluded that APWP and nonlinear chirp signals have the lowest RF correlation sidelobes level in exchange of significant loss of energy. When it comes

to the envelope sidelobes, pulse and toneburst signals, these indicate the best results which is misleading, because these signals are not compressible, therefore envelope sidelobes do not exist. Barker code has the lowest envelope sidelobes, but -18 dB instead of the expected -22.3 dB. Envelope sidelobes are 8 dB worse for APWP and nonlinear chirp, but these signals were not optimized for the envelope sidelobes.

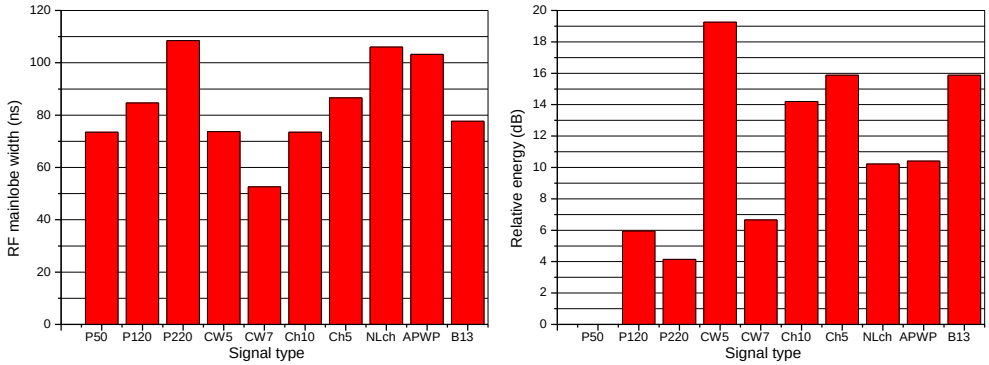

Fig. 4.8. Signal RF correlation mainlobe width (left) and relative energy (right) vs. signal type

As expected, the narrowest RF mainlobe was for the 7.45 MHz toneburst signal: despite being away from the center frequency, it has enough energy to produce the narrowest mainlobe, but it has a very high sidelobe level and low energy, almost the same as the pulse.

With the set of optimized signals available, experiments have been carried out. Emulated situation (Fig. 4.9) was representing a small defect present close to the backwall of the test sample. The defect was emulated by the 0.34 mm diameter fishing line placed above a thick Plexiglas slab. This experiment presented below was aimed to evaluate the random errors of the reflection temporal position estimation.

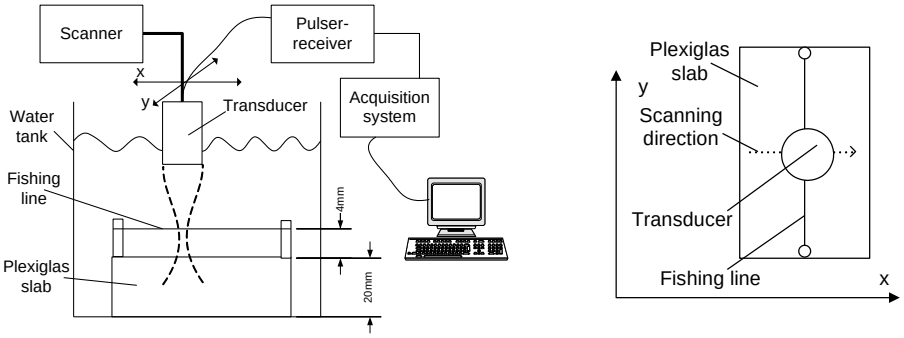

Fig. 4.9. Experimental setup (left): for ToF and spatial position estimation errors study (right)

The same spherically focused 5 MHz ultrasonic transducer IRY405 (from NDT transducers LLC) was used. The excitation was performed using the same unipolar pulser with 15 V excitation signal amplitude and 12 dB gain of the preamplifier. The

signal was always acquired with a large refection from the Plexiglas present, so gain and the excitation amplitude were adjusted according to this signal. Therefore, the signal from the fishing line was considerably smaller.

The fishing line was placed at 4 mm from the Plexiglas slab (Fig. 4.9 left), and the transducer was precisely positioned above the fishing line at a focal distance (37 mm). A-scan signals were acquired 1000 times in the same position, then aligned and averaged to produce the reference signal, which was later used for ToF estimation. Temperature of the bath was not controlled, therefore temperature variation induced a trend in the measurements. A moving average filter of 20 samples was used to smooth the data. After removing the trend from the ToF array, the standard deviation of the ToF was calculated. Comparison of random errors for the ToF estimation (when RF and envelope of the correlation are used) are summarized in Fig. 4.10. It can be seen that the lowest random errors are in the case of RF information exploitation. On the other hand, the best performance was for CW toneburst with the frequency matching to the transducer response. Errors for spread spectrum signals are low for both in the case of RF and envelope information, due to high energy. Additionally, signal to clutter ratio (SCR) was calculated using peak values (Fig. 4.10 right).

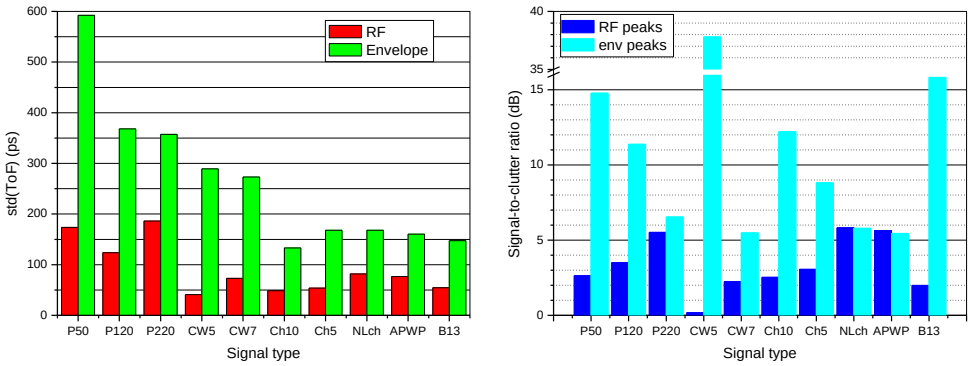

Fig. 4.10. Random errors of ToF estimation (left) and signal to clutter ratio in time domain (right)

In the case of envelope, SCR was highest for CW toneburst with the frequency matching to the transducer response, but this conclusion is misleading since the mainlobe of the correlation envelope for this signal is very wide. Barker code and short pulse have the best performance here. The best performance for the RF case was for nonlinear chirp and APWP signal.

4.3. Spatial resolution

The analysis of the influence of the signal type on the spatial resolution has been carried out using two 0.4 mm diameter copper wires, which had a spacing of 5mm at one end and where together at the opposite end at 135mm distance (Fig. 4.11).

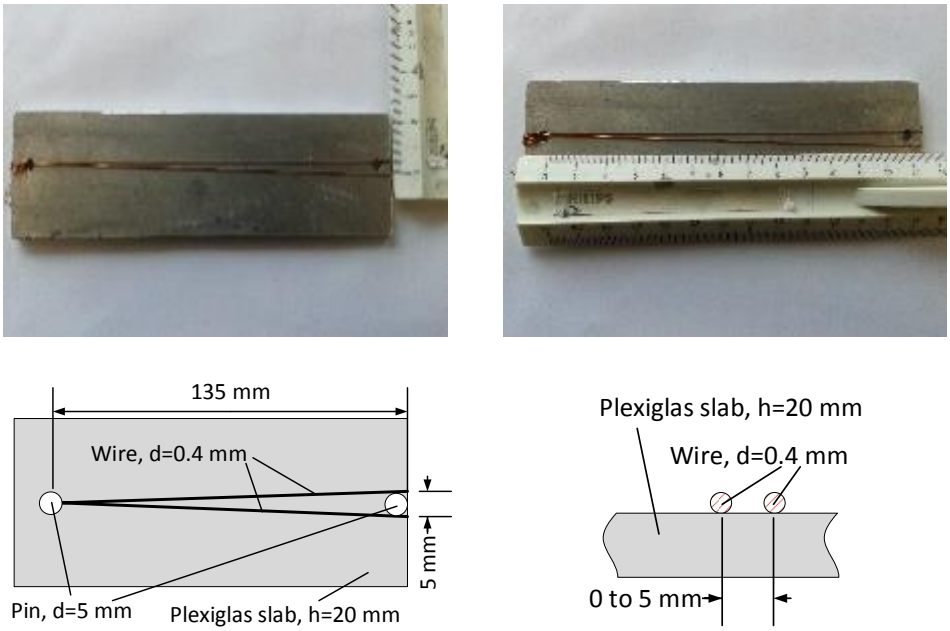

Fig. 4.11. Setup for spatial resolution study: photos (top) and drawing (bottom)

This investigation takes into account that the transducer lateral resolution depends on the wavelength to transducer diameter ratio. Refer to Fig. 4.12 for 5 MHz IRY405 transducer beamwidth versus frequency plot at -6 dB (outer lines) and -3 dB (inner lines).

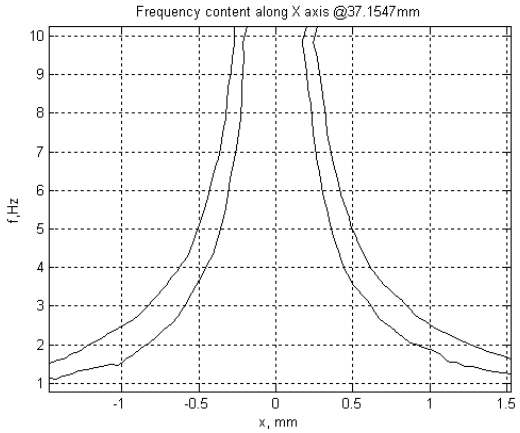

Fig. 4.12. Transducer IRY405 beamwidth variation with frequency

It should be noted that the pulse and PSK signals concentrate their energy around the center frequency, so little energy remains at high frequencies. Therefore, lateral resolution for these signals is defined by the center frequency. Meanwhile, SS signals can concentrate energy into higher frequencies and provide better lateral resolution.

The same acquisition system as above was used, same 5 MHz IRY405 transducer and pulser SE-TX-06-00 with 2 V and 20 V excitation amplitude, reception gain was 37.16 dB and 4.5 dB correspondingly. The scanning area was 400x60 with 250 µm step size. Twelve signals were used in the evaluation, whose parameters are resumed in Table 4.2.

Table 4.2. Excitation signals used

Nr.	Signal type	Parameters	Note
Gencode1	Pulse	4 samples	Wide bandwidth
Gencode2	Pulse	8 samples	Best energy-and bandwidth ratio
Gencode3	Pulse	10 samples	For high signal energy
Gencode4	Barker code	Scale 4	
Gencode5	Barker code	Scale 8	
Gencode6	Barker code	Scale 10	
Gencode7	CW burst	5 MHz @ 1 µs	
Gencode8	CW burst	7 MHz @ 1 µs	
Gencode9	Chirp	1-10 MHz @ 1 µs	
Gencode10	Chirp	2-7 MHz @ 1 µs	
Gencode11	APWP	3 µs duration	Optimize for low sidelobes
Gencode12	APWP	3 µs duration	Optimize for low sidelobes

Signals reflected from the wire were gated out and a C-scan image was produced. Refer to Fig. 4.13 for example of C-scan image and signal intensity variation across the wires.

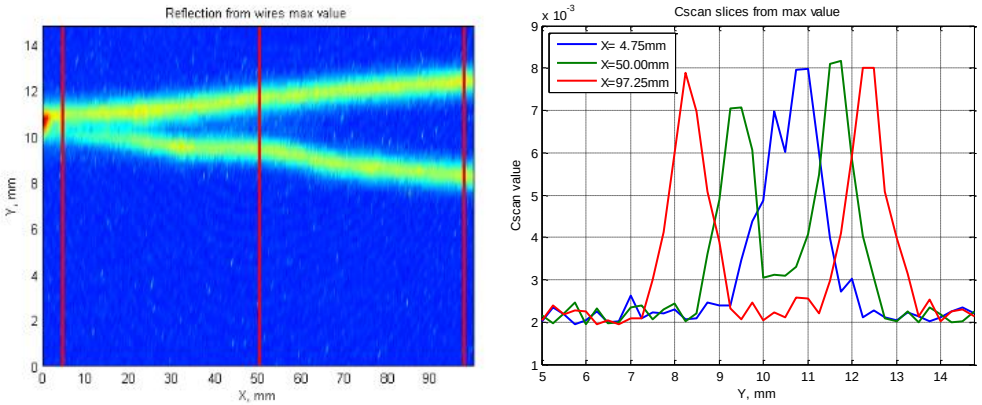

Fig. 4.13. C-scan image (left) and signal intensity variation across the wires (right)

Resolution performance was evaluated by trying to find the spacing between the wires. The signature of the wire was taken at the widest spacing (right line in Fig. 4.13). This signature was spatially correlated with the rest of the image. The correlation peak position was estimated using correlation peaks position (equations (2.2), (3.2)-(3.6)). Resulting wires spacing and C-scan images used for processing are presented in APPENDIX A. It can be concluded that APWP and chirp provided best spatial resolution (lowest deviation from actual wires spacing).

4.4. Spatial position estimation random errors

This experiment was aimed to evaluate the random errors of the defect spatial position estimation. A fishing line was placed at 4 mm from the Plexiglas slab (Fig. 4.9 right), and one line along coordinate *x* was scanned across the fishing line using 10 nm step. One hundred A-scans were acquired at every scanner position. This data was later split to emulate the situation where the same scan along *x* axis was carried out 100 times. This one hundred scanner positions were used to locate the position x_{peaki} where the signal reflected from the fishing line has maximum value, assuming it as a defect spatial position. Results are summarized in Fig. 4.14 left. Same signals were used, main signal parameters are presented in Table 4.1.

Both raw data and the cross-correlation results were used for maximum location. Obtained data positions x_{peaki} were processed to obtain the random errors (standard deviation) of this position estimation.

It can be seen that the lowest random errors are for CW toneburst of the frequency matched to the transducer center frequency. Random errors are small for spread spectrum signals as well. The same data was averaged and later used to produce the transducer directivity presented as the point spread function (PSF) at -6 dB level. Comparison of the PSF width for all signal types is presented in Fig. 4.14 right.

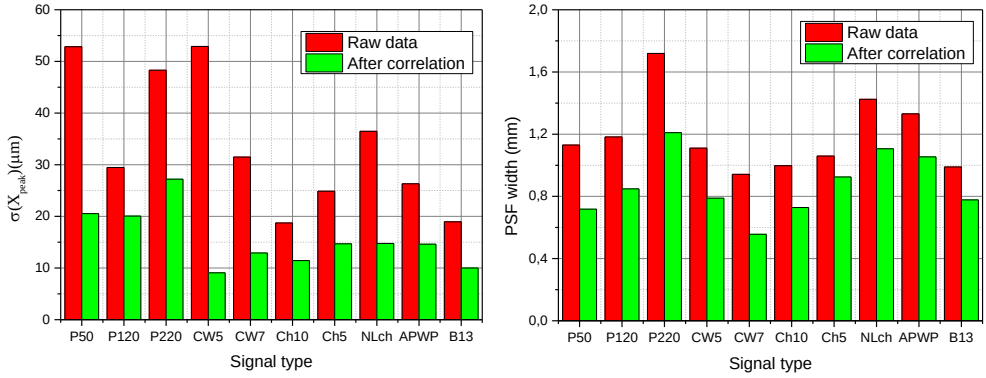

Fig. 4.14. Random errors of spatial position estimation (left) and PSF width @-6 dB (right)

It can be seen that the narrowest PSF is for the 7.45 MHz CW toneburst signal: it has the highest amount of energy at high frequencies. Spread spectrum signals performance is comparable to that of the pulse signals.

It was demonstrated that APWP signals are attractive since any desired RF signal shape can be produced, and these signals had lowest RF sidelobes. APWP and other spread spectrum signals had similar performance in terms of the random errors of the temporal position estimation. APWP performance in the spatial domain was lower than for other signals, due to the energy losses. Artificially offset frequency (7.45 MHz instead of 5 MHz) CW toneburst produced best spatial resolution. Barker code 13 with chip size 1 period and 5 MHz CW toneburst allowed for lowest spatial position estimation errors, due to their high energy.

4.5. Deconvolution performance

The analysis presented below was aimed to investigate the APWP signals performance in iterative deconvolution, when reflections were close to overlapping.

ToF imaging in the case of close reflections is further complicated due to the neighboring reflections influence on estimated ToF [88]. Refer to Fig. 4.15 for the plot showing the errors induced on two neighboring reflections when they are becoming closer to each other.

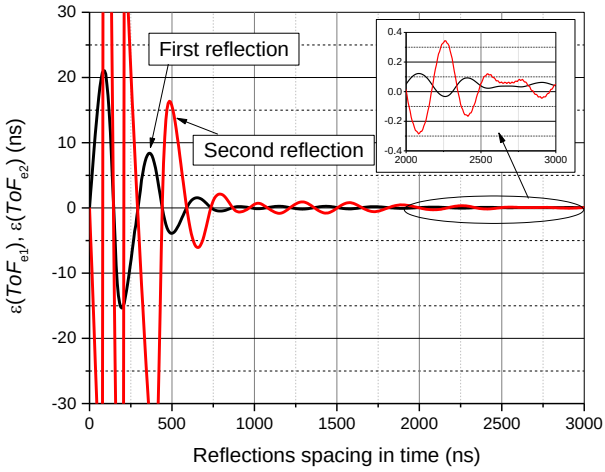

Fig. 4.15. ToF errors for first and second reflection versus reflections spacing in time [88]

It can be seen that a bias error is introduced into both reflections if they are separated by a very small distance. It was demonstrated in [88] that bias errors are present in all ToF estimation techniques. Refer to Fig. 4.16 for an example of pulse (left) and chirp (right) signals as used in the investigation.

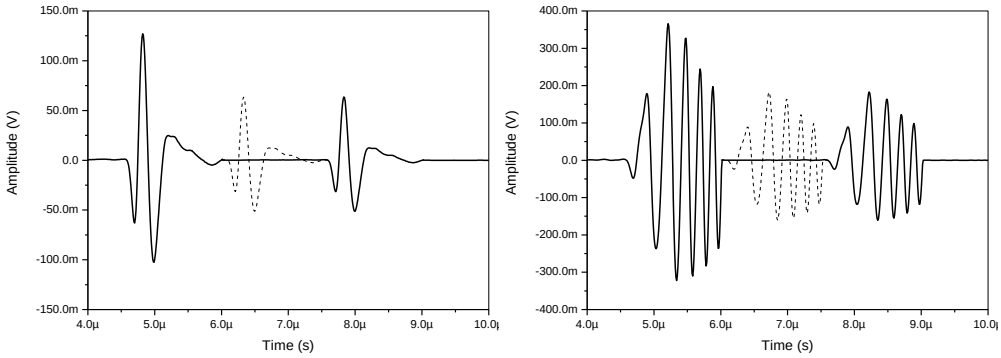

Fig. 4.16. Multilayer reflections example when short pulse is used for probing when spread spectrum (chirp) signal is used for probing

Seven signals were compared: the rectangular, 100 ns pulse; short, 0.5 μs duration 5 MHz CW toneburst; long, 2 μs duration 5 MHz CW toneburst; short, 0.5 μs duration (2-8) MHz chirp; long, 2 μs (2-8) MHz chirp; short, 0.5 μs duration APWP

signal; and long, 2 μs APWP signal. The ToF errors produced when ToF is obtained using cosine interpolation, equation (2.5), are presented in Fig. 4.17.

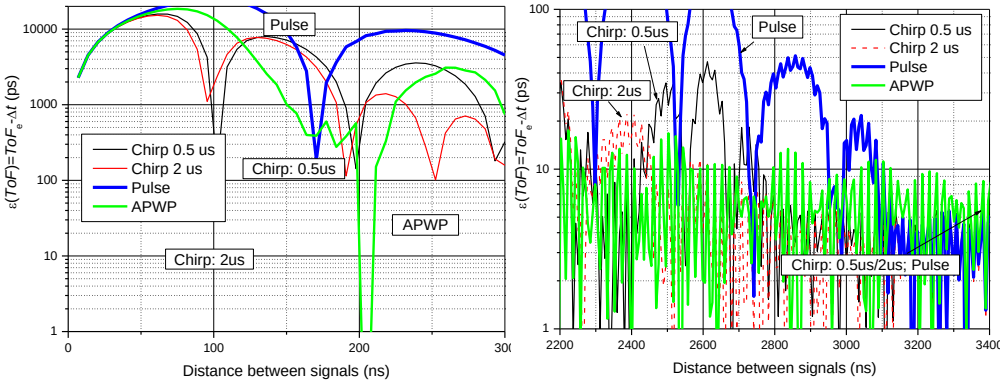

Fig. 4.17. ToF bias errors in case of two reflections proximity

As expected, long uncompressible signals had the worst performance: larger than 10 ns error was introduced when spacing between toneburst is below half of its duration. Meanwhile, long APWP and chirp signals (2 μs), which were significantly overlapping (230 ns spacing) before compression, had much better performance; even at close range: 10 ns error for pulse, 3.6 ns error for 0.5 μs chirp and 1 ns error for 2 μs chirp were obtained, which are higher than 0.5 ns error for APWP. Pulse performance was unexpected: there is no single area where pulse errors are lower than other signals. In the case of large signals spacing (2600 ns), 500 ps error for pulse, 50 ps error for 0.5 μs chirp and 12 ps error for 2 μs chirp have been obtained, which are higher than 10 ns error obtained for APWP signals. It can be concluded that APWP had the best performance in neighboring reflection bias errors reduction.

4.6. Conclusions of the 4nd chapter

APWP signals offer programmable correlation sidelobes and the ability to concentrate the excitation energy into the selected bandwidth.

It was concluded that APWP and nonlinear chirp signals have the lowest RF correlation sidelobes level, although Barker code PSK SS signal has the lowest envelope sidelobes, their level is -18 dB instead of the expected -22.3 dB. Envelope sidelobes are only 8 dB worse for APWP and nonlinear chirp, even in the case when these are not optimized for the envelope sidelobes (optimized for RF sidelobes).

It was also concluded that APWP and chirp offer the best spatial resolution. It was demonstrated that APWP signals are attractive, since any desired RF signal shape can be produced: these signals had the lowest RF sidelobes.

Bias errors are present in ToF estimation when signals are close to overlapping. It was demonstrated that long (2 μs) APWP and chirp signals, despite significant overlap, had much better performance even in iterative deconvolution at close range (230 ns). Pulse performance is the lowest: there is no single area where pulse errors are lower than other signals. In the case of large signals spacing, the APWP signal had the best performance.

5. APWP SIGNALS APPLICATION

This chapter is devoted to show and demonstrate the APWP signal properties ultrasonic applications. Four distinct applications are presented, which explore the two essential properties of these signals: spectral shape and sidelobes programmability.

Spectral shape programmability would be extremely useful when spectral compensation is required in spectroscopy. Programmable spectrum could also be useful in the case of ToF bias errors reduction in flow measurements.

Spectral flatness is also related to far range correlation sidelobes. Randomness of the signal is related to the self-noise, which in turn also defines the sidelobe level. Both high SNR and wide bandwidth are expected from APWP as representative of SS signals. The aforementioned properties are suitable for narrowband transducer band improvement. In addition, an improvement on the relative noise margin of the air coupled transducer was demonstrated.

Defect detectability was carried out on thin composite laminates for several SS (including APWP) and simple signals.

5.1. Relative noise margin improvement

Use of APWP signals was proposed to reduce the correlation function sidelobes in the case of narrowband channel in the application described below, in which the setup analyzed (Fig. 5.1) was aimed at anemometry [74].

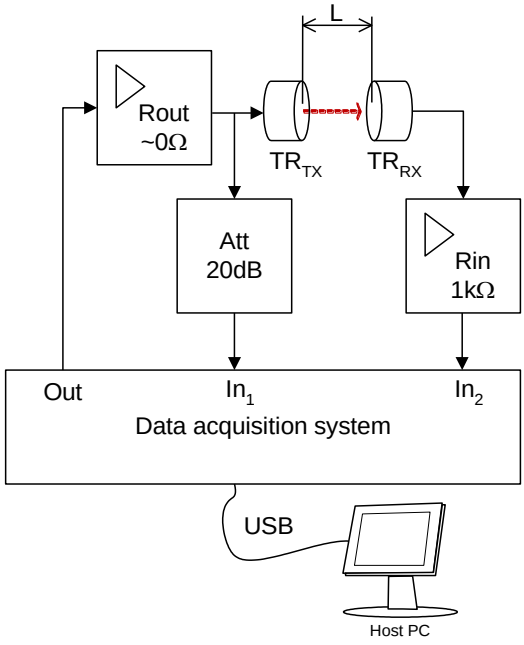

Fig. 5.1. Ultrasound transmission measurement setup

ToF estimation accuracy is extremely important in such applications, while it is of less importance in car parking, indoor navigation and ranging applications. Air

coupled transducers aimed at these applications are 40 kHz, but the bandwidth is very narrow, (1-4) kHz. While the aforementioned application can use an envelope for ToF estimation, it is desirable to use RF signals for anemometry. Going from envelope to RF would improve ToF accuracy 10 times (compare equation (1.8) and (3.9)).

A pair of transmitting transducer 400ST160 and receiving transducer 400SR160 (Pro-Wave Electronic Corp.) was placed at L=120 mm distance against each other. Transducers were placed in a cardboard box to reduce the air motion. To predict the signal performance, the AC response of the transmission channel was measured. AC response was measured using continuous wave (CW) signal for excitation. The CW was produced by direct synthesis, generated directly coupled to the acquisition system [75]. The received signal was acquired by the acquisition system, where it was then filtered using sine wave correlation (SWC) in order to extract the complex amplitudes of the transmitting and receiving transducers. The SWC procedure can be presented as covariance coefficient of sine and cosine functions to the sampled version of the measured signal s_n windowed by w_n and normalized by L1 norm $|W|_1$ of the window function:

$$V_I(f) = \frac{2\sum_{n=0}^{N-1}\left[\cos(2\pi f t_n)\cdot s_n \cdot w_n\right]}{N|W|_1}, \tag{5.1}$$

$$V_Q(f) = \frac{2\sum_{n=0}^{N-1}\left[\sin(2\pi f t_n)\cdot s_n \cdot w_n\right]}{N|W|_1}, V_0(f) = \frac{2\sum_{n=0}^{N-1} s_n}{N}. \tag{5.2}$$

Then magnitude and phase of the measured signal can be estimated using:

$$V_m(f) = \sqrt{V_I(f)^2 + V_Q(f)^2}, \phi(f) = \arctan\left(\frac{V_Q(f)}{V_I(f)}\right), \tag{5.3}$$

where the channel transmission AC response can be obtained using amplitudes of the exciting $u_{in}(f)$ and through transmitted $u_{out}(f)$ signals:

$$T(f) = \frac{u_{out}(f)}{u_{in}(f)}. \tag{5.4}$$

Results were acquired over 1 kHz to 100 kHz frequency range. Refer to Fig. 5.2 for resulting AC response plot.

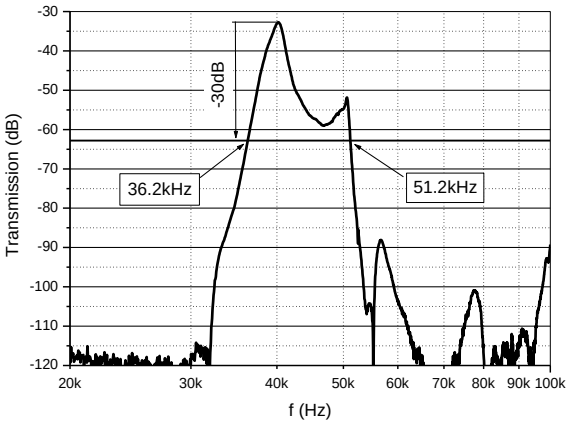

Fig. 5.2. Measured transmission using transducers pair

It can be seen that peak transmission is at 40.2 kHz (-32.8 dB). Additionally, about 12 dB lower transmission peak can be noted at 50 kHz. Passband at -6 dB level is from 38.8 kHz to 41.1 kHz i.e. 2.3 kHz range. Such narrow bandwidth will create problems in ToF estimation. Narrowband signal has a high level of correlation function sidelobes and therefore a large signal to noise ratio cannot be fully exploited.

However, it can be noted that the passband at -30 dB level is from 36.2 kHz to 51.2 kHz. The objective is to increase the excitation energy in this range, which is supposed to improve the bandwidth of the received signal so the correlation sidelobes can be reduced. Such an operation will reduce the total signal energy if the optimized signal duration has to be the same.

Therefore there is a tradeoff between i) putting all the signal energy into the passband, but increasing RF sidelobes (so the abrupt errors of ToF estimation, refer Fig. 1.2), or ii) pushing the energy into the stopband in order to reduce RF sidelobes and losing signal energy in exchange. While the CRLB equation (1.8) predicts that favor should be given to option i), RNM would predict abrupt errors performance, but a direct answer is not available without further investigation.

With a complex transmission model of the measurement channel available, optimal signal search was performed. The candidate APWP signals were constructed using a series of toggling rectangular pulses with a duration assigned by a random number generator. Randomization step was limited by the planned timer clock (8 MHz) and the assigned investigation frequencies range (from 36.2 kHz to 51.2 kHz) which defined the minimum and maximum durations of the pulse. The generated candidate APWP train was passed through the channel transmission model and the resulting signal (Fig. 5.3) was submitted for SLL and RNM analysis.

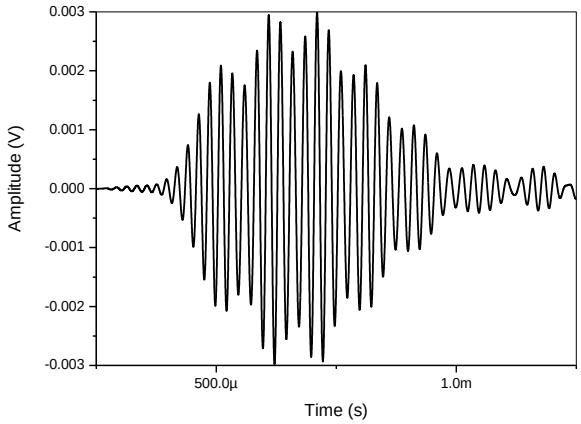

Fig. 5.3. Simulated received signal

In order to have some comparison of the attained improvement, simple toneburst was used as a reference. The same procedure was applied on the reference signal: the 40 kHz toneburst of 5, 10 and 20 periods was passed through the propagation model. The length of APWP candidates was the same as for the corresponding toneburst. Refer to Fig. 5.4 for central peak zoom of the obtained autocorrelation functions.

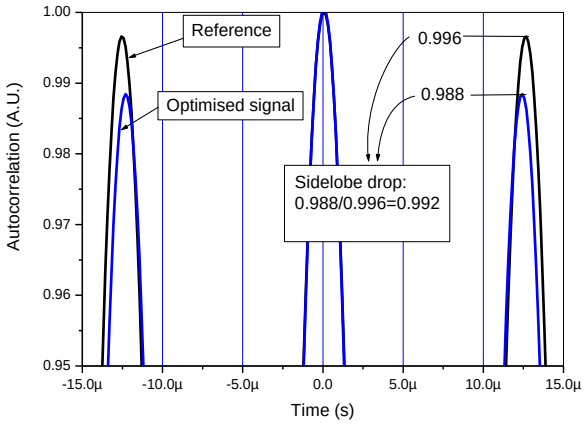

Fig. 5.4. Example of the autocorrelation function for reference and optimized signal

It can be seen that APWP (labeled as “Optimized signal” in Fig. 5.4) offers lower SLL than toneburst (labeled as “Reference” in Fig. 5.4). The SSL investigation results obtained for pulse train length corresponding to 5, 10 and 20 periods of 40 kHz toneburst are presented in Fig. 5.5. Only 200 points of each experimental set are presented with extreme points added manually.

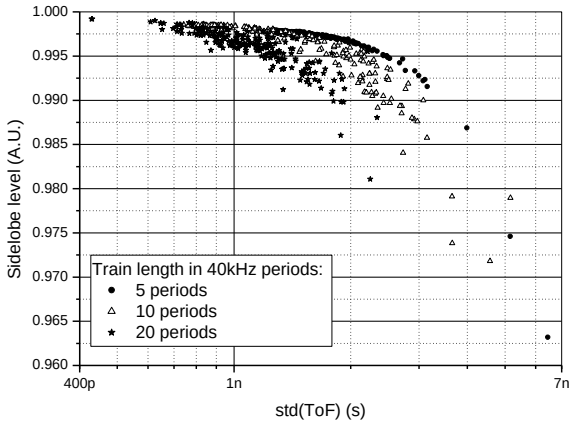

Fig. 5.5. Optimization results plot, absolute sidelobe levels

Two rare extremes can be noted on the graph: i) with significant sidelobes reduction (bottom right corner) and ii) with extremely high sidelobes (top left corner). Once uniform distribution of random numbers was used, the situation where 40 kHz component (peak transmission) and 50 kHz component appear together (right peak in AC response in Fig. 5.2) are very rare. Especially when 40 kHz and 50 kHz peaks are about the same level. It should be noted that the sidelobe level reduction also leads to an increae of ToF random errors and only rare candidates manage to achieve both low SLL levels and moderate ToF error increase.

Candidate APWP trains were selected from the optimization to investigate for the correspondence with the real experiment. The same setup as in Fig. 5.1 was used, only a microcontroller PCB capable of APWP trains generation replaced the acquisition system. APWP signals obtained in optimization were used. Each measurement was repeated 200 times and the results were averaged for better statistics. Resulting sidelobe levels for simulated (filled symbols) and experimentally obtained (hollow symbols) signals are presented in Fig. 5.6.

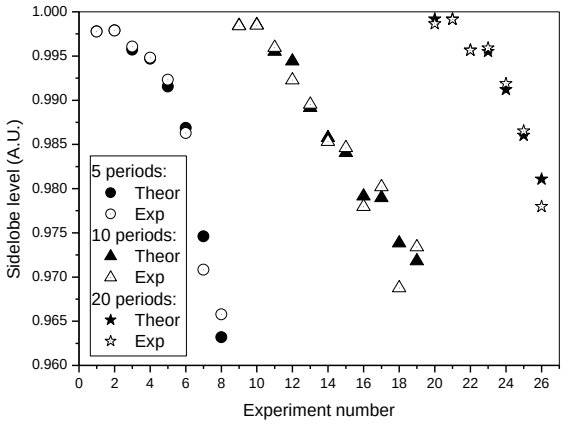

Fig. 5.6. Sidelobe levels comparison for experimentally obtained and simulated signals

It can be concluded that the model derived in the Fig. 5.6 experiment is a reliable replacement for time consuming experimental investigations. Both experimental and simulated investigation indicates that it is possible to compensate for the lack of bandwidth to gain the sidelobe level reduction.

It is worth reminding that a narrowband transducer was used and the excitation signal spectrum was allowed to span beyond the passband, causing a significant reduction of the received signal energy. This energy reduction can be attributed to a SNR decrease, which in turn will reduce the RNM. Relative sidelobe level and relative noise margin results can be compared in Fig. 5.7.

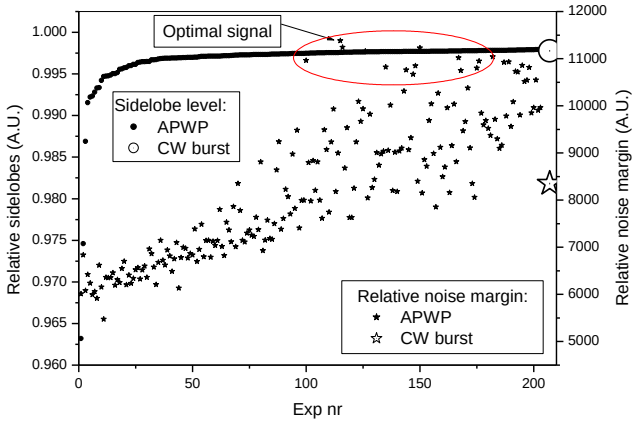

Fig. 5.7. Relative noise margin and the relative sidelobe level for candidate signals

Results were sorted according to SLL improvement. It can be seen that SLL (circles) reduction is not necessarily attribute to the improved RNM (stars): circles on the left indicate low sidelobes, but their RNM counterparts (stars, refer by Exp nr) are close or below the toneburst (large circle and start symbol on the right) performance.

It can be noted that there is a group of signals (RNM=11500, small stars within red boundary in Fig. 5.7) where there was a 40 % increase in relative noise margin, compared to the same length (but much higher energy) CW burst signals (RNM=8250, large star in Fig. 5.7 right). Significant RNM improvement is because sidelobes were very high. Therefore, even a slight reduction in SL gives much better RNM performance. Therefore, this happens only if SNR reduction is insignificant.

It can be concluded that application of APWP signals allowed both sidelobe reduction but keeping SNR level at acceptable level, so relative noise margin was improved. An increase of 40 % in relative noise margin was achieved, compared to the same length toneburst signals.

5.2. Flow measurement bias errors reduction

In chapter 2.3 it has already been demonstrated that application of SS signals reduces the ToF measurement bias errors caused by transmission asymmetry of a pair. Experiments presented below are aimed to investigate the APWP signals performance in bias errors reduction. It was hypothesized that spectral flatness is influencing the aforementioned bias errors. Since sidelobe level (SLL) is affected by spectral flatness, APWP optimization used SLL criteria.

Chirp (0.1-10) MHz 5 μs was used to build spectral system model for APWP signals derivation when the flow measurement chamber (Fig. 5.8) had no flow.

Fig. 5.8. Measurement chamber

Refer to Fig. 5.9 for signals used in spectral model construction and resulting system transmission response.

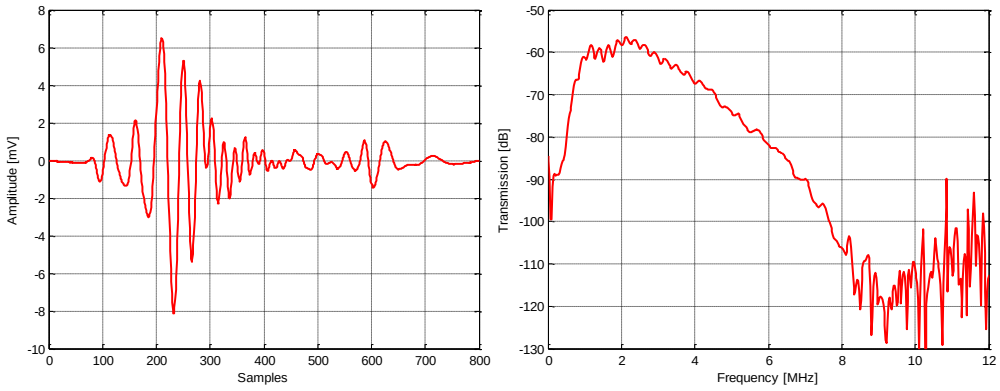

Fig. 5.9. Received signal under chirp excitation (left) and estimated transmission (right)

Only 11 APWP candidates were selected among 100 000 iterations. Optimization was using SLL of the auto-correlation function. SLL for the selected 11 candidates is given in Fig. 5.10.

It can be noted that the lowest SLL (-11.32 dB) and the narrowest mainlobe width (15.03 ns) was for the $APWP_{11}$ signal, which is unusual for standard SS signals [31]. Narrow mainlobe predicts a wide bandwidth and low SLL predicts a spectral flatness, therefore good performance in bias error reduction is expected for this signal.

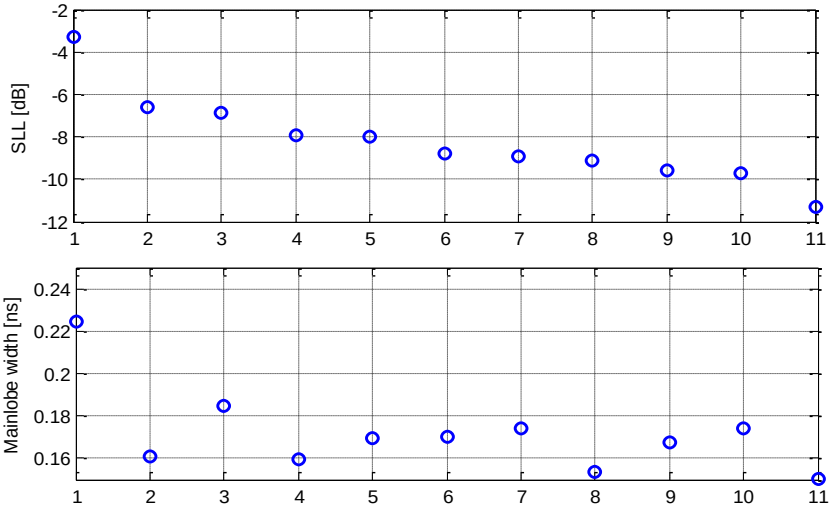

Fig. 5.10. SLL level (top) and mainlobe width (bottom) for derived 11 APWP signals

Spectrum of $APWP_{11}$ excitation signal and simulated response in frequency domain are presented in Fig. 5.12.

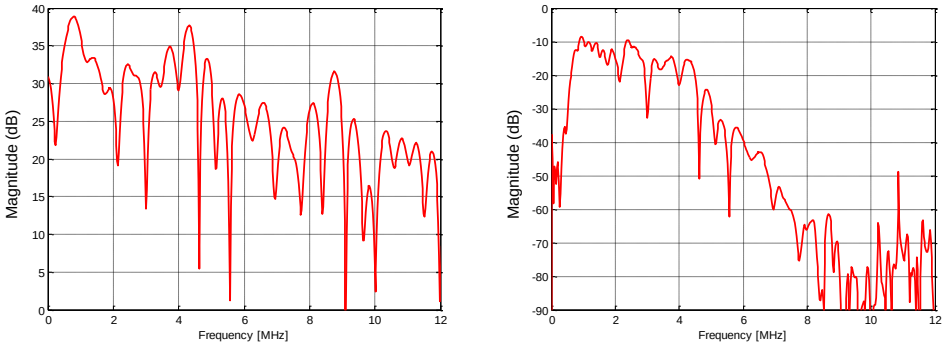

Fig. 5.11. APWP excitation signal and simulated response in frequency domain

It can be seen that APWP concentrates its spectrum at roll-off edges of the passband (Fig. 5.12 right). As a consequence, the received signal spectrum is flat.

After APWP signals has been derived, other signals were selected based on Fig. 5.9 results. The list of all signals used in the experiment are given below in Table 5.1.

Table 5.1. Excitation signals used in experiment

Signal no.	Description
1	Chirp (0.1-10) MHz, 5 μs
2	Chirp (0.1-10 MHz, 3 μs
3	Chirp (3-8) MHz, 3 μs
4	Chirp (1-5) MHz, 3 μs
5	Chirp (5-9) MHz, 3 μs
6	Chirp (1-7) MHz, 3 μs
7	Chirp (3-9) MHz, 3 μs
8	Toneburst 1 MHz, 3 μs
9	Toneburst 2 MHz, 3 μs
10	Toneburst 3 MHz, 3 μs
11	Toneburst 4 MHz, 3 μs
12	Toneburst 5 MHz, 3 μs
13	Toneburst 6 MHz, 3 μs
14	Pulse 1 MHz
15	Pulse 2 MHz
16	Pulse 3 MHz
17	Pulse 4 MHz
18	Pulse 5 MHz
19	Pulse 6 MHz
20	$APWP_1$
...	…
30	$APWP_{11}$

Signals 1 and 2 are covering the widest bandwidth, but differ in total energy. All except 1 SS signals had 3 μs duration. Signals 3 and 5 concentrate the energy at the -3 dB passband. Signals 4, 6 and 5, 7 use the left or right part of the passband correspondingly. Toneburst 8-13 and pulses 14-19 uniformly cover the passband.

The same measurement setup as in Fig. 2.7 was used. Refer to Fig. 5.12 for registered temperature values. It can be seen that temperature variation was small, 4°C maximum.

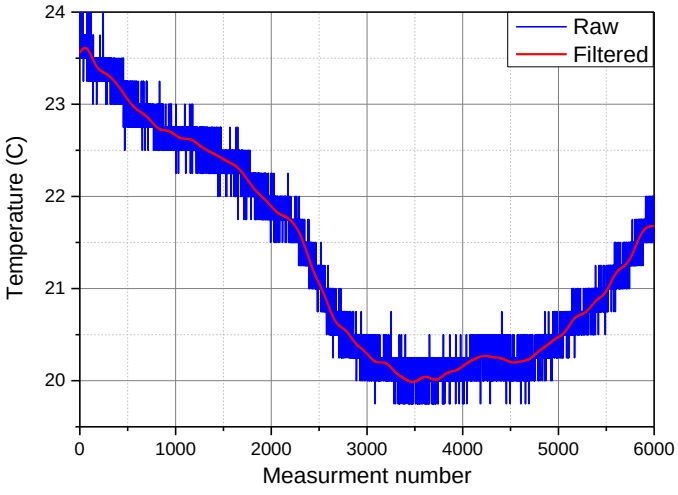

Fig. 5.12. Temperature variation during measurements

Excitation voltage was 24 V, reception gain was 20.21 dB. Flow measurement chamber (Fig. 5.8) had no flow. Ambient temperature variation during the night was used as experiment variable. Temperature changes were registered by digital temperature sensor AD7414ARTZ inserted in the measurement chamber. Experiment was carried out for 17 h.

SLL and mainlobe performance for pulse signals is presented in Fig. 5.13.

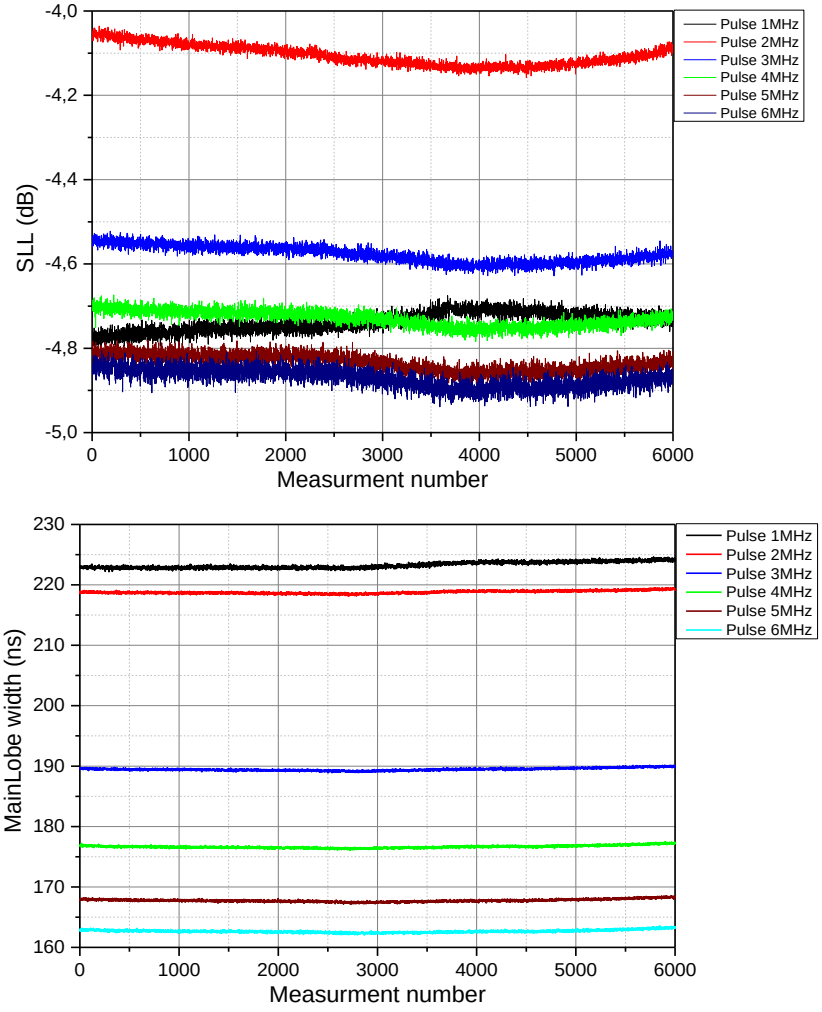

Fig. 5.13. Sidelobe level (top, SLL) and mainlobe width (bottom, MLW) variation during the experiment when pulse excitation was used

Summary of correlation function parameters for all signals is presented in Table 5.2.

Table 5.2. Correlation function parameters for all signals

Signal no.	Description	Mean SLL (dB)	Mean mainlobe width (ns)
1	Chirp (0.1-10) MHz, 5 μs	-4.608	137.955
2	Chirp (0.1-10 MHz, 3 μs	-5.359	135.191
3	Chirp (3-8) MHz, 3 μs	-3.199	98.227
4	Chirp (1-5) MHz, 3 μs	-4.144	136.273
5	Chirp (5-9) MHz, 3 μs	-8.849	99.412
6	Chirp (1-7) MHz, 3 μs	-4.420	133.955
7	Chirp (3-9) MHz, 3 μs	-3.470	99.945
8	Toneburst 1 MHz, 3 μs	-1.029	256.593
9	Toneburst 2 MHz, 3 μs	-0.348	168.043
10	Toneburst 3 MHz, 3 μs	-0.680	115.278
11	Toneburst 4 MHz, 3 μs	-1.608	90.792
12	Toneburst 5 MHz, 3 μs	-4.961	84.554
13	Toneburst 6 MHz, 3 μs	-5.372	92.353
14	Pulse 1 MHz	-4.737	223.282
15	Pulse 2 MHz	-4.105	218.799
16	Pulse 3 MHz	-4.577	189.471
17	Pulse 4 MHz	-4.730	176.656
18	Pulse 5 MHz	-4.835	167.767
19	Pulse 6 MHz	-4.871	162.672
20	APWP1	-3.766	222.399
21	APWP2	-6.357	162.584
22	APWP3	-6.488	185.811
23	APWP4	-7.136	157.730
24	APWP5	-7.720	166.026
25	APWP6	-9.150	169.426
26	APWP7	-9.314	178.387
27	APWP8	-9.472	157.656
28	APWP9	-9.143	166.387
29	APWP10	-9.973	173.437
30	APWP11	-9.789	148.832

Table 5.2 results are given in graphical form in Fig. 5.14. Note the blue line which is indicating SLL for pulse signals.

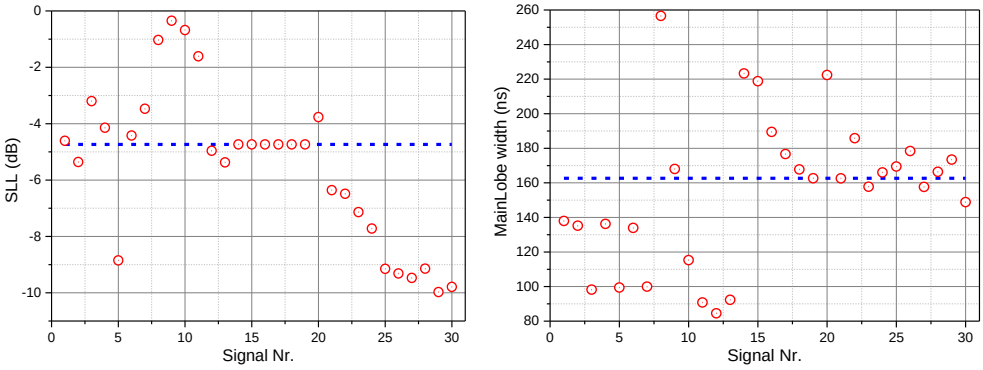

Fig. 5.14. Experimentally obtained SLL and mainlobe width mean values

It can be noted that APWP has the lowest SLL (-10 dB) while pulses and toneburst signals have only -5 dB SLL. Chirp signals had slightly narrower mainlobe width (80 ns min) compared to approximately 160 ns for the rest of the signals.

Model adequacy was checked by comparing the normalized cross-correlation (equation (3.4) between simulated and measured APWP response signals (Fig. 5.15).

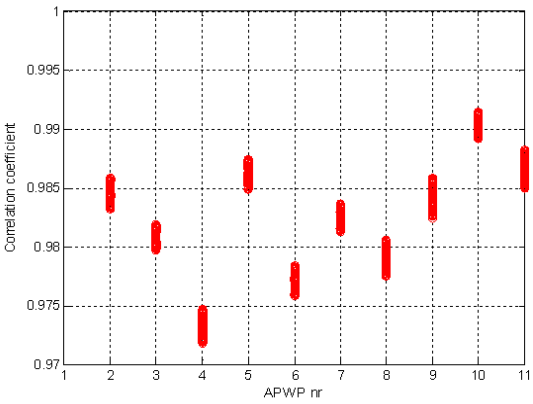

Fig. 5.15. Normalized cross-correlation peak for APWP signal

The experiment produced 6000 signals (over 17 h): this can be noted by value blur in Fig. 5.15. The lowest normalized cross-correlation was 0.97, which can be used as confirmation of the model adequacy.

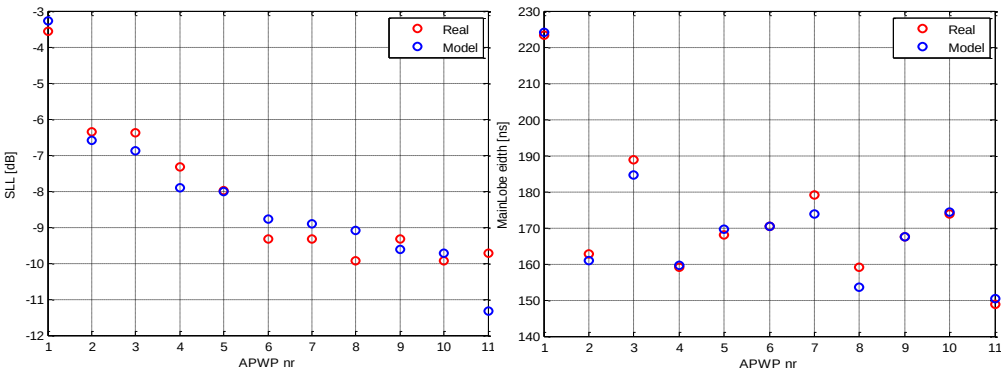

Fig. 5.16. Comparison of SLL and mainlobe width mean values in case of experimentally obtained and simulated APWP signals

Experiment results were used to calculate the differential ToF between upstream and downstream channels (equation (2.13)). Refer Fig. 5.17 left for ΔToF variation during the experiment, when chirp SS signals are used. Moving average filter (100 samples long) was used to extract the bias error (Fig. 5.17 right) from ΔToF measurements. Results for toneburst signals are presented in Fig. 5.18, pulse signals results are presented in Fig. 5.19 and APWP signals results are in Fig. 5.20.

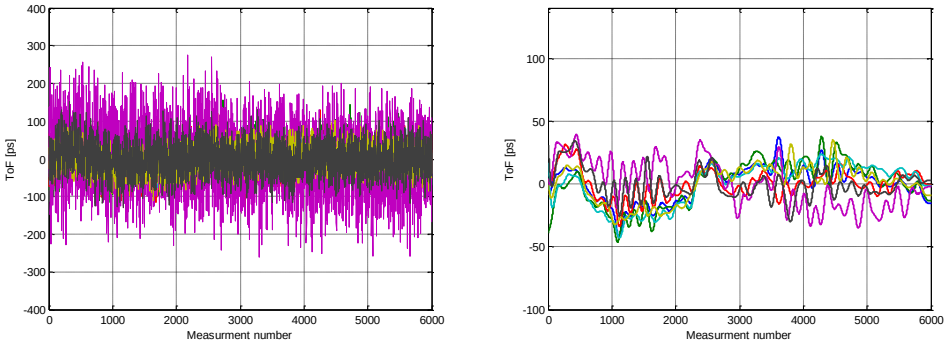

Fig. 5.17. *ΔToF* variation (left) and derived trend (bias error, right) during experiment when chips signals are used for excitation

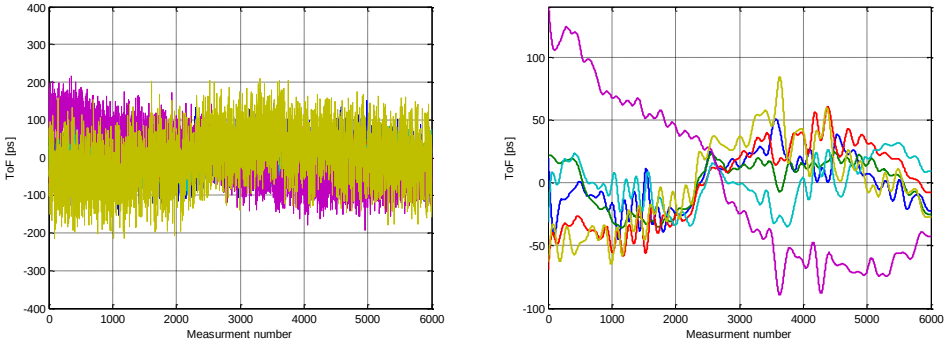

Fig. 5.18. *ΔToF* variation (left) and derived trend (bias error, right) during experiment when toneburst signals are used for excitation

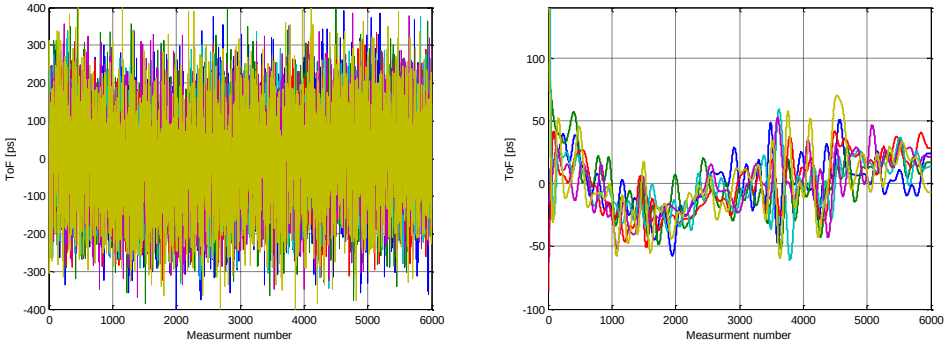

Fig. 5.19. *ΔToF* variation (left) and derived trend (bias error, right) during experiment when pulse signals are used for excitation

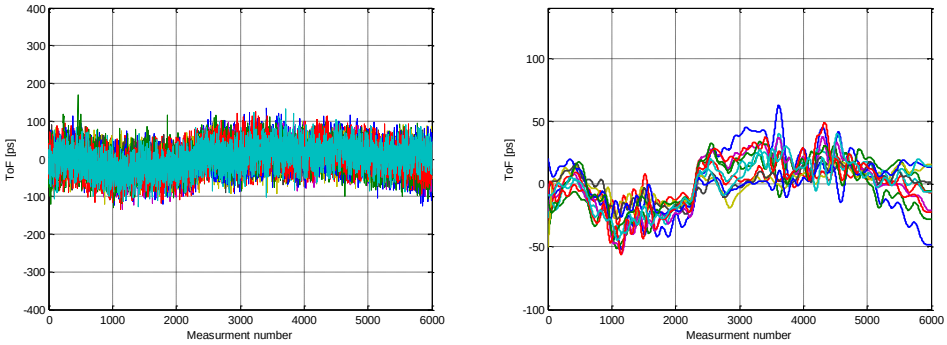

Fig. 5.20. *ΔToF* variation (left) and derived trend (bias error, right) during experiment when APWP signals are used for excitation

Errors evaluation results are summarized in Table 5.3. The mean ToF over the experiment is included, it can also be used as bias errors estimate.

Table 5.3. Differential ToF errors for all signals

Signal no.	Description	Mean ToF, ns	Std, ns	Bias, ps
1	Chirp (0.1-10) MHz, 5 μs	-0.205	0.167	-19.300
2	Chirp (0.1-10 MHz, 3 μs	-0.006	0.033	1.507
3	Chirp (3-8) MHz, 3 μs	-0.734	0.260	-11.325
4	Chirp (1-5) MHz, 3 μs	-0.357	0.348	13.057
5	Chirp (5-9) MHz, 3 μs	-0.680	0.365	-27.615
6	Chirp (1-7) MHz, 3 μs	-0.183	0.171	-5.067
7	Chirp (3-9) MHz, 3 μs	-0.627	0.408	-3.569
8	Toneburst 1 MHz, 3 μs	1.981	0.859	21.308
9	Toneburst 2 MHz, 3 μs	0.486	0.216	-43.671
10	Toneburst 3 MHz, 3 μs	0.173	0.140	35.959
11	Toneburst 4 MHz, 3 μs	-1.498	0.516	3.712
12	Toneburst 5 MHz, 3 μs	1.050	0.406	-147.419
13	Toneburst 6 MHz, 3 μs	-0.850	0.401	7.781
14	Pulse 1 MHz	1.902	1.082	-15.909
15	Pulse 2 MHz	1.984	1.063	-32.215
16	Pulse 3 MHz	1.621	1.104	-10.339
17	Pulse 4 MHz	1.253	0.233	35.682
18	Pulse 5 MHz	1.303	0.756	1.195
19	Pulse 6 MHz	1.349	0.199	6.347
20	APWP1	0.430	0.133	-38.639
21	APWP2	-0.030	0.005	9.509
22	APWP3	0.377	0.216	-1.069
23	APWP4	-0.324	0.301	11.775
24	APWP5	0.783	0.296	-10.149
25	APWP6	-0.193	0.011	10.898
26	APWP7	0.438	0.124	-0.474
27	APWP8	0.438	0.194	7.905
28	APWP9	0.309	0.161	-6.348
29	APWP10	0.115	0.118	-14.003
30	APWP11	-0.519	0.453	20.223

Differential ToF errors are summarized graphically in Fig. 5.21. Note that the blue dotted line, which indicates best result for pulse signals.

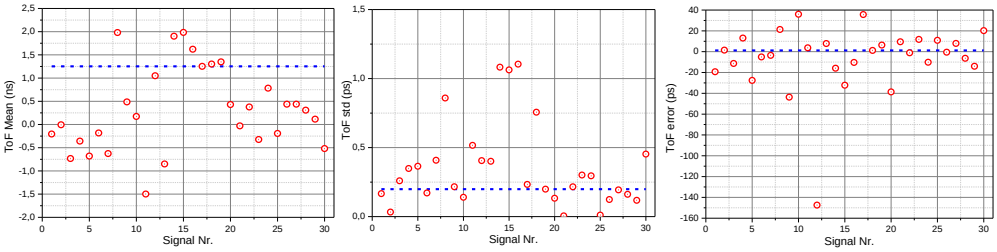

Fig. 5.21. Differential ToF errors for all signals

It can be concluded that APWP and chirp signals have the best performance in differential ToF errors reduction.

Differential ToF errors obtained in experiments were converted into flow parameters. Summary of conversion results are presented in Table 5.4.

Table 5.4. Differential ToF errors influence on flow parameters

Signal no.	Description	Mean flow rate, l/h	Total volume, l
1	Chirp (0.1-10) MHz, 5 µs	-0.431	-6.469
2	Chirp (0.1-10 MHz, 3 µs	-0.012	-0.179
3	Chirp (3-8) MHz, 3 µs	-1.545	-23.158
4	Chirp (1-5) MHz, 3 µs	-0.753	-11.282
5	Chirp (5-9) MHz, 3 µs	-1.432	-21.472
6	Chirp (1-7) MHz, 3 µs	-0.385	-5.775
7	Chirp (3-9) MHz, 3 µs	-1.319	-19.776
8	Toneburst 1 MHz, 3 µs	4.171	62.532
9	Toneburst 2 MHz, 3 µs	1.024	15.350
10	Toneburst 3 MHz, 3 µs	0.364	5.453
11	Toneburst 4 MHz, 3 µs	-3.153	-47.267
12	Toneburst 5 MHz, 3 µs	2.211	33.143
13	Toneburst 6 MHz, 3 µs	-1.790	-26.836
14	Pulse 1 MHz	4.004	60.017
15	Pulse 2 MHz	4.178	62.626
16	Pulse 3 MHz	3.413	51.169
17	Pulse 4 MHz	2.638	39.536
18	Pulse 5 MHz	2.743	41.125
19	Pulse 6 MHz	2.840	42.564
20	APWP1	0.905	13.573
21	APWP2	-0.062	-0.935
22	APWP3	0.794	11.899
23	APWP4	-0.682	-10.223
24	APWP5	1.649	24.716
25	APWP6	-0.405	-6.077
26	APWP7	0.922	13.826
27	APWP8	0.922	13.827
28	APWP9	0.650	9.740
29	APWP10	0.241	3.615
30	APWP11	-1.093	-16.383

Flow parameters variation graphically is presented in Fig. 5.22.

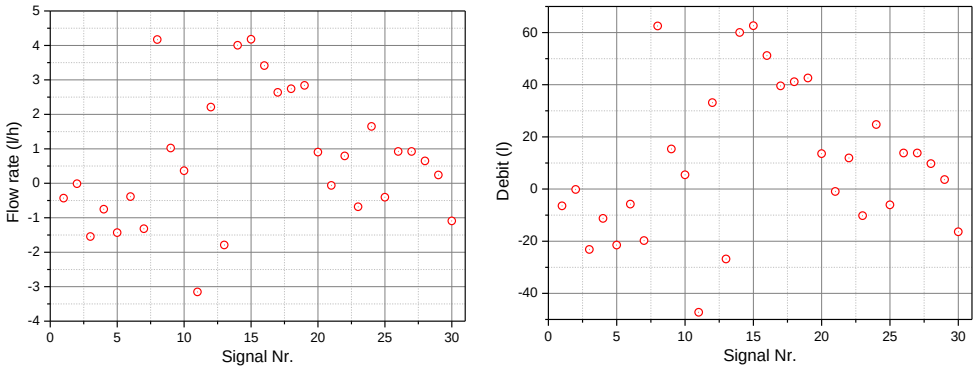

Fig. 5.22. Differential ToF errors influence on flow rate (left) and total volume (right)

Total volume variation in time, caused by differential ToF errors is presented in Fig. 5.23.

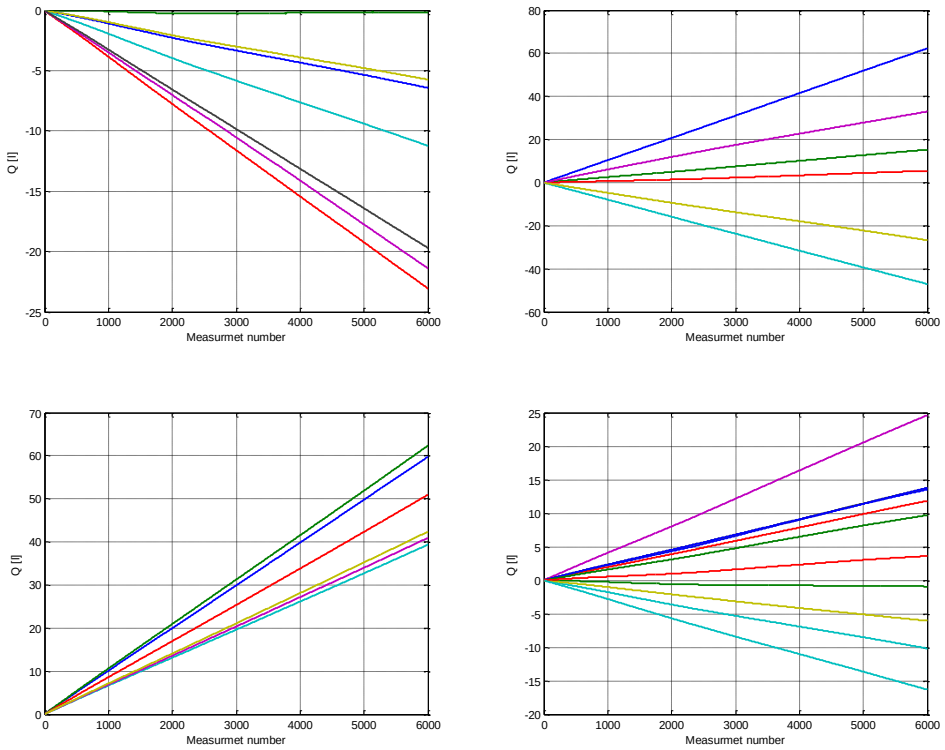

Fig. 5.23. Total volume variation caused by bias errors for chirp (up-left), toneburst (up-right), pulse (bottom-left) and APWP (bottom- right)

It can be seen that the widest chirp (0.1-10) MHz, 3 μs duration accumulated 0.179 l over the experiment duration (17 h). Other chirp signals had 5 to 23 litters

error in total volume. $APWP_2$ signal provided similar results: mean flow rate deviation was 0.062 l/h and total volume error was 0.935 l (other APWP – from 3 to 24 l). Toneburst – from 5 l to 62 l, pulse signals from 39 l to 62 l. It can be concluded that chirp and APWP signals have similar performance and allow for 10 to 100 times reduction of total volume error.

5.3. Defect detectability in layered laminates

Thin fiberglass laminates are used in multilayer PCB manufacturing. If buried capacitance is embedded in one of the layers, then EMI robustness of the electronic device is ensured [84,94]. High relative permittivity material is stacked between two copper layers to increase the embedded capacitance, but it is difficult to avoid trapping air bubbles in PCB prepreg in manufacturing. Inclusions are of lower permittivity, therefore some areas of embedded capacitance will have reduced capacitance per are. Filler with higher relative permittivity is more sensitive for any inclusions. A customer indicated the task for NDT: locate the trapped air bubbles down to 100 μm in PCB laminate. The inspected PCB laminate had 100 μm dielectric thickness (Fig. 5.24 left) sandwiched between two 10 μm copper foils. Defects were located in the upper third of the scanned area (Fig. 5.24 right).

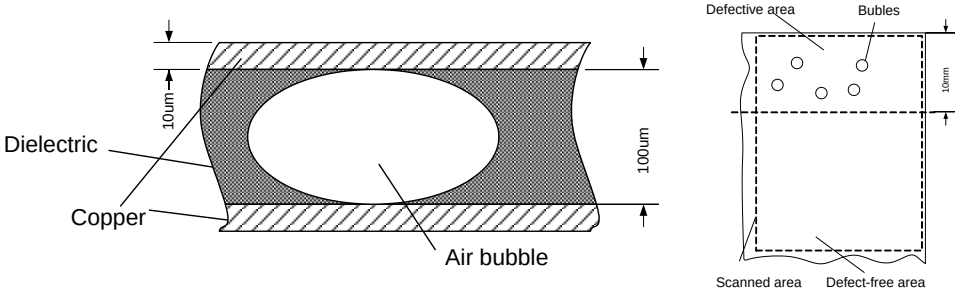

Fig. 5.24. Cross section of the PCB layers (left) and drawing of the scanned area (right) [91]

The arrangement of the layers (Fig. 5.24 left) indicates that there will be two types of reflections prevailing: i) in the defect free zone reflections will come from the copper-dielectric-copper stack; ii) in areas where trapped air bubbles are present, reflection from the copper-air layer will prevail. Reflection from the defect-free stack can be modeled using equations (1.13)-(1.15). Assuming c_{water}=1420 m/s, c_{Cu}=4660 m/s, $c_{dielectric}$=3070 m/s and ρ_{water}=1 g/m^3, ρ_{Cu}=8.93 g/m^3 $\rho_{dielectric}$=1.5 g/m^3 the stack reflectivity in the frequency domain is obtained (Fig. 5.25 left). Reflectivity for the case where the bubble is completely replacing the dielectric is presented in Fig. 5.25 right with c_{air}=340 m/s and ρ_{air}=0.001225 g/m^3.

It can be seen that the essential resonance will be at 14.6 MHz (reflectivity 0.2) and additional resonances will be at 18.2 MHz (reflectivity 0.6) and 29.6 MHz (reflectivity 0.5). If a defect is present, only a weak resonance at 5 MHz appears (reflectivity 0.78).

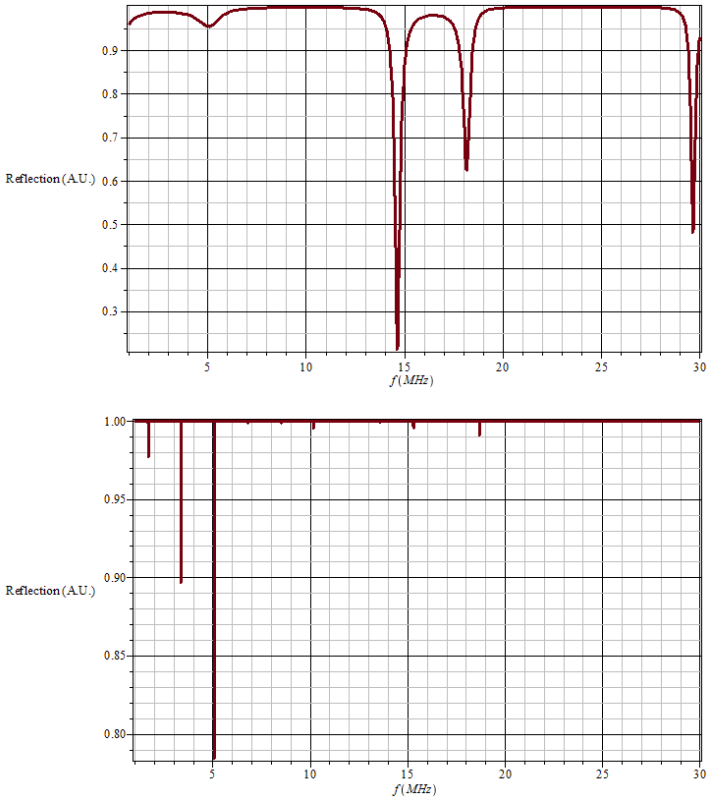

Fig. 5.25. Reflectivity frequency response for defect-free zone (top) and bubbly zone (bottom)

Wideband, spherically focused, 10 MHz center frequency and 3 MHz to 19 MHz bandwidth (-20 dB) ultrasonic transducer IRY210 (from NDT transducers LLC) was used. The region of interest (ROI) was selected at the edge of the laminate and a 230x250 mm area (Fig. 5.24 right) was scanned using 0.1 mm step. A-scans reflected from the laminate surface were collected (Fig. 5.26).

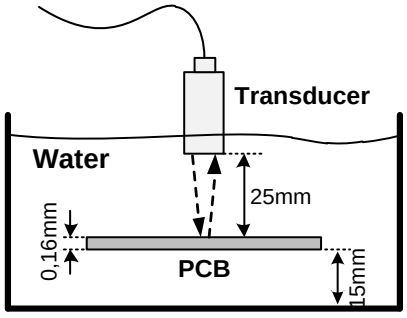

Fig. 5.26. Measurement setup for PCB inspection

Signals collection has been done using short, 50 ns duration 15 V amplitude rectangular pulse for probing and 11 dB receiving gain using an acquisition system

[83]. Initially, it was assumed that amplitude of the reflection will be influenced by the inner structure of the laminate. A-scans were gated to leave just the reflection from the sample surface. Peak value (Fig. 5.27 left) and RMS value (Fig. 5.27 right) of the raw data was plotted as C-scan. Taking the peak value supposed to maximize the contrast, therefore RMS value should have better SNR.

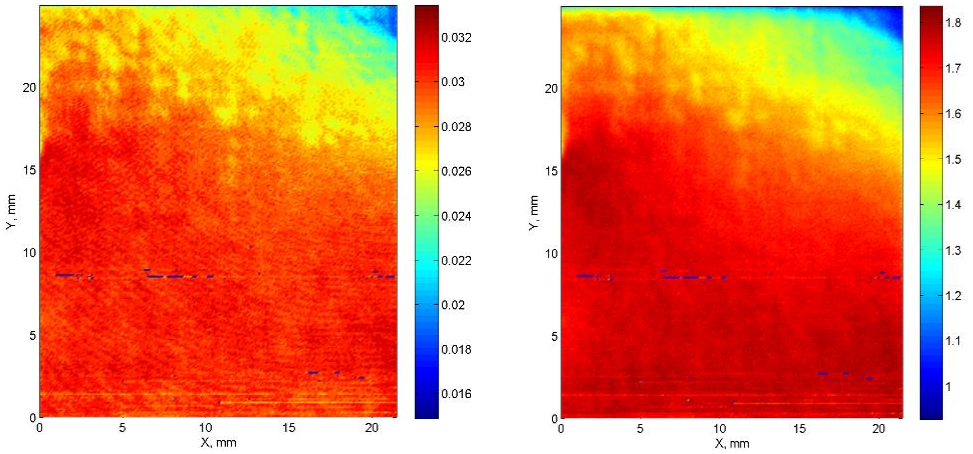

Fig. 5.27. C-scan of the preliminary scan using rectangular pulse: peak value of raw data (left) and RMS (right)

Unfortunately, no significant indication of defects can be seen in the image above. The explanation could be that reflection from defect-free laminate is masking slight variations in the signal due to a trapped bubble. Horizontal strips at *y* coordinate 0 to 3 mm and at 8 mm have occurred due to an air bubbles build-up on the transducer surface during the scanning process.

Spectroscopy [85] has been carried out for defects indication. Results at 13 MHz and 11.42 MHz are presented in Fig. 5.28.

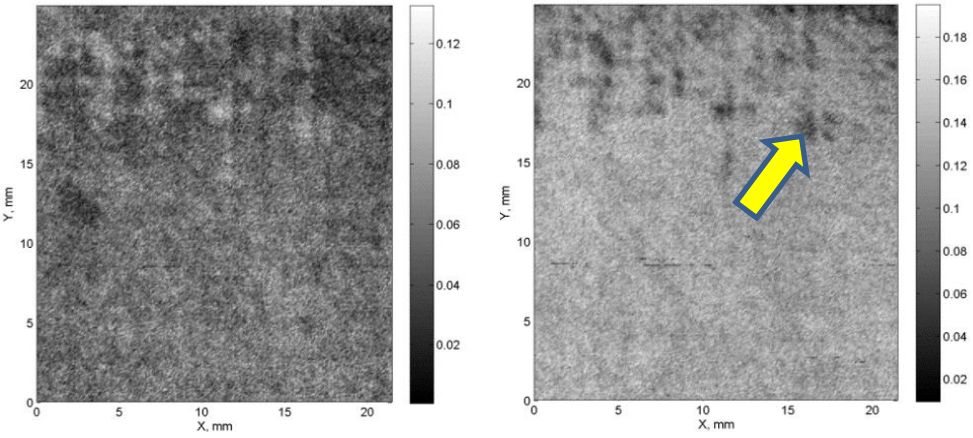

Fig. 5.28. C-scan of the spectroscopy at 13 MHz (left) and 11.42 MHz (right) using pulse

Though signals from the bubbles can be detected now, the quality of the image obtained is not sufficient for reliable inspection. A better probing signal and processing was needed. An effective technique for inclusions location using ultrasonic inspection was proposed. It is based on the assumption that the majority of the PCB area inspected does not contain defects. Then, an averaged signal from all the inspection area is representing a defect-free A-scan. Subtracting such a signal from the A-scan obtained at every individual position would enhance the signal from faulty areas.

Cross-correlation function with cosine interpolation (equations (2.4) and (3.4)) was used for *ToF* estimation. A-scan at coordinates 0,0 was used as a reference signal. The obtained ToF_{ss} was used to subsample-shift each signal *s* to get a new signal *ssa*, which was then aligned with the A-scan at coordinates 0,0 s_a:

$$ssa_{1..k}\left(t - ToF_i\right) = \mathrm{IDFT}\left[\mathrm{DFT}\left(s_{1..k}\right) \cdot e^{j\omega_{1..k} ToFss_i}\right]. \tag{5.5}$$

The aligned signals were averaged to produce a reference signal *sr;* representing defect-free zone:

$$sr_{i,j} = \frac{\sum_{j=1}^{J}\left(\sum_{i=1}^{I} s_{i,j}\right)}{I \cdot J}. \tag{5.6}$$

Then, the signal *sr* was subtracted from every individual A-scan by adjusting its temporal position ToF_{adj} and amplitude *Amp*:

$$ss_{1..k} = s_{1..k} - Amp \cdot sr\left(ToF_{adj}\right)_{1..k}, \tag{5.7}$$

where *Amp* is:

$$Amp = \frac{\sum_{k=1}^{K} sr_k \cdot s_k}{\sum_{k=1}^{K}\left(sr_k\right)^2}. \tag{5.8}$$

It is essential that this technique does not require additional measurement for reference signal production. The reference signal is produced by taking the average of measurement signals over a sufficient surface area. Results are better than the ones obtained by spectroscopy (Fig. 5.28). Yet, horizontal strips at y coordinate 0 to 3 mm have occurred due to signal energy reduction caused by an air bubbles build-up on transducer surface.

The remainder of frontface signals subtraction *ss* were used to obtain the peak (Fig. 5.29 left) and RMS values (Fig. 5.29 right), which were used for C-scan image construction.

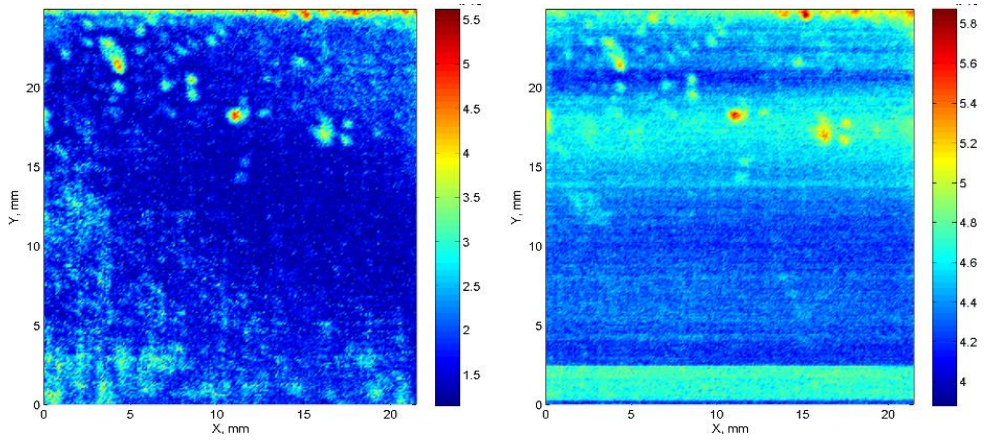

Fig. 5.29. C-scan of the average stripping algorithm application on figure 3 data: peak (left) and RMS (right)

It can be seen that the average stripping significantly enhances the information from the defective areas. A search for a better probing signal was done in order to improve the imaging results. The energy of the probing signal can be increased by using continuous wave (CW) toneburst. However, temporal resolution and bandwidth will suffer. Spread spectrum signals offer both high SNR and resolution [86,73]. Chirp and PSK (13 elements Barker) SS signals were selected. APWP signals were derived using a model from a previous measurement. Optimization was done according to SLL criteria. Thirteen signals were derived for analysis (Table 5.5).

Table 5.5. Full set of the excitation signals used

No.	Signal type	Parameters	Notes
Gencode1	Pulse	2 samples	wide bandwidth
Gencode2	Pulse	3 samples	Best side lobes
Gencode3	Pulse	13 samples	For high signal energy (STD)
Gencode4	CW burst	10 MHz @ 3 μs	
Gencode5	CW burst	15 MHz @ 3 μs	
Gencode6	APWP	3 μs duration	Highest main/side lobes energy ratio
Gencode7	APWP	3 μs duration	Lowest mainlobe width
Gencode8	Chirp	1-20 MHz @ 3 μs	
Gencode9	Chirp	1-20 MHz @ 6 μs	
Gencode10	Chirp	1-20 MHz @ 9 μs	
Gencode11	Barker Code	Chip size in half periods 2	
Gencode12	Barker Code	Chip size in half periods 3	
Gencode13	Barker Code	Chip size in half periods 5	

Toneburst signal 5 was selected based on the analysis of the spectral response ratio (Fig. 5.30) of a signal from the defective zone (note the arrow in Fig. 5.28 in cor. x=15.7 mm, y=17.1 mm) and the averaged reference signal.

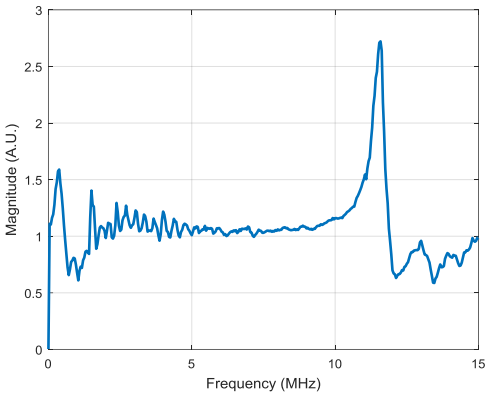

Fig. 5.30. Spectral response ratio of signal from defective zone and averaged reference signal

The five best performing candidate signals were selected for further analysis. Refer to Table 5.6 for signals description.

Table 5.6. Reduced set of the excitation signals

Signal type	**Parameters**
Rectangular pulse	20 ns
CW toneburst	10 MHz 3 μs
APWP	3 μs duration
Chirp	(1-20) MHz 3 μs
Barker Code 13	Length 13, chip 1.5 periods

The amplitude of all signals was 15 V. Pulse and toneburst are chosen as simple signals. Chirp, Barker code and APWP signals are spread spectrum representatives, therefore should offer high SNR and bandwidth. Total length of toneburst and spread spectrum signals was 3 μs. Spectrums of the candidate signals obtained for reflection from the stainless steel slab are presented in Fig. 5.31.

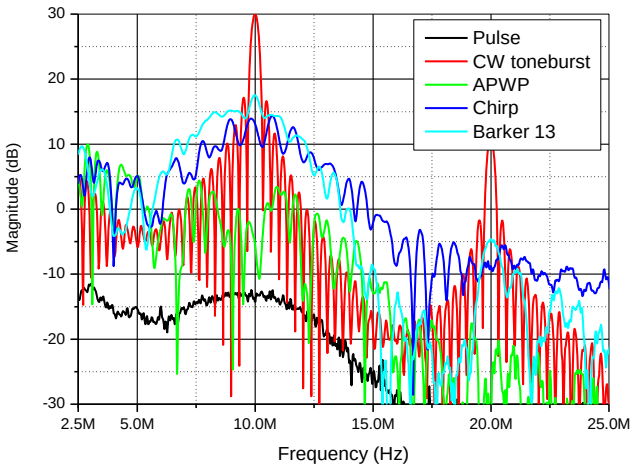

Fig. 5.31. Spectrums of the candidate signals used in investigation

It can be seen that pulse has the lowest energy, and it is concentrated at low frequencies. Toneburst has the highest energy, but most of it is concentrated at 10 MHz. Since it is a non-sinusoidal signal, the second harmonic is also present. Chirp has a sufficiently large energy and is covering a wide frequency range. Barker has more energy than chirp around the center frequency, but has significant energy reduction at high frequencies compared to chirp. APWP signal has similar to pulse spectral shape but possesses significant energy losses.

The same area was scanned, using all signals simultaneously. Average stripping procedure was applied after data collection. Results for four high energy signal can be compared in Fig. 5.32.

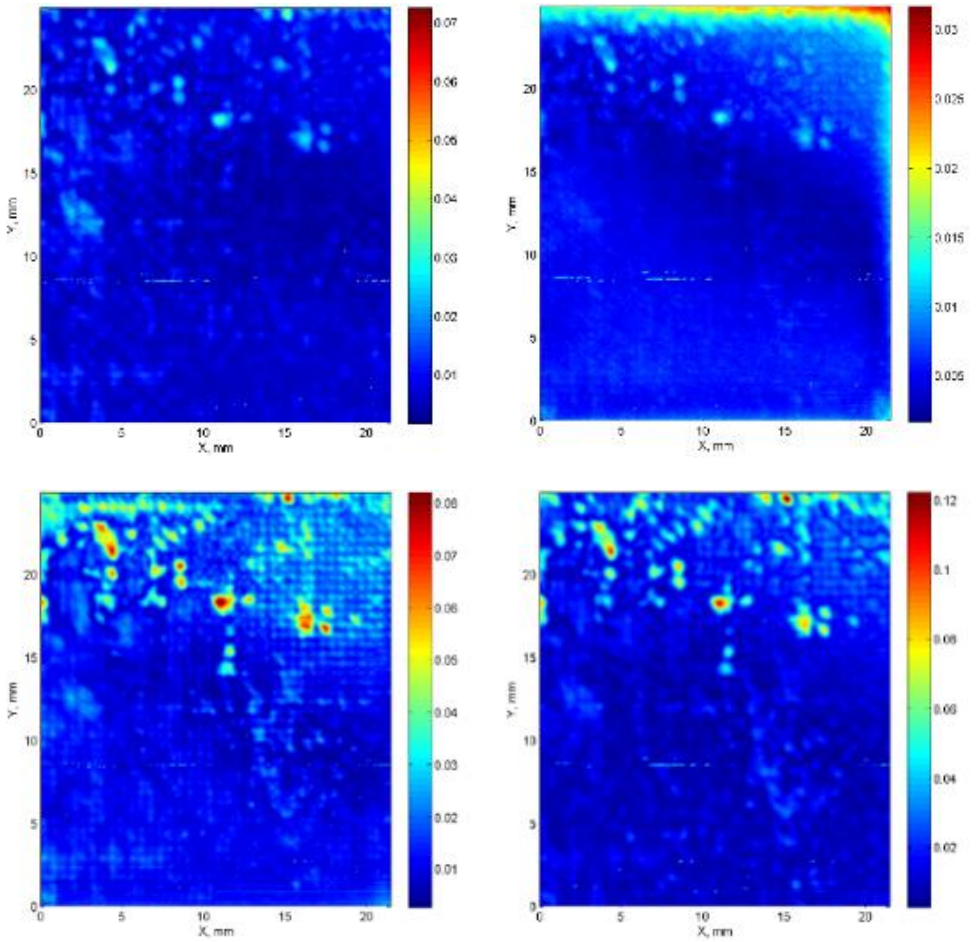

Fig. 5.32. C-scan of the average stripping application using peak value for: toneburst (top-left), APWP (top-right), chirp (bottom- right) and PSK (bottom-left)

It can be seen that chirp and PSK (Barker 13) produced the best contrast. The reason for lower APWP performance is that APWP is the only signal which was able to efficiently detect the delamination at the upper part of the image. These large signals from edge defect reduce the image dynamic range.

Probability of detection analysis was carried out. Since there was no information on the inner structure of defects, it was assumed that all signals contain some useful information about the defects. Signals were averaged first, then thresholded at 0.5. The resulting mask (see Fig. 5.33) was used as a reference map of the defects.

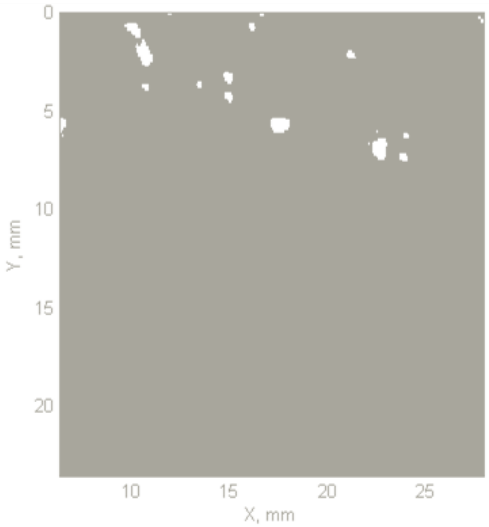

Fig. 5.33. C-scan of the reference map of the defects

Every signal set was analyzed by varying the threshold and evaluating the detection and the false alarm rate. The receiver operating curves (ROC) produced are presented in Fig. 5.34.

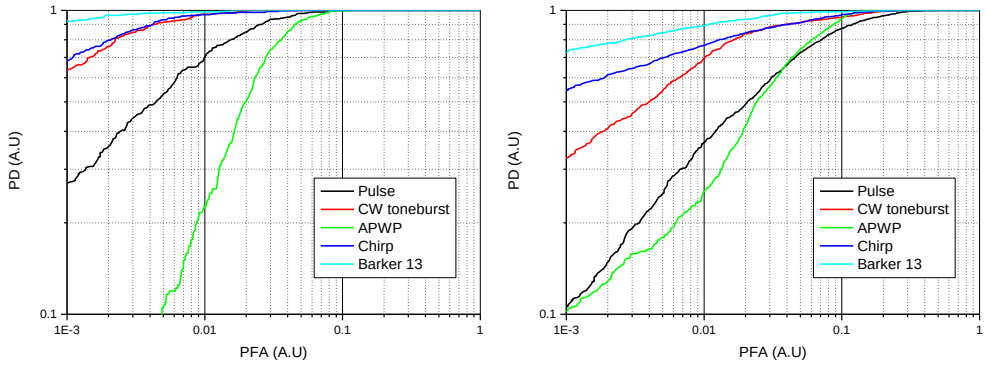

Fig. 5.34. ROC curves for several probing signal types: peak (left) and RMS (right)

It can be seen that the best performance was found for Barker 13 code. CW toneburst and chirp performance is also acceptable. Pulse and the APWP performance at 1 % probability of false alarm are not acceptable. If 10 % false alarm rate is used, all signals have similar performance: 100 % detection probability.

It can be concluded that chirp and Barker spread spectrum signals have the best performance in detection. A simple yet efficient technique was suggested for air bubbles detection in thin PCB laminate. This technique does not require any additional

measurement and is applicable for online inspection. The reference signal can be produced by running the average of raw data acquired within some time period.

5.4. Spectral loses compensation

While electronics used in ultrasonic measurements can be wideband, the transducer is significantly altering the spectral content. Furthermore, as it was demonstrated in chapter 1.3, the thickness resonances also modifies the transmission in the material. Spectral losses can be compensated for by altering the excitation signal spectrum. Simple signals (pulse, step and toneburst), PSK and linear chip do not have the ability to program the excitation spectrum, while nonlinear chirp and arbitrary waveform signals allows to control the spectral content of the excitation signal. The analysis presented below was aimed to demonstrate the ability of APWP signals to compensate for the spectral losses without significant SNR degradation.

5.4.1. Spectral loses optimization

A relatively flat passband ultrasonic transducer was simulated using a second order Butterworth bandpass filter with a center frequency of 1 MHz and bandwidth 0.6 MHz. The transducer was excited by a LFM (chirp) binary excitation (bipolar) signal with a frequency span 0.5 MHz to 1.5 MHz (Fig. 5.35 left). This signal was used to obtain the system transmission response (Fig. 5.35 right).

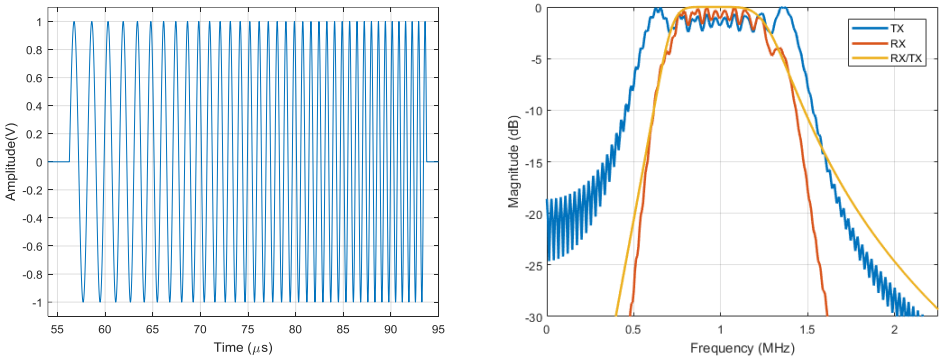

Fig. 5.35. Linear chirp excitation signal (left), signals and obtained transmission in frequency domain (right)

The system transmission response was obtained by taking the Fourier transforms of the probing and the response signals and dividing the received signal $S_{RX}(f)$ by the transmitted signal spectrum $S_{TX}(f)$:

$$G(f) = \frac{S_{RX}(f)}{S_{TX}(f)}. \tag{5.9}$$

It has to be noted that the transducer AC response (Fig. 5.35) is narrower than the excitation signal. Spectral losses can be compensated for by enhancing the attenuated components in the excitation signal using equation (1.17), but in such a case;

SNR will degrade such inverse filtering performance. A Quasi-Wiener [59] filter can be used instead:

$$C_{mp}(f)=\frac{\left|S_{RX}(f)\right|}{\left|S_{RX}(f)\right|^2+\alpha\cdot\max\left(\left|S_{RX}(f)\right|^2\right)}, \tag{5.10}$$

or desired compensation shape *W(f)* can be programed using:

$$C_{mp}(f)=\frac{\left|W(f)\right|}{\sqrt{\left|S_{RX}(f)\right|^2+\alpha\cdot\max\left(\left|S_{RX}(f)\right|^2\right)}}. \tag{5.11}$$

Amplitude modulation as proposed by Toh and Motooka in [89]. The obtained compensation function can be used to provide amplitude modulation for the original signal Fig. 5.35, by multiplying the original transmitted signal spectrum $S_{TX}(f)$ to compensation function:

$$S_{TXAMC}(f)=S_{TX}(f)\cdot C_{mp}(f). \tag{5.12}$$

Refer to Fig. 5.36 for transmitted and received signals compensated using equation (5.10) and (5.11) correspondingly.

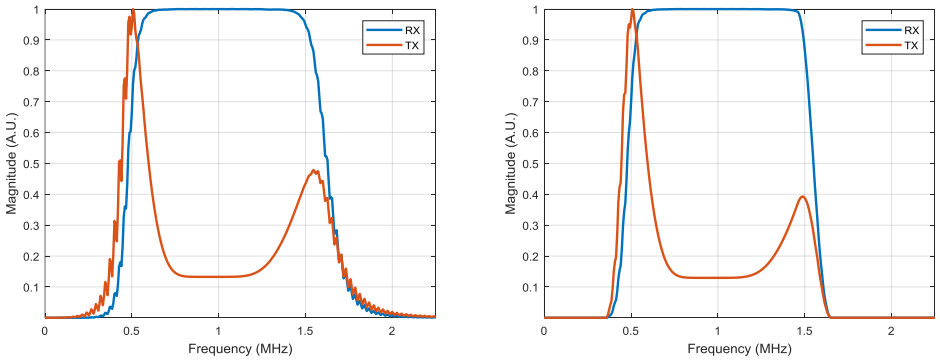

Fig. 5.36. Spectral losses compensation using AM results when quasi Wiener (left) and direct definition (right) filters are used to calculate the compensation function

The received signal has an extremely flat spectrum and improved bandwidth (0.5 MHz to 1.5 MHz instead of 0.7 MHz to 1.3 MHz, i.e. 0.6 MHz bandwidth was increased almost twice, up to 1 MHz). It can be concluded that the application of AM provides a smooth spectral response of the received signal, but such excitation signals should be treated as arbitrary waveform, because their shape is complex (Fig. 5.37).

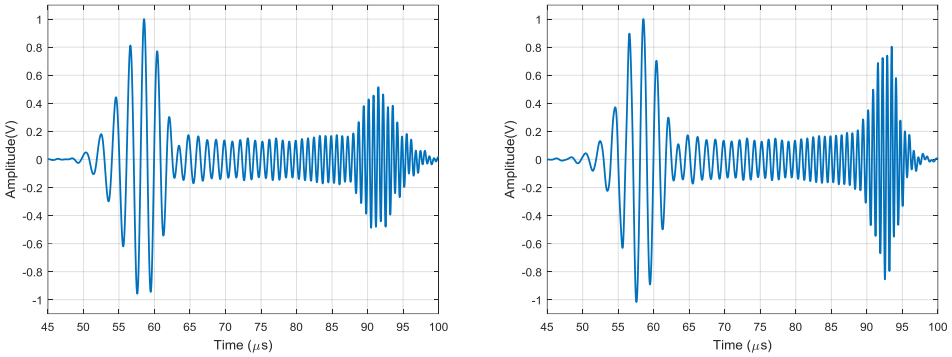

Fig. 5.37. Excitation signal used for spectral losses compensation when quasi Wiener (left) and direct definition (right) filters are used

It can be concluded that such signals use the power amplifier output swing inefficiently: only a small portion of the signal has the full amplitude swing (note two peaks at signal edges). Nonlinear frequency modulation spread spectrum signals (both linear frequency modulation and nonlinear frequency modulation) explore the amplifier capabilities better.

It was demonstrated in [78] that NLFM signals can be used to provide the programmable spectrum. The spectral programming idea is based on finding that slowly varying instantaneous frequency produces higher spectral components. The same compensation function as in the AM case has been used in an experiment to obtain the time-frequency relationship.

$$\tau(f') = \int_0^{f'} \left| S_{TXAMC}(f) \right|^2 df \ . \tag{5.13}$$

Obtained relationship (Fig. 5.38 left) represents the accumulative phase required to obtain the required $S_{TX}(f)$ magnitude response.

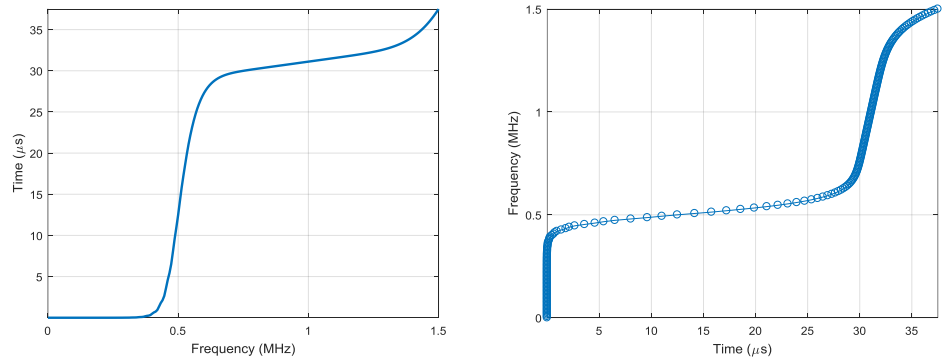

Fig. 5.38. Inverse transformation

Unfortunately, this relationship cannot be directly inversed to obtain the instantaneous phase of an NLFM, because the grid is non-uniform (Fig. 5.38 right). Inverse procedure is required to obtain the instantaneous phase. Since analytical inversion is not possible [18], the approximate solution is obtained by interpolating and resampling the function in Fig. 5.38. MATLAB procedure interp1 was used:

$$\tau(f') \xrightarrow{INTERP} f'(\tau). \tag{5.14}$$

Conversion of the instantaneous phase into accumulative phase was by integration:

$$\theta(t') = \int_0^{t'} f(t)dt. \tag{5.15}$$

Instantaneous phase was used to produce a sensitivity-compensated NLFM signal:

$$S_{TXFMC}(t) = \sin(2\pi\theta). \tag{5.16}$$

Refer Fig. 5.39 for NLFM signal produced.

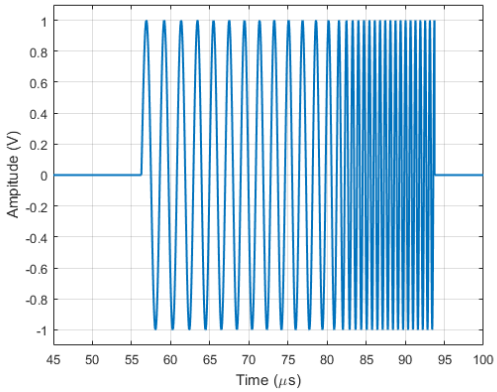

Fig. 5.39. Excitation NLFM signal with losses compensation

It can be seen that the NLFM signal effectively explores the output range of the excitation amplifier: signal amplitude is always constant. The energy of such a signal should be higher than the AM-compensated signal, due to constant amplitude: even taking into account that the AM-compensated signal is slightly longer (compare Fig. 5.38 and Fig. 5.39). Unfortunately, the spectrum of NLFM contains ripples (Fig. 5.40).

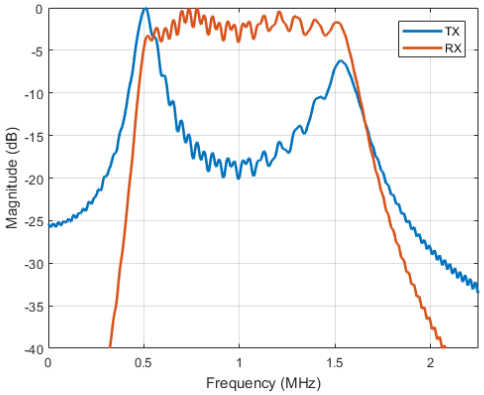

Fig. 5.40. Frequency domain representation of transmitted and received signals when Spectral losses compensation was done using NLFM signal

Spectral ripples can be explained by the non-ideal time-frequency inversion procedure and rectangular shape of the envelope. Ripples are within the 4 dB range, which could be acceptable if the signal is used in spectroscopy.

Chimura et al. proposed an AM and NLFM combination for spectral losses compensation in [36]. Additionally, AM modulation provides spectral smoothness, while NLFM provides efficiency in excitation generator use. The same approach was used to compensate the Fig. 5.39 signal, by producing additional AM compensation using equation (5.12). Resulting in an AM-NLFM sensitivity-compensated signal that is presented in Fig. 5.41.

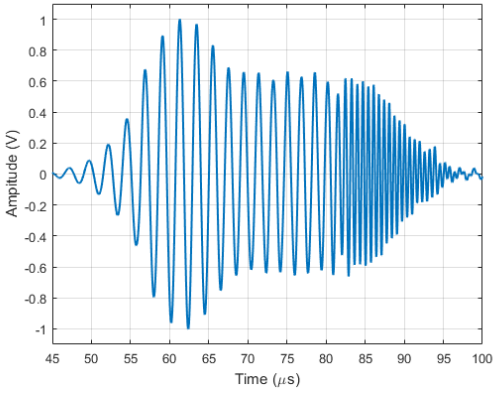

Fig. 5.41. Transmitted AM-NLFM signal with losses compensation

It can be noted that the signal duration has increased, but excitation amplifier dynamic range is exploited more efficiently than in Fig. 5.37. Transmitted and received signal spectrums are presented in Fig. 5.42.

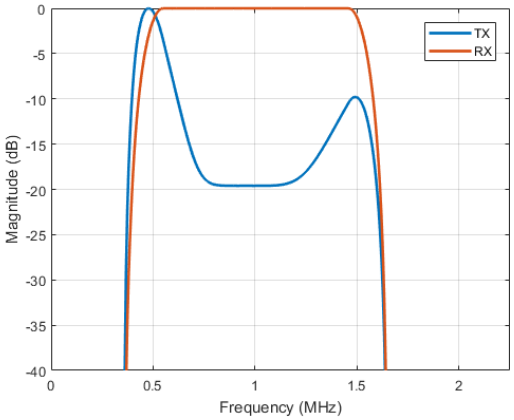

Fig. 5.42. Frequency domain representation of transmitted and received signals when Spectral losses compensation was done using AM-NLFM signal

As a result of the smooth envelope windowing and accurate amplitude, the compensation received signal spectrum is flat and does not contain significant ripples. However, the AM-NLFM signal corresponds to arbitrary waveform and therefore posed the aforementioned drawbacks. Furthermore, derivation of NLFM signals is an approximate procedure.

Rectangular pulses are relatively easy to generate, offer small equipment size and low cost. Linear and nonlinear frequency modulation (chirp) signals can also be generated using rectangular pulses, but this will create additional spectral ripples.

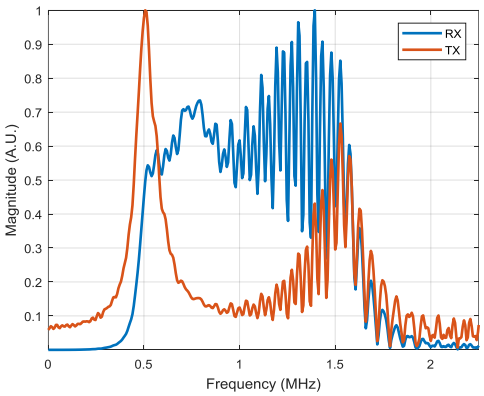

Fig. 5.43. Frequency domain representation of transmitted and received signals when spectral losses compensation was done using rectangular wave NLFM signal

The spread spectrum signals can be generated using arbitrary position and width pulses sequences. Unfortunately, direct derivation of APWP sequences is a lengthy process. The novelty of the approach presented here is that AM-NLFM spread spectrum signal is converted into a bipolar APWP sequence and this sequence is used for further optimization to improve the spectral flatness of the received signal.

Harmonic version of NLFM, AM, and AM-NLFM signals requires an arbitrary waveform generator and linear power amplifier. If would be preferable to use quasi

chirp signals, when the sinusoid is converted into rectangular pulses (e.g. using sign function). In such a case, the output dynamic range is used even more efficient than in the case of LFM or NLFM signals. The first harmonic of the rectangular waveform is approximately 1.3 times higher than the same amplitude of the sinusoidal wave.

Arbitrary position and width pulse trains are a novel class of spread spectrum signals. Spectral spread is produced using trains of rectangular pulses that are placed at specific positions in time in order to provide a spectrum spread of the signal. It was shown that spectral shape or correlation sidelobes can be programmed by an iterative optimization procedure [79,80]. Yet, construction of APWP signals requires a lengthy iterative process when no initial guess is available. NLFM SS signals are easier to derive, but their spectral flatness is unsatisfactory.

This research proposed a novel approach, when AM-NLFM SS signal is converted into rectangular APWP sequence and this sequence is used for further optimization to improve the spectral flatness. Essential drawback of rectangular wave are spectral ripples. While NLFM ripples are within 4 dB range (Fig. 5.40), NLFM rectangular version has 20 dB ripples (Fig. 5.43). Rectangular envelope is implementing the ripples because of convolution with the *sinc* function in the spectral domain. Another *sinc* function appears due to the rectangular nature of each APWP pulse. Smooth envelope of the AM-compensated and AM-NLFM signals is the reason for good spectral flatness performance of the AM-compensated signal. Instead of optimizing the pulse durations and positions of the APWP sequence as in chapter 4.1, on this occasion only additional zeros were inserted (Fig. 5.44) in optimization.

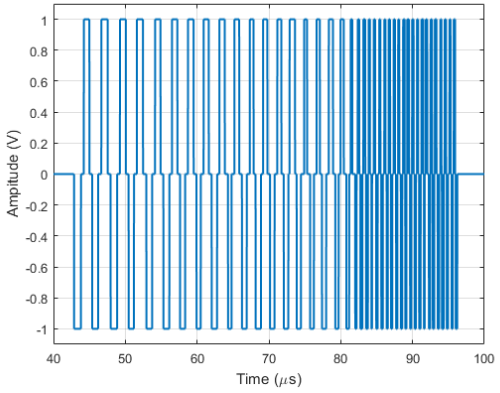

Fig. 5.44. Optimized APWP signal used in transmission for transducer spectral losses compensation

It was expected that reducing the duration of APWP pulses should be equivalent to windowing using the smooth envelope function. A genetic algorithm was used to select the optimal APWP pulses duration reduction. The start and end of every pulses in the APWP sequence were optimized separately. Standard deviation of the received signal $S_{RX}(f)$ magnitude spectrum within 0.5 MHz (f_{min}) to 1.5 MHz (f_{max}) range was used as convergence criteria:

$$\sigma = \sqrt{\frac{\int_{f_{\min}}^{f_{\max}} \left| S_{RX}(f) - \overline{S}_{RX} \right|^2 df}{(f_{\max} - f_{\min})}} . \tag{5.17}$$

Refer Fig. 5.44 for optimized APWP signal. Resulting spectrum response of the received signal, when signal in Fig. 5.44 was used for excitation is presented in Fig. 5.45.

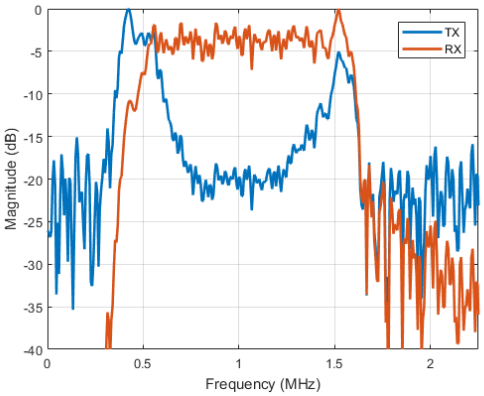

Fig. 5.45. Spectral losses compensation using APWP signal.

Spectral losses compensation performance can compared at Fig. 5.46 left; where spectrums of all received signals are presented. It should be noted, that peak amplitude for all transmitted signals used in this experiment was the same. Comparison of the transmitted signal spectrums can be found in Fig. 5.46 right.

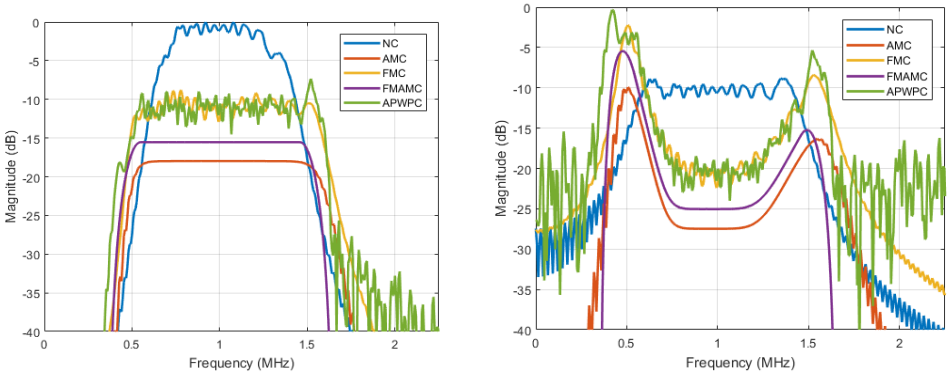

Fig. 5.46. Comparison of spectral losses compensation (left) and corresponding transmission signals (right)

It can be seen that the none compensated signal has the highest energy in the passband, but its energy quickly diminishes out of passband. The none compensated signal also has spectral ripples, which are the reason of the rectangular envelope of

the sinusoidal chirp. AM and AM-FM compensated signals have a very smooth spectrum, but their energy is the lowest in the passband, because full swing of the power amplifier was used inefficiently. Energy is lower despite the longer duration of these signals. NLFM and APWP signals energy is 8 dB higher than for AM and AM-FM compensated signals. Essentially, the performance of the NLFM and APWP signals is the same. All signals apart from APWP are analog, therefore require a linear amplifier for excitation.

5.4.2. Spectroscopy measurements

The same idea as above was used in a real spectroscopy experiment presented below. Spectroscopy measurements were done through transmission for a thin membrane (187 μm thickness). Photo of the experiment setup is presented in Fig. 5.47.

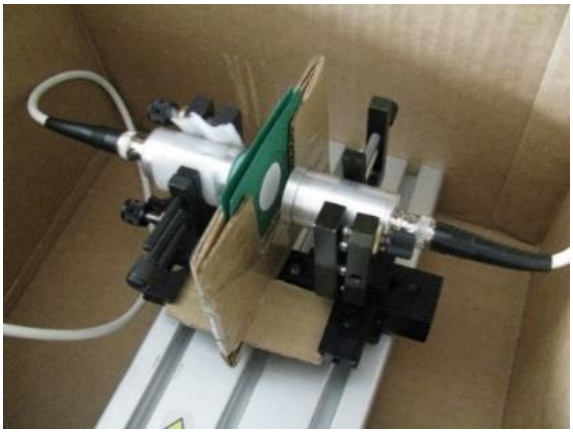

Fig. 5.47. Spectroscopy experiment setup

A pair of wideband 0.65 MHz ultrasonic transducers from CSIC were placed against each other at 30 mm distance. Ultrasound excitation has been done using a bipolar pulser SE TX01-02. Received signal, after being conditioned by the programmable gain block was digitized using 100 Ms/s 10 bit acquisition system [14]. Excitation voltage was 50 V, reception gain 34.59 dB. Four types of signals were used in the experiment: short pulses (step and pulse), toneburst (0.65 MHz 1 period, 0.35 MHz 5 periods, 0.9 MHz 5 periods, 0.5 MHz 1 period, 0.5 MHz 5 periods), chirp (covering (0.3-1)MHz band with 3 μs, 10 μs and 15 μs durations) and APWP optimized for bandwidth flatness of the received signal. Refer Fig. 5.48 and Fig. 5.49 for representative spectrums reference signals (obtained without sample inserted, blue curves), measurement signals (obtained with sample inserted, red curves) and resulting test material spectroscopic response (obtained using equation (5.9), orange curves).

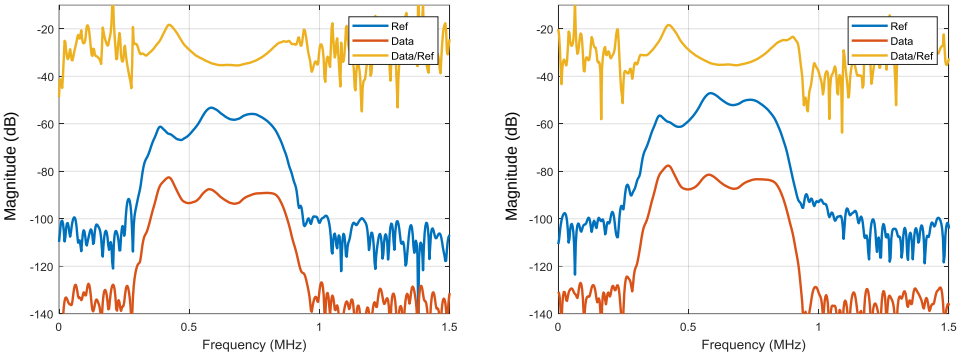

Fig. 5.48. Pulse (left) and toneburst 065 (right) signals and transmission obtained

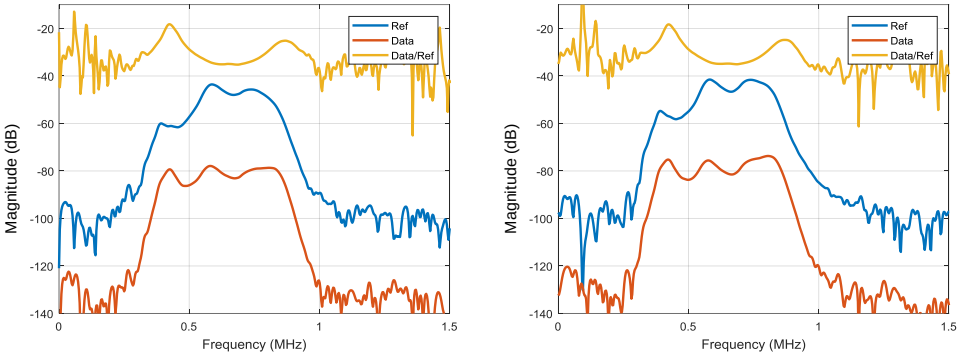

Fig. 5.49. Chirp and APWP signals and transmission obtained

Comparison of magnitude (Fig. 5.50 left) and phase (Fig. 5.50 right) response supplied to spectroscopy analysis indicates that the pulse signals are not able to cover the second resonant peak.

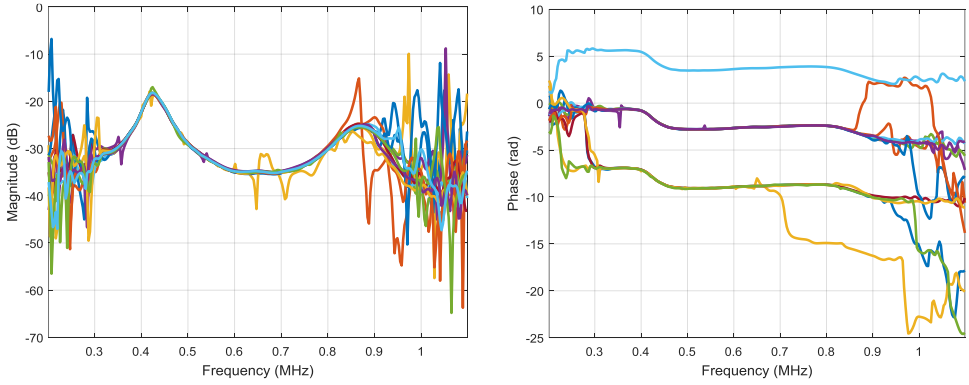

Fig. 5.50. Comparison of obtained material transmission response for magnitude (left) and phase (right)

Toneburst signals have large energy but are not able to cover both resonant peaks. A special, dual toneburst signal was included with 0.35 MHz and 0.9 MHz fill-in frequencies in order to inspect such signal performance. These frequencies were selected to cover the spectral peaks of the tested material. It can be seen that chirp signals have excellent bandwidth coverage and offer good SNR in transmission measurement, especially at high frequencies.

Membrane parameters measurements were done using the resonant spectroscopy technique presented in [64]. The resonance spectroscopy technique allows research to estimate the ultrasound velocity, material thickness and density. Frequency range (0.4-0.9) MHz was used in processing. Measurements were carried out 50 times for every signal. The obtained velocity, thickness and density results were processed to extract the random errors. Variabilities for all signals used are given in Table 5.7 for comparison.

Table 5.7. Material parameters estimation errors

Nr.	**Signal**	**Velocity σ(m/s)**	**Thickness σ(µm)**	**Density σ(g/cm^3)**
1	Pulse 0.65 MHz	0.0029	0.3944	0.3426
2	Toneburst 0.65 MHz 1 period	0.0194	2.5691	2.2236
3	Toneburst 0.35 MHz 5 period	0.0266	8.6794	7.1459
4	Toneburst 0.9 MHz 5 period	0.0113	1.4983	0.9799
5	Chirp (0.3-1) MHz 3 us	0.0009	0.3772	0.3265
6	Chirp (0.3-1) MHz 10 us	0.0017	0.3782	0.3279
7	Chirp (0.3-1) MHz 15 us	0.0013	0.3841	0.3324
8	Step	0.0094	0.8760	0.7582
9	Toneburst 0.5 MHz 1 period	0.5418	3.4897	5.0158
10	Toneburst 0.5 MHz 5 period	0.0092	0.4480	0.3916
11	Chirp (0.2-1) MHz 15 us	0.0014	0.3232	0.2797
12	Toneburst (0.35&0.9) MHz 5 period	0.0021	0.8106	0.7017
13	APWP	0.0005	0.3381	0.2926

Table 5.7 results are presented in graphical form in Fig. 5.51. Material parameters estimation random errors below. It can be seen that the APWP signal (No 13) provides the lowest random errors for all parameters estimation, because its wide band fully covers several peaks and dips (essential in attenuation measurements). The specially constructed dual toneburst signal, whose frequencies were concentrated at resonances frequencies, also has good performance. The disadvantage of such a dual toneburst is that fill-in frequencies have to be selected again for every new test object. This selection has to be done manually, using a calibrating measurement. Meanwhile, the APWP signal has to be optimized only once without the material inserted and then can be used indefinitely for all materials.

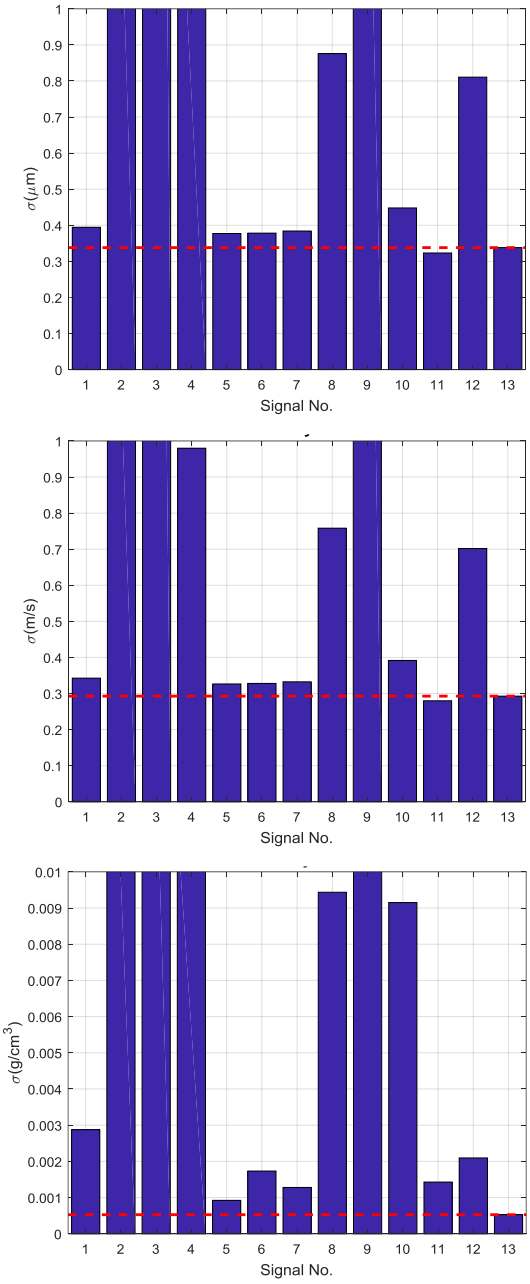

Fig. 5.51. Material parameters estimation random errors: thickness (top), velocity (middle) and density (bottom)

It can be concluded that the APWP signal provides the lowest random errors for all parameters estimation: 0.29 g/cm^3 density error versus (0.4-7) g/cm^3 for other signals, 0.3 μm thickness error versus (0.4-8.6) μm for other signals, 0.5 mm/s material velocity error versus (1-500) mm/s for other signals.

5.5. Conclusions of the 5nd chapter

The APWP signal use in ultrasonic applications was studied. It was demonstrated that signal spectrum broadening can be achieved with APWP even for a narrowband transducer, by increasing the excitation energy in stopband. APWP provided both lower sidelobe level SLL and SNR, so the relative noise margin was improved. An increase of 40 % in the relative noise margin, compared to the same length toneburst signals was achieved.

It was demonstrated that there is a flow meter bias errors reduction (differential ToF errors) with APWP. APWP concentrates its spectrum at roll-off edges of passband, therefore the received signal spectrum is flat. APWP signal mean flow rate deviation was 0.062 l/h and total volume error was 0.935 l. Toneburst – from 5 l to 62 l, pulse signals from 39 l to 62 l. It was concluded that the application of chirp and APWP signals has similar performance and allowed for 10 to 100 times reduction of total volume error.

It was demonstrated that detectability in layered laminates NDT for chirp and PSK (Barker 13) was the best, while APWP had lower performance. APWP was the only signal that was able to efficiently detect the delamination at the upper part of the image. Though, these large indications reduce the image dynamic range.

A new technique for APWP signal derivation and spectral loses compensation has been proposed. The technique has been compared with AM, NLFM and AM-FM compensated signals. These signals require arbitrary waveform generation, while electronics for APWP signal generation is much less complex and efficiency is higher. It was found that the APWP signals energy is 8 dB higher than for AM and AM-FM compensated signals. Essentially, the spectral flatness performance of the NLFM and APWP signals were the same. It was noted that the APWP signal has a slightly wider bandwidth. For spectroscopy it is essential to cover the low frequencies end in order not to miss the first spectral peaks or zeros.

Membrane parameters measurements was done using resonant spectroscopy and APWP signals. It was concluded that the APWP signal provides the lowest random errors for all parameters estimation: 0.29 g/cm^3 versus (0.4-7) g/cm^3 for other signals; 0.3 μm thickness error versus (0.4-8.6) μm for other signals and 0.5 mm/s material velocity error versus (1-500) mm/s for other signals. The APWP signal has to be optimized only once (without material inserted) and can then be used indefinitely for all measurements.

GENERAL CONCLUSIONS

1. Limitations of conventional excitation signals have been rectified through performance analysis. It has been demonstrated that simple (pulse or toneburst) signals do not provide energy and bandwidth simultaneously. Energy increase of the pulse by larger excitation amplitude reduces the maximum operation frequency, due to a slew rate limitation. The spectral shape of these signals is not flat, spectral zeros are present and a large part of the spectral content is outside of the transducer passband. Spread spectrum signals offer independent control over energy and bandwidth: energy can be increased by longer durations without bandwidth reduction. Yet, conventional spread spectrum signals have shortcomings. Though they can be compressed through correlation processing, this produces correlation sidelobes. LFM (chirp) signals have good spectral coverage, they possess large sidelobes. While PSK signals have controllable sidelobes (by code length), their spectrum has dips, spectral shape and bandwidth are fixed. Despite NLFM, AM and arbitrary waveform signals having spectral control, they require complex excitation electronics.
2. Applications analysis allowed to select the properties that have been retained in new signals: efficiency of the excitation, low complexity of the electronics required for signal generation, compressibility, high energy, correlation properties and spectral control. Three application areas were selected: resonant spectroscopy, measurements and imaging cases with a high dynamic range of reflections.
3. A new class of spread spectrum signals has been proposed, APWP (Arbitrary Position and Width Pulses) sequences. They are based purely on binary, unmodulated unipolar or bipolar pulses with optional zeros inserted. Signals are optimized according to the selected performance parameter. Correlation lobes, energy, spectral shape and bandwidth of the received signal were proposed as convergence criteria. The optimization accounts for the system transmission response. It was proposed to replace the online measurements by a numerical model of the system transmission in order to speed up the optimization. A high degree of freedom and absence of mathematical methods for such sequences derivation requires full permutation of all possible pulse combinations, but the number of possible combinations is extremely large. Three algorithms have been suggested to ease the generation of candidate sequences: Monte Carlo, genetic and derivation from NLFM.
4. Performance of the APWP signals has been investigated using rectified metrics. It has been demonstrated that APWP signals are able to concentrate the signal's spectrum into an arbitrary bandwidth or shape, or can add energy out of band (8 dB higher spectral components have been obtained in stop band). It was shown that APWP signals have a programmable sidelobes' level. Sidelobes' level lower than chirp and PSK (Barker) signals and similar to pulse can be achieved. APWP signals provide better iterative deconvolution performance compared to pulse signals. It was demonstrated that APWP signals, despite significant overlap, have improved the iterative deconvolution performance (error was reduced from 10 ns to 0.5 ns).

5. It has been demonstrated that APWP signals offer improved performance in imaging and measurement applications. The relative noise margin was improved by 40 % due to the lower sidelobe level and higher SNR; even for narrowband transducers in anemometry. Significant flow meter bias errors (differential ToF) reduction is achieved with APWP (0.935 l over 15 h), compared to conventional pulse (39 l), toneburst (5 l) and LFM signals (5 l). Superior APWP performance over conventional spread spectrum AM, LFM, NLFM, AM-NLFM signals has been demonstrated in spectral losses compensation in resonant spectroscopy. The APWP signal provides the lowest random errors in material thickness, velocity and density estimation (e.g. 0.29 g/cm^3 versus (0.4-7) g/cm^3 for other signals).

REFERENCES

1. WELLS, P.N.T. Ultrasonic imaging of the human body. *Reports on Progress in Physics*, 1999, vol. 62, no. 5, pp. 671–722. ISSN 0031-9155
2. HARRIS, R.A, FOLLETT, D.H., HALLIWELL M. and WELLS P.N.T. Ultimate limits in ultrasonic imaging resolution. *Ultrasound in Medicine & Biology*, 1991, vol. 17, no. 6, pp. 547–558. ISSN 0301-5629
3. CHEN, C.h. *Ultrasonic and Advanced Methods for Nondestructive Testing and Material Characterization*. Singapore: World Scientific Publishing Co. 2007. ISBN 978-981-270-409-2
4. KALASHNIKOV, A.N., IVCHENKO, V., CHALLIS, R.E., and HOLMES, A.K. Compensation for temperature variation in ultrasonic chemical process monitoring. In *Ultrasonics Symposium, 2005 IEEE*. 2005, vol. 2, pp. 1151-1154. ISSN 1051-0117
5. DIXON, S., EDWARDS, C., and PALMER, S.B. High accuracy non-contact ultrasonic thickness gauging of aluminium sheet using electromagnetic acoustic transducers. *Ultrasonics*. 2001 vol. 39, no. 6, pp. 445-453. ISSN 0041-624X.
6. CHAZIACHMETOVAS, A. et al. Evaluation of material nonlinearities using rectangular pulse trains for excitation. In *Physics procedia: proceedings of the 2015 ICU international congress on ultrasonics*, Metz, France. 2015, vol. 70, pp. 582-585. ISSN 1875-3892
7. ZHENG, D., FU, X. and YANG, Z. Research and realisation of reciprocal electronic circuits for gas ultrasonic flow meter. *IET Science, Measurement & Technology*. 2017, vol. 11, issue 5, pp. 666-672. ISSN 1751-8822
8. SVILAINIS, L., KABIŠIUS, P., ALEKSANDROVAS A. and CHAZIACHMETOVAS, A. Excitation signal's influence on ultrasonic transit time flow meter's performance. In *IOP Conference Series: Materials Science and Engineering*, 2012, vol. 42, pp. 1-4. ISSN 1742-6596
9. MCCLEMENTS, J.A. and GUNASEKARAN, S. Ultrasonic characterization of foods and drinks: Principles, methods, and applications. *Critical Reviews in Food Science & Nutrition, 1997*, vol. 37(1), pp. 1-46. ISSN 1040-8398
10. ALEKSANDROVAS, A. et al. Ultrasound-based density estimation of composites using water-air interface. *Elektronika ir elektrotechnika*. Kaunas: KTU. 2016, vol. 22, iss. 6, pp. 28-32. ISSN 1392-1215
11. LIONETTO, F., TARZIA, A. and MAFFEZZOLI, A. Air-coupled ultrasound: a novel technique for monitoring the curing of thermosetting matrices. *IEEE transactions on ultrasonics, ferroelectrics, and frequency control*, 2007, vol. 54, no. 7, pp. 1437-1444. ISSN 0885-3010
12. APARICIO, S. et al. Non-destructive monitoring of curing process in precast concrete. In *IOP Conference Series: Materials Science and Engineering*, 2012, vol. 42, pp.1-4. ISSN 1757-8981
13. SVILAINIS, L., DUMBRAVA, V. and CHAZIACHMETOVAS, A. Versatile signal acquisition system for ultrasound equipment frequency domain parameters estimation. *Sensors & Transducers*, 2013, vol. 24, pp. 7-17. ISSN 1726- 5479
14. SVILAINIS, L. et al. Acquisition system for the arbitrary pulse width and position signals application in ultrasound. *Sensor letters*, 2014, vol. 12, iss. 9, pp. 1399-1407. ISSN 1546-198X

15. JACOVITTI, G. and SCARANO, G. Discrete Time Techniques for Time Delay Estimation. *IEEE Transactions on Signal Processing*, 1993, vol. 41, pp. 525-533. ISSN 1053-587X
16. SVILAINIS, L. et al. Comparison of spread spectrum and pulse signal excitation for split spectrum techniques composite imaging. In *International Symposium on Ultrasound in the Control of Industrial Processes (UCIP 2012)*, pp. 1-4. ISSN 1757-8981
17. SVILAINIS, L. et al. Signal stripping technique for ultrasonic imaging. In *IC-MINDT-2013 : Materials integrated non destructive testing : 5th international conference on NDT of HSNT-IC MINDT 2013*.
18. POLLAKOWSKI, M. and ERMERT, H. Chirp signal matching and signal power optimization in pulse-echo mode ultrasonic nondestructive testing. *IEEE Transactions on Ultrasonics, Ferroelectrics, and Frequency Control*. 1994, vol. 41, no.5, pp. 655-659. ISSN 0885-3010.
19. SVILAINIS, L., DUMBRAVA, V., KITOV, S. and CHAZIACHMETOVAS A. The influence of digital domain on time of flight estimation performance. In *Conference: International Congress on Ultrasonics, At Gdansk, Volume: 1433*, pp. 479-482. DOI: 10.1063/1.3703231
20. SVILAINIS, L., CHAZIACHMETOVAS, A, and DUMBRAVA, V. Half bridge topology 500V pulser for ultrasonic transducer excitation. *Ultrasonics*, 2015, vol. 59, pp. 79-85. ISSN 0041-624X
21. LICUN, Q. and WANG, R. L. Performance improvement of ultrasonic Doppler flowmeter using spread spectrum technique. In *IEEE International Conference on Information Acquisition*, 2006, pp. 122-126. ISBN 1-4244-0528-9
22. VIROLAINEN, T., ESKELINEN, J., and HAEGGSTROM, E. Frequency domain low timebandwidth product chirp synthesis for pulse compression side lobe reduction. In *Ultrasonics Symposium (IUS), 2009 IEEE International*, 2009, pp. 1526-1528. ISSN 1051-0117
23. ZAPF, M., DEROUICHE, B.F. and RUITER, N.V. Evaluation of chirp and binary code based excitation pulses for 3D USCT. In *Ultrasonics Symposium (IUS), 2009 IEEE International*, 2009, pp. 1996-1999. ISSN 1051-0117
24. HUANG, S.W. and LI, P.C. Arbitrary waveform coded excitation using bipolar square wave pulsers in medical ultrasound. *IEEE transactions on ultrasonics, ferroelectrics, and frequency control*, 2006, vol. 53, no. 1, pp. 106-116. ISSN 0885-3010
25. SVILAINIS, L. and ALEKSANDROVAS, A. Application of arbitrary pulse width and position trains for the correlation sidelobes reduction for narrowband transducers. *Ultrasonics*. 2013, vol. 53, iss. 7, pp. 1344-1348. ISSN 0041-624X.
26. YAMASAKI, T., TAMAI, S., and HIRAO, M. Optimum excitation signal for long-range inspection of steel wires by longitudinal waves. *NDT & E International*, 2001, vol. 34, iss. 3, pp. 207– 212. ISSN 0963-8695
27. FOLKESTAD, T. and MYLVAGANAM, K.S. Chirp excitation of ultrasonic probes and algorithm for filtering transit times in high-rangeability gas flow metering. IEEE Transactions on Ultrasonics, Ferroelectrics, and Frequency Control. 1993, vol. 40, iss. 3, pp. 193–215. ISSN 0885-3010
28. VIROLAINEN, T., ESKELINEN, J. and HAEGGSTROM, E. Frequency domain low time-bandwidth product chirp synthesis for pulse compression side lobe reduction. In

Ultrasonics Symposium (IUS), 2009 IEEE International. 2009, pp. 1526–1528. SSN 1051-0117

29. BENKHELIFA, M.A., GINDRE, M., HUEROU, J.Y. Le and URBACH, W. Echography using correlation techniques: choice of coding signal. *IEEE Transactions on Ultrasonics, Ferroelectrics, and Frequency Control.* 1994, vol. 41, iss. 5, pp. 579–587. ISSN 0885-3010
30. RODRÍGUEZ, A. et al. Split Spectrum processing applications for new composite materials imaging. In *Ultrasonics Symposium (IUS), 2012 IEEE International*. 2012, pp. 1473-1476. ISSN 1051-0117
31. MISARIDIS, T. and JENSEN, J.A. Use of modulated excitation signals in medical ultrasound. Part II: design and performance for medical imaging applications, *IEEE Transactions on Ultrasonics, Ferroelectrics, and Frequency Control.* 2005, vol. 52, no. 2, pp. 192–207. ISSN 0885-3010
32. HUTCHINS, D., et al. Coded waveforms for optimised air-coupled ultrasonic non-destructive evaluation. *Ultrasonics*, 2014, vol. iss. 7, pp. 1745–1759. ISSN 0041-624X
33. ALVAREZ, F. J. et al. Real-time implementation of an efficient correlator for complementary sets of four sequences applied to ultrasonic pulse compression systems. *Microprocessors and Microsystems*. 2006, vol. 30, iss. 1, pp. 43–51. ISSN 0141-9331
34. SVILAINIS, L., ALEKSANDROVAS, A., LUKOŠEVIČIŪTĖ, K. and EIDUKYNAS, V. Investigation of the time of flight estimation errors induced by neighboring signals. In *Intelligent Data Acquisition and Advanced Computing Systems (IDAACS), 2013 IEEE 7th International Conference on.* 2013, vol. 1, pp. 413-418. ISBN 9781479914265
35. MISARIDIS Thanassis. *Ultrasound Imaging Using Coded Signals*. Ph.D. thesis. Technical University of Denmark, Department of Electrical Engineering, 2001, 228 p.
36. CHIMURA, D., TOH, R. and MOTOOKA S. Ultrasonic Direction Measurement Method Using Sensitivity Compensated Transmitting Signal and Pulse Compression. *Physics Procedia*, 2015, vol.70, pp. 476-479. ISSN 1875-3892
37. CHIMURA, D., TOH, R. and MOTOOKA S. Spectrum Compensation for Time Reversal Method on Ultrasonic Target Detection Using Pulse Compression. *IEEE Transactions on Ultrasonics, Ferroelectrics, and Frequency Control*. 2017, vol. 64, iss. 12, pp. 1874 – 1883. ISSN 0885-3010
38. SVILAINIS, L. et al. Electronics for ultrasonic imaging system. *Electronics and electrical engineering*. 2014, vol. 20, no. 7, pp. 51-56. ISSN 1392-1215
39. SVILAINIS, L., DUMBRAVA, V., CHAZIACHMETOVAS, A., ALEKSANDROVAS, A. Pulser for arbitrary width and position square pulse trains generation. In *Ultrasonics Symposium (IUS), 2012 IEEE International.* 2012, pp. 1746-1749. ISSN 1051-0117
40. SVILAINIS, L. Review of high resolution time of flight estimation techniques for ultrasonic signals. In *Conference: BINDT 2013*, At Telford. ISBN 9780903132567
41. SVILAINIS, L., LUKOSEVICIUTE, K., DUMBRAVA, V. and CHAZIACHMETOVAS, A. Subsample interpolation bias error in time of flight estimation by direct correlation in digital domain. *Measurement*. 2013, vol. 46, iss. 10, pp. 3950-3958. ISSN 0263-2241
42. HE-WEN, W., SHANGFU, Y. and QUN, W. Influence of Random Carrier Phase on True Cramer-Rao Lower Bound for Time Delay Estimation. In *Acoustics, Speech and*

Signal Processing, 2007. ICASSP 2007. IEEE International Conference on. 2007, vol. 3, pp. 1029-1032. ISSN 1520-6149

43. VIOLA, F. and WALKER, W. F .A Comparison of the Performance of Time-Delay Estimators in Medical Ultrasound. *IEEE Transactions on Ultrasonics, Ferroelectrics, and Frequency Control*. 2003, vol. 50, no. 4, pp, 392-401. ISSN 0885-3010
44. MINKOFF John. *Signal Processing Fundamentals and Applications for Communications and Sensing Systems*. Artech House, London, 2002. ISBN 9781580535670
45. PARRILLA, M., ANAYA, J.J. and FRITSCH, C. Digital signal processing techniques for high accuracy ultrasonic range measurements. *IEEE Transactions on Instrumentation and Measurement.* 1991, vol. 40, no. 4, pp. 759-763. ISSN 0018-9456
46. CRAMER Harald. *Mathematical Methods of Statistics*. Princeton Univ. Press, Princeton, NJ, 1946. ISBN 9781400883868
47. RADHAKRISHNA RAO, C. Information and the accuracy attainable in the estimation of statistical parameters. Springer, New York, NY 1992. ISBN 978-0-387-94037-3
48. SVILAINIS, L. and DUMBRAVA, V. Investigation of a preamplifier noise in a pulse-echo mode. *Ultrasound.* 2005, vol. 56, no. 3, pp. 26–29. ISSN 1392-2114
49. YANEZ, Y. et al. Designing amplifiers with very low output noise for high impedance piezoelectric transducers. *NDT & E International.* 2005, vol. 38. iss. 6, pp. 491-496. ISSN 0963-8695
50. BECHOU, L. et al. An improved method for automatic detection and location of defects in electronic components using scanning ultrasonic microscopy. *IEEE Transactions on Instrumentation and Measurement*. 2003, vol. 52, iss. 1, pp. 135 – 142. ISSN 0018-9456
51. ZALA, C. A., BARRODALE, I. and MCRAE K. I. High Resolution Deconvolution of Ultrasonic Traces. In *Signal Processing and Pattern Recognition in Nondestructive Evaluation of Materials.* Vol.44, pp. 101-108. Print ISBN 978-3-642-83424-0
52. SVILAINIS, L. et al. Application of iterative deconvolution technique for ultrasonic imaging. Sensor letters. 2014, vol. 12, iss. 11, p. 1572-1582. ISSN 1546-198X
53. LI, X., LI, X., LIANG, W. and CHEN, L. L0-norm regularized minimum entropy deconvolution. NDT&E International. 2012, vol. 47, pp. 80–87. ISSN 0963-8695
54. RAIŠUTIS, R., KAŽYS, R. and MAŽEIKA, L. Application of the ultrasonic pulse-echo technique for quality control of the multi-layered plastic materials. *NDT & E International*. 2008, vol. 41, iss. 4, pp. 300-311. ISSN 0963-8695
55. SANCHO-KNAPIK, D. et al. Air-Coupled Ultrasonic Resonant Spectroscopy for the Study of the Relationship Between Plant Leaves Elasticity and Their Water Content. *IEEE Transactions on Ultrasonics, Ferroelectrics, and Frequency Control*. 2012. vol. 59, iss. 2, pp. 319 - 325. ISSN 0885-3010
56. SVILAINIS, L., CHAZIACHMETOVAS, A. and DUMBRAVA, V. Efficient high voltage pulser for piezoelectric air coupled transducer. *Ultrasonics,* 2013, vol. 53, iss. 1, pp. 225-231. ISSN 0041-624X
57. JAHANGIR KHAN Kayani. *Development and application of spread-spectrum ultrasonic evaluation technique*. Dissertation. Digital Repository, Iowa State University 1996, p.-227
58. STURM, C. and WIESBECK, W. Waveform Design and Signal Processing Aspects for Fusion of Wireless Communications and Radar Sensing. In *Proceedings of the IEEE.* 2011, vol. 99, iss. 7, pp. 1236-1259. ISSN 0018-9219

59. KAGEYAMA, S., HASEGAWA, H. and HIROSHI, K. Increasing Bandwidth of Ultrasound Radio Frequency Echoes Using Wiener Filter for Improvement of Accuracy in Measurement of Intima-Media Thickness. *Japanese journal of applied physics*, 2013, vol. 52, no. 7s, pp. 07HF04-1-6. ISSN 0021-4922

60. TURO, A. et al. Ultra-low noise front-end electronics for air-coupled ultrasonic non-destructive evaluation. *NDT & E International*, 2003, vol. 36, iss. 2, pp. 93-100. ISSN 0963-8695

61. SALAZAR, J. et al. High-Power High-Resolution Pulser for Air-Coupled Ultrasonic NDE Applications. *IEEE Transactions on Instrumentation and Measurement*. 2003, vol. 52, no. 6, pp. 1792-1798. ISSN 0018-9456

62. LIAUKONIS, D., ALEKSANDROVAS, A. and SVILAINIS, L. Epoxy cure monitoring using ultrasonic spread spectrum binary signals. In *Information, Electronic and Electrical Engineering (AIEEE), 2014 IEEE 2nd Workshop on Advances in*. 2014, pp. 1-4. ISBN 978-1-4799-7122-0

63. SVILAINIS, L., KABIŠIUS, P. and KITOV, S. Ultrasonic transit time flow meter for diesel: initial analysis. *ULTRAGARSAS (ULTRASOUND).* 2010, vol. 65, no. 4, pp. 16-21. ISSN 1392-2114

64. ALVAREZ-ARENAS, T. E. G. Magnitude and phase spectral analysis of through-transmitted ultrasound pulses for the determination of the ultrasound velocity and the thickness of solid plates. *Physics Procedia*. 2010, vol.3, iss. 1, pp. 541–550. ISSN 1875-3892

65. OTT Henry W. *Electromagnetic Compatibility Engineering*. 2011, John Wiley & Sons, pp. 872. ISBN: 978-0-470-18930-6

66. YAO, Z. and YANG, J. Optimization of Self-Matching Chaotic Pulse Position Modulation Excitation Sequences for Multichannel Sonar Ranging System. *Journal of Information & Computational Science*. 2011, vol. 8, no. 16, pp. 4105-4114. ISSN 1548–7741

67. COWELL, DM. and FREEAR, S. Quinary excitation method for pulse compression ultrasound measurements. *Ultrasonics*, 2008, vol. 48, iss. 2, pp. 98-108. ISSN 0041-624X

68. NOWICKI, A. et.al. Influence of the ultrasound transducer bandwidth on selection of the complementary Golay bit code length. *Ultrasonics*, 2007, vol.47, iss. 1-4, pp. 64-73. ISSN 0041-624X

69. FORTUNA, L., FRASCA, M. and RIZZO, A. Chaotic pulse position modulation to improve the efficiency of sonar sensors. *IEEE Transactions on Instrumentation and Measurement*. 2003, vol.52, iss. 6, pp. 1809-1814. ISSN 0018-9456

70. YAO, Z.-J. et al. Non-crosstalk real-time ultrasonic range system with optimized chaotic pulse position-width modulation excitation. In *Ultrasonics Symposium, 2008. IUS 2008. IEEE*. 2008, pp. 729-732. ISSN 1051-0117

71. JÖRG, K. W. and BERG, M. Sophisticated mobile robot sonar sensing with pseudo-random codes. Robotics and Autonomous Systems. 1988, vol.25, iss. 3-4, pp. 241-251. ISSN 0921-8890

72. HERNÁNDEZ, A. et al. Ultrasonic ranging sensor using simultaneous emissions from different transducers. *IEEE Transactions on Ultrasonic Ferroelectrics and Frequency Control* . 2004, vol.52, no. 12, pp. 1660-1670. ISSN 0885-3010

73. XIAODONG, C., ZHOU, H., WEN, S. and YU, D. Increasing average power in medical ultrasonic endoscope imaging system by coded excitation. In *SPIE 7156, 2008 International Conference on Optical Instruments and Technology: Optical Systems and Optoelectronic Instruments.* 2009, vol. 7156. doi: 10.1117/12.807063

74. FERNANDES, D., GOMES, L. and COSTA, A. Wind speed and direction measurement based on time of flight ultrasonic anemometer. In *Industrial Electronics (ISIE), 2017 IEEE 26th International Symposium on.* 2017, pp. 1417-1422. ISSN 2163-5145

75. SVILAINIS, L., DUMBRAVA, V. and CHAZIACHMETOVAS, A. Universal acquisition system for frequency domain parameters measurement. In *Intelligent Data Acquisition and Advanced Computing Systems (IDAACS), 2011 IEEE 6th International Conference on.* 2011, pp. 10-15. ISBN 978-1-4577-1426-9

76. CAMACHO, J. and FRITSCH, C. Protection Circuits for Ultrasound Applications. *IEEE Transactions on Ultrasonics, Ferroelectrics, and Frequency Control*. 2008, vol. 55, no.5, pp. 1160-1164. ISSN 0885-3010

77. FULLER, M. I., BLALOCK, T. N., HOSSACK, J. A. and WALKER, W. F. Novel Transmit Protection Scheme for Ultrasound Systems. *IEEE Transactions on Ultrasonics, Ferroelectrics, and Frequency Control.* 2007, vol. 54, no.1, pp. 79-86. ISSN 0885-3010

78. POLLAKOWSKI, M., ERMERT, H., BERNUS, L. and SCHMEIDL, T. The optimum bandwidth of chirp signals in ultrasonic applications. *Ultrasonics*. 1993, vol. 31, no. 6, pp. 417-420. ISSN 0041-624X

79. HUANG, H. and PARAMO, D. Broadband electrical impedance matching for piezoelectric ultrasound transducers. *IEEE Transactions on Ultrasonics, Ferroelectrics, and Frequency Control*. 2011, vol.58, iss. 12, pp. 2699-2707. ISSN 0885-3010

80. WIENER NORBERT. *The interpolation, extrapolation and smoothing of stationary time series*. The MIT Press 1964. ISBN 0262730057

81. RODRÍGUEZ, A. and VERGARA, L. A new Split-Spectrum algorithm for dispersive materials using variable bandwidth filters. In *Ultrasonics Symposium (IUS), 2009 IEEE International.* 2009 , pp. 710-713. ISSN 1051-0117

82. RAIŠUTIS, R., KAŽYS, R. and MAŽEIKA, L. Ultrasonic thickness measurement of multilayered aluminum foam precursor material. *IEEE Transactions on Instrumentation and Measurement*. 2008, vol. 57, no. 12, pp. 2846–2855. ISSN 0018-9456

83. SVILAINIS, L. et al. Application of arbitrary position and width pulse trains signals in ultrasonic imaging: correlation performance study. *Elektronika ir elektrotechnika*. 2013, vol. 19, no. 3, p. 57-60. ISSN 1392-1215.

84. KINRA, V. K. and ZHU, C. Ultrasonic nondestructive evaluation of thin (sub-wavelength) coatings. *The Journal of the Acoustical Society of America*. 1993, vol. 93, no. 5, pp. 2454. ISSN 0001-4966

85. TOHMYOH, H. and IKARASHI, H. Detection of Micro-Bubbles in Thin Polymer Films by Means of Acoustic Resonant Spectroscopy. *Japanese Journal of Applied Physics*. 2013, vol. 52, no. 2R, pp. 028001-1-2. ISSN 0021-4922

86. MISARIDIS, T. and JENSEN, J. A. Use of Modulated Excitation Signals in Medical Ultrasound. Part II: Design and Performance for Medical Imaging Applications. *IEEE Transactions on Ultrasonics, Ferroelectrics, and Frequency Control*. 2005, vol. 52, no. 2, pp. 192-207. ISSN 0885-3010

87. LIONETTO, F and MAFFEZZOLI, A. Monitoring the Cure State of Thermosetting Resins by Ultrasound. *Materials*. 2013, vol. 6, no. 9, pp. 3783-3804. ISSN 1996-1944

88. SVILAINIS, L., LUKOSEVICIUTE, K. and LIAUKONIS, D. Reiterative deconvolution: New technique for time of flight estimation errors reduction in case of close proximity of two reflections. *Ultrasonics*. 2017, vol. 76, pp. 154–165. ISSN 0041-624X

89. TOH, R. and MOTOOKA, S. Target ranging using ultrasonic sensitivity-compensated signal and pulse compression. *Japanese Journal of Applied Physics*. 2009, vol. 48, no. 7s, pp. 07GB09-1-7. ISSN 0021-4922

90. GARCIA, J. T. and ALVAREZ-ARENAS, T. E. G. Optimization of the Design of Multifrequency Annular Arrays for Very Wide Band Operation. *Elektronika ir Elektrotechnika*. 2016, vol. 22, pp. 89-93. ISSN 1392-1215

91. SVILAINIS, L., RODRÍGUEZ, A., EIDUKYNAS, V. and ALEKSANDROVAS, A. Comparison of Conventional and Spread Spectrum Signals Application in Thin PCB Imaging. In *ECNDT 2014 proceedings: 11th European conference on non-destructive testing.* 2014, pp. 1-9. ISBN 9788021450189

92. SVILAINIS, L., CHAZIACHMETOVAS, A. and DUMBRAVA, V. Half bridge topology 500V pulser for ultrasonic transducer excitation. *Ultrasonics*, 2015, vol. 59, pp. 79-85. ISSN 0041-624X

93. CICEK, I, BOZKURT, A. and KARAMAN, M. Design of a Front-End Integrated Circuit for 3D Acoustic Imaging Using 2D CMUT Arrays. *IEEE Transactions on Ultrasonics, Ferroelectrics, and Frequency Control*. 2005, vol. 52, iss. 12, pp. 2235-2241. ISSN 0885-3010

94. LEE, S. et al. Fabrication and Characterization of Embedded Capacitors in Printed Circuit Boards using B-stage Epoxy/BaTiO3 Composite Embedded Capacitor *Films. In Electronic Components and Technology Conference, 2008. ECTC 2008. 58th*. 2008, pp. 742 – 746. ISSN 0569-5503

95. CAMPOLO, D., SITTI, M. and FEARING, R. S. Efficient charge recovery method for driving piezoelectric actuators with quasi-square waves. *IEEE Transactions on Ultrasonics, Ferroelectrics, and Frequency Control*. 2003, vol.50, iss. 3, pp. 237-244. ISSN 0885-3010

96. ARMANAVIČIUS, G. and KAŽYS, R. Analysis of pseudo noise sequences for multi channel distance measurements. *Ultrasound*. 2000, vol. 37, iss. 4, pp. 16-23. ISSN 1392-2114

97. KAŽYS, R., SVILAINIS, L and MAŽEIKA, L. Application of orthogonal ultrasonic signals and binaural processing for imaging of the environment. *Ultrasonics*. 2000, vol. 38, no. 1–8, pp. 171-175. ISSN 0041-624X

98. NIEDERDRANK, T. Maximum length sequences in non-destructive material testing: application of piezoelectric transducers and effects of time variances, *Ultrasonics.* 1997, vol. 35, iss. 3, pp. 195–203. ISSN 0041-624X

99. Non-destructive testing: Characterization and verification of ultrasonic examination equipment Part 1: Instruments. Standard BS EN 12668-1:2010, British Standards Institution, p.48.

100. SVILAINIS, L., DUMBRAVA, V. and CHAZIACHMETOVAS, A. Procedure for the recovery time estimation of the ultrasonic preamplifier. *NDT 2013 Conference & Database Exhibition*. 2003, vol. 1. Northampton: The British Institute of Non-Destructive Testing, 2013. pp. 1-12. ISBN 9780903132567

LIST OF RESEARCH PUBLICATIONS

Articles indexed in the Web of Science with Impact Factor

1. Svilainis, L.; Rodriguez-Martinez, A.; Chaziachmetovas, A.; **Aleksandrovas, A.** Ultrasound Transmission Spectral Compensation Using Arbitrary Position and Width Pulse Sets. *IEEE Transactions on Instrumentation and Measurement*. ISSN: 0018-9456. DOI: 10.1109/TIM.2018.2809838. 2018, vol. 67. iss. 8, pp. 1778-1785. [IF: 2.794, Q1]
2. **Aleksandrovas A.**; Rodríguez, A.; Svilainis, L.; de la Casa, M.A.; Salazar, A. Ultrasound-based density estimation of composites using water-air interface. *Elektronika ir elektrotechnika*. Kaunas : KTU. ISSN 1392-1215. 2016, vol. 22, iss. 6, pp. 28-32. [IF: 0,859, Q4]
3. Svilainis, L.; Rodríguez, A.; **Aleksandrovas, A.** Ultrasonic system models for pulse trains excitation tuning . *Elektronika ir elektrotechnika*. Kaunas : KTU. ISSN 1392-1215. 2016, vol. 22, iss. 2, pp. 62-65. [IF: 0,859, Q4]
4. Svilainis, L.; Dumbrava, V; Kitov, S.; **Aleksandrovas, A.**; Tervydis, P.; Liaukonis, D. Electronics for ultrasonic imaging system. *Elektronika ir elektrotechnika = Electronics and electrical engineering*. Kaunas: KTU. ISSN 1392-1215. 2014, Vol. 20, no. 7, pp. 51-56. [IF: 0,561, Q4]
5. Svilainis, L.; **Aleksandrovas, A.** Application of arbitrary pulse width and position trains for the correlation sidelobes reduction for narrowband transducers. *Ultrasonics. Amsterdam: Elsevier Science*. ISSN 0041-624X. 2013, vol. 53, iss. 7, pp. 1344-1348. [IF: 1,805, Q2]
6. Svilainis, L.; Lukoševičiūtė,K.; Dumbrava,V.; Chaziachmetovas, A. ;**Aleksandrovas,A.** Application of arbitrary position and width pulse trains signals in ultrasonic imaging: correlation performance study. *Elektronika ir elektrotechnika = Electronics and Electrical Engineering*. Kaunas: KTU. ISSN 1392-1215. 2013, Vol. 19, no. 3, pp. 57-60. [IF: 0,445, Q4]

Articles in other peer reviewed research publications (Articles in periodicals, collections of articles, etc.)

1. Svilainis, L.; Dumbrava, V.; Kitov, S.; **Aleksandrovas, A.**; Chaziachmetovas, A.; Eidukynas, V.; Kybartas, D.; Lukoševičiūtė, K. Acquisition system for the arbitrary pulse width and position signals application in ultrasound. *Sensor letters*. Valencia, CA: American Scientific Publishers. ISSN 1546-198X. 2014, vol. 12, iss. 9, pp. 1399-1407.
2. Svilainis, L.; Dumbrava, V.; **Aleksandrovas, A.**; Chaziachmetovas, A.; Kitov, S. Application of iterative deconvolution technique for ultrasonic imaging. *Sensor letters*. Valencia, Ca: American Scientific Publishers. ISSN 1546-198X. 2014, vol. 12, iss. 11, pp. 1572-1582.
3. Svilainis, L.; **Aleksandrovas, A.**; Lukoševičiūtė, K.; Eidukynas, V. Comparison of conventional and spread spectrum signals time of flight error caused by neighboring reflections // International Journal of Computing / Research Institute of Intelligent Computer Systems. Ternopil : Ternopil National Economic University. ISSN 1727-6209. 2013, Vol. 12, iss. 3, pp. 241-247.
4. Svilainis, LK; Dumbrava, V.; Chaziachmetovas, A.; **Aleksandrovas, A.** Application of spread spectrum signals in ultrasonic imaging. Journal of applied electromagnetism. Athens: ICCS. ISSN 1109-1606. 2013, vol. 15, no. 1, pp. 49-64.

Articles in conference proceedings

1. Svilainis, L.; Rodriguez-Martinez, A.; Chaziachmetovas, A.; **Aleksandrovas, A.** Application of binary excitation spread spectrum signals for spectral compensation. *IDAACS 2017: 9th IEEE International Conference on Intelligent Data Acquisition and Advanced Computing Systems: Technology and Applications (IDAACS)*, 21-23 September 2017, Bucharest, Romania. Piscataway, NJ: IEEE, 2017. ISBN 9781538606964. pp. 1105-1110.
2. Chaziachmetovas, A.; Svilainis, L; Kybartas, D.; **Aleksandrovas, A.**; Liaukonis, D. Evaluation of material nonlinearities using rectangular pulse trains for excitation. *Physics procedia : proceedings of the 2015 ICU international congress on ultrasonics, Metz, France*, May 10-15, 2015. Amsterdam: Elsevier. 2015, vol. 70, pp. 582-585.
3. Svilainis, L.; Dumbrava, V.; Chaziachmetovas, A.; Jurkštas, P.; **Aleksandrovas, A.** Technique for the performance evaluation of the ultrasonic preamplifier input protection circuits. *IDAACS'2015: proceedings of the 8th international conference on intelligent data acquisition and advanced computing systems: technology and applications*, September 24-26, 2015, Warsaw, Poland. Piscataway, NJ : IEEE, 2015. ISBN 9781467383592. pp. 102-107.
4. Liaukonis, D.; **Aleksandrovas, A.**; Svilainis, L. Epoxy cure monitoring using ultrasonic spread spectrum binary signals. *2014 IEEE 2nd Workshop on Advances in Information, Electronic and Electrical Engineering (AIEEE): proceedings of the 2nd workshop*, November 28-29, 2014, Vilnius, Lithuania / Vilnius Gediminas Technical University, Riga Technical University. Piscataway, NJ:IEEE, 2014. ISBN 9781479971220. pp. 1-4.
5. Svilainis, L.; Rodríguez, A.; Dumbrava, V.; Lukoševičiūtė, K.; **Aleksandrovas, A.**; Liaukonis, D. Application of arbitrary position and width pulse train signals in ultrasonic imaging. *ECNDT 2014 proceedings: 11th European conference on non-destructive testing*, October 6-10, 2014, Prague, Czech Republic / Czech Society for NDT and European Federation for NDT. Brno: Brno Technical University of Technology, 2014. ISBN 9788021450189. pp. 1-9.
6. Svilainis, L.; Rodríguez, A.; Eidukynas, V.; **Aleksandrovas, A.** Comparison of conventional and spread spectrum signals application in thin PCB imaging. *ECNDT 2014 proceedings: 11th European conference on non-destructive testing*, October 6-10, 2014, Prague, Czech Republic / Czech Society for NDT and European Federation for NDT. Brno: Brno Technical University of Technology, 2014. ISBN 9788021450189. pp. 1-9.
7. Svilainis, L.; Lukoševičiūtė, K.; **Aleksandrovas, A.** Time of flight estimation of sparse ultrasonic reflections using reiterative deconvolution technique. *ACOMEN 2014: book of abstracts of the 6th international conference on Advanced computational methods in engineering*, 23-28 June 2014. Ghent University June 6, 2014. Ghent: Ghent University, 2014. ISBN 9789082230901. pp. 27-28.
8. Svilainis, L.; **Aleksandrovas, A.**; Lukoševičiūtė, K.; Eidukynas, V. Investigation of the Time of Flight estimation errors induced by neighboring signals. *IDAACS'2013: proceedings of the 7th International Conference on Intelligent Data Acquisition and Advanced Computing Systems: Technology and Applications*, September 12-14, 2013, Berlin, Germany. Vol. 1. Piscataway: IEEE, 2013. ISBN 9781479914265. pp. 413-418.
9. Svilainis, L.; Dumbrava, V.; **Aleksandrovas, A.**; Chaziachmetovas, A.; Kitov, S.; Pagodinas, D. Signal stripping technique for ultrasonic imaging. *IC-MINDT-2013: Materials integrated non destructive testing : 5th international conference on NDT of HSNT*, 20-22 May, 2013 Athens, Greece. Athens: HSNT. 2013, pp. 1-8.

10. Svilainis, L.; Dumbrava, V.; Kitov, S.; **Aleksandrovas, A.**; Chaziachmetovas, A.; Eidukynas, V.; Kybartas, D.; Lukoševičiūtė, K. Ultrasonic systems for arbitrary pulse width and position trains application for imaging. *IC-MINDT-2013: Materials Integrated Non Destructive Testing - 2013: 5th International Conference on NDT of HSNT*, 20-22 May, 2013 Athens - Greece Athens: HSNT. 2013, pp. 1-10.
11. Svilainis, L.; **Aleksandrovas, A.**; Lukoševičiūtė, K. Arbitrary width and position pulse trains application for ultrasonic imaging: initial study. *Proceedings of 7th international conference on communications, electromagnetics and medical applications*, Athens, Greece, 8-10 November, 2012 (CEMA'12) / Faculty of Telecomunications Technical University of Sofia, Bulgaria; National Technical University of Athens, Greece. School of electrical and computer engineering. [S.l : s.n]. ISSN 1314-2100. 2012, pp. 87-90.
12. Svilainis, L.; Dumbrava, V.; Chaziachmetovas, A.; **Aleksandrovas, A.** Pulser for arbitrary width and position square pulse trains generation. *2012 IEEE International Ultrasonics Symposium*, October 7 - 10, 2012, Dresden, Germany: proceedings. Piscataway: IEEE, 2012. ISBN 9781467345620. pp. 1746-1749.

Conference proceedings

1. Rodríguez, A.; de la Cassa Lillo, M. A.; **Aleksandrovas, A.**; Svilainis, L.; Galiana, J. C. Characterization of nanoparticles doped composites using ultrasound. *Ultrasonics 2016: 2nd international conference on ultrasonic-based applications: from analysis to synthesis*, 6-8th June 2016, Caparica, Portugal. [S.l.]: Proteomass, 2016. ISBN 9789899936195. pp. 177.

APPENDIX A

	C-scan	Wires spacing
Gencode1	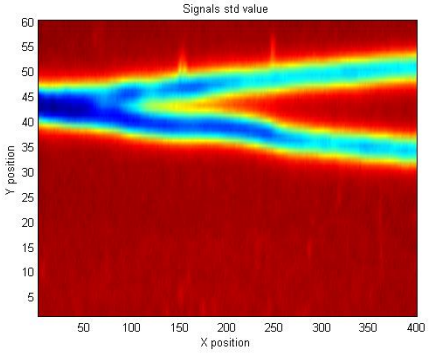	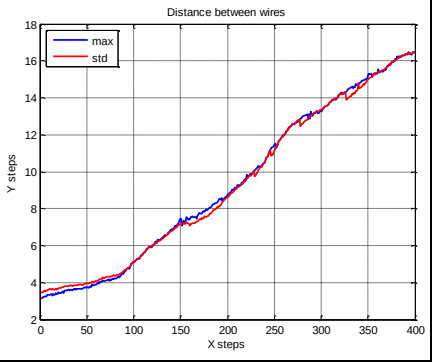
Gencode2	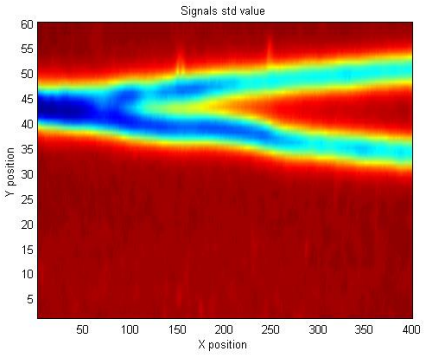	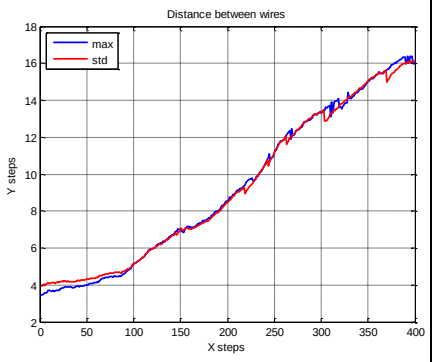
Gencode3	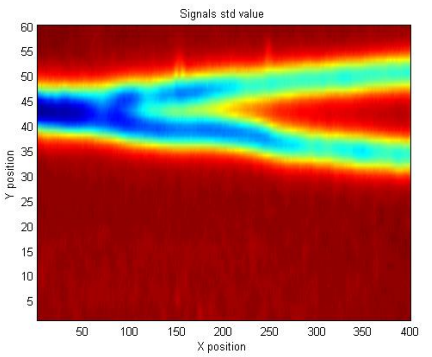	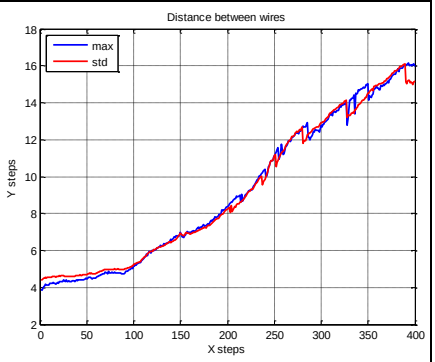
Gencode4	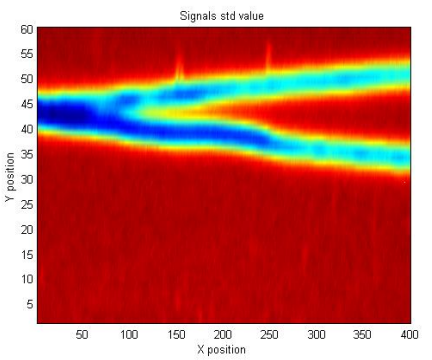	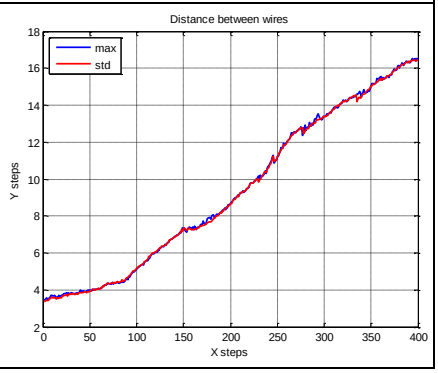

Gencode5	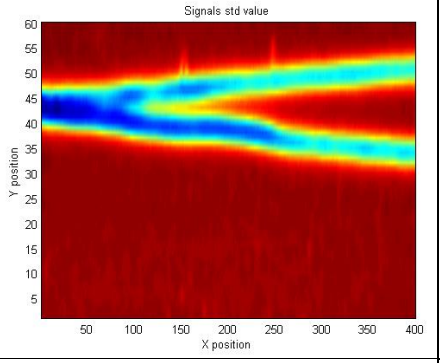	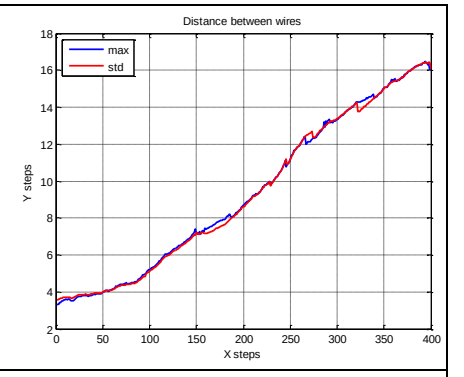
Gencode6	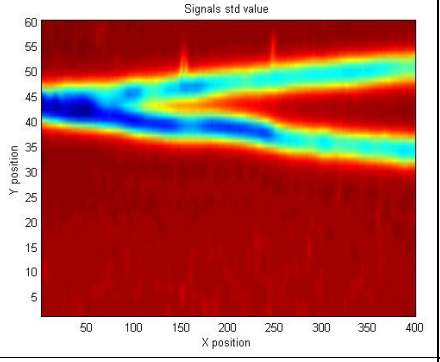	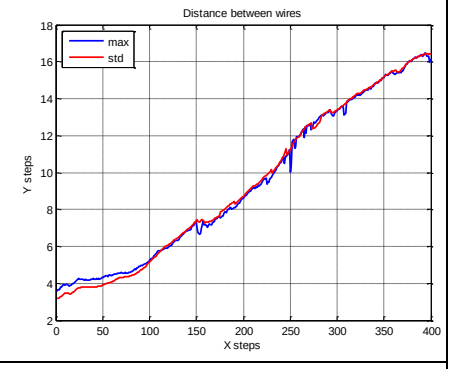
Gencode7	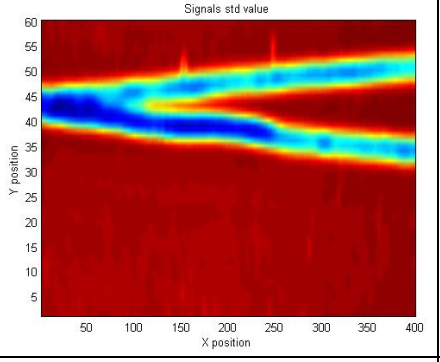	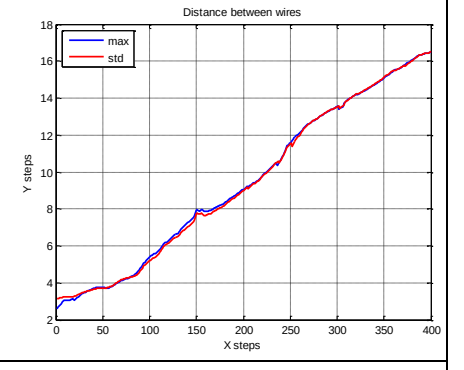
Gencode8	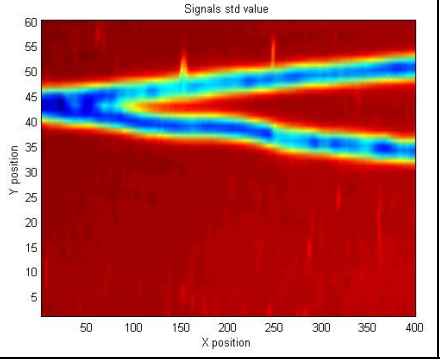	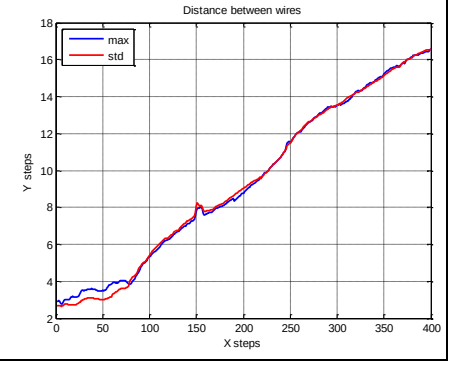

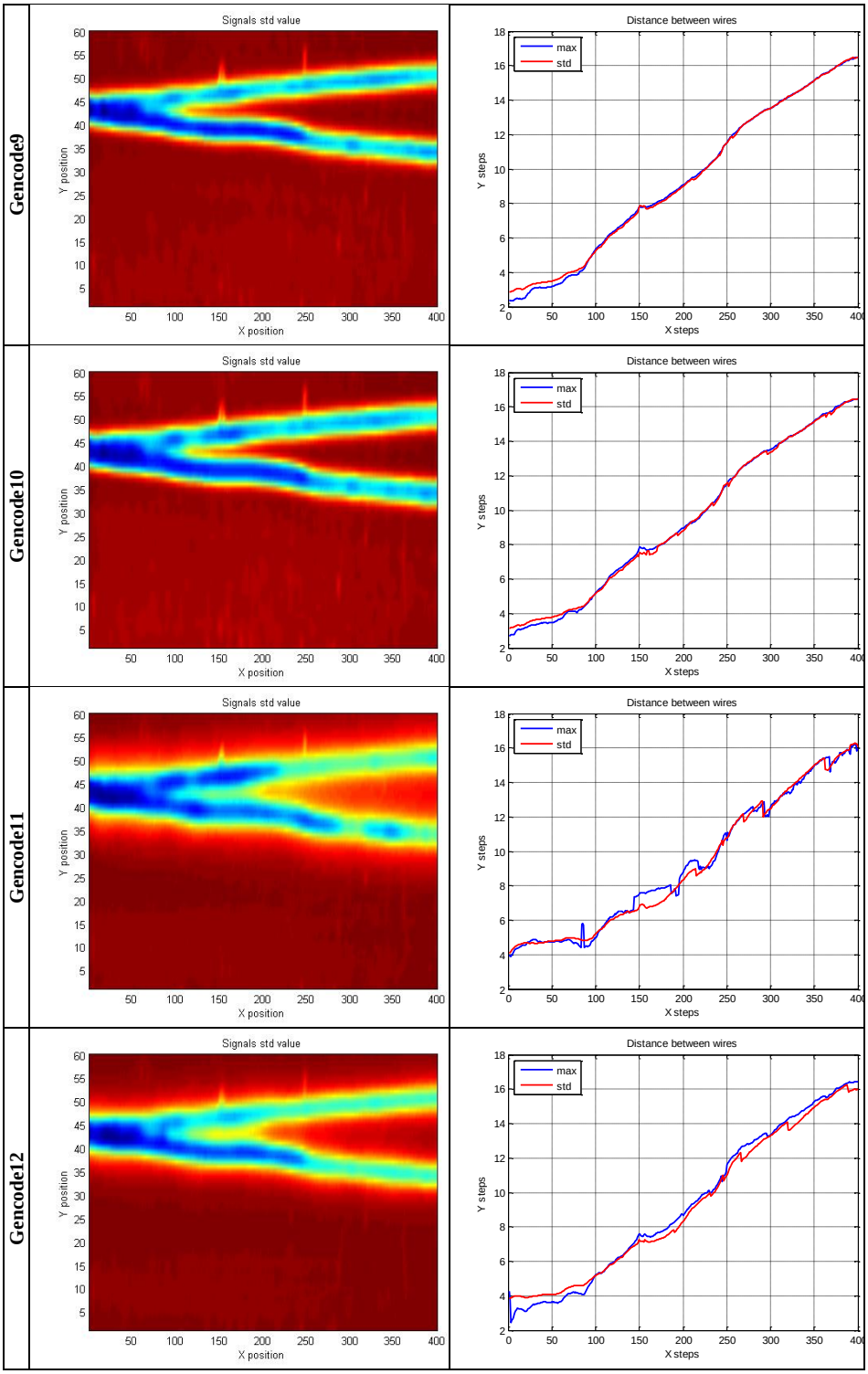

Fig. A.1. C-scan image (left) and wire spacing (right) for all signals used in experiment

SL344. 2018-09-19, 16,5 leidyb. apsk. l. Tiražas 12 egz. Užsakymas 273
Išleido Kauno technologijos universitetas, K. Donelaičio g. 73, 44249 Kaunas
Spausdino leidyklos „Technologija“ spaustuvė, Studentų g. 54, 51424 Kaunas